UNIVERSITY OF GENOVA

PHD PROGRAM IN CHEMICAL AND MATERIALS SCIENCE AND TECHNOLOGY

CD-Enhanced Plasmonic Metasurfaces Based on Achiral and Dimer Gratings for Biosensing Applications

by

MARYAM MIRAHMADI

Thesis submitted for the degree of *Doctor of Philosophy* (38° cycle)

December 2025

Dr. Roman Krahne (IIT)	Supervisor
Prof. Francesco Buatier de Mongeot (DIFI)	Supervisor
Prof. Marco Grotti (DCCI)	Head of the PhD program

Thesis Jury:

Prof. Yang Zhang, *Jinan University, China*	External examiner
Prof. Tobias König, *Leibniz Institute of Polymer Research, Germany*	External examiner

Department of Chemistry and Industrial Chemistry

This thesis is dedicated to my partner-in-crime and my family, whose encouragement and understanding kept me going.

Declaration

I hereby declare that except where specific reference is made to the work of others, the contents of this dissertation are original and have not been submitted in whole or in part for consideration for any other degree or qualification in this, or any other university. This dissertation is my own work and contains nothing which is the outcome of work done in collaboration with others, except as specified in the text and Acknowledgements. This dissertation contains fewer than 65,000 words including appendices, bibliography, footnotes, tables and equations and has fewer than 150 figures.

Maryam Mirahmadi
February 2026

Acknowledgements

I would like to express my deepest gratitude to my supervisors, Dr. Roman Krahne and Dr. Francesco Buatier de Mongeot, for their invaluable guidance, patience, and expertise throughout this research. Their insightful feedback and continuous support were instrumental in shaping and improving this thesis.

I am also deeply grateful to Dr. Tobias König and his research group for their kind support and collaboration, which significantly contributed to part of this thesis.

I would like to sincerely thank all the participants involved in this study for generously sharing their time and experiences. This research would not have been possible without their valuable contributions.

Abstract

Distinguishing the chirality of biomolecules is essential in biophysics and pharmaceutics, yet their intrinsic circular dichroism (CD) signals are typically weak and lie in the ultraviolet (UV) region, demanding costly instrumentation. To address this limitation, this thesis introduces tunable plasmonic and photonic metasurfaces that dramatically enhance CD signals in the visible–NIR range, where optical components are widely accessible. In the first part of this work, tilted gold nanohole arrays are employed to generate extrinsic chirality in fully achiral structures, enabling strong chiroptical responses through geometric symmetry breaking. By integrating these arrays into a Metal-Dielectric-Metal (MDM) cavity, we create a hybrid plasmonic–photonic resonator that produces intense, asymmetric near fields and enhances the chirality enhancement factor, χ, by an additional order of magnitude. Compared to a simple glass-supported biolayer, commonly used in earlier studies, we demonstrate a 50-fold CD enhancement due to the synergistic interplay between the cavity's magnetic-dipole mode and the plasmonic nanohole resonance.

In the second part of the thesis, we investigate an emerging class of intrinsically chiral architectures based on Nanoparticle–on Mirror (NPoM) cavities. Here, cross-stacked nanoparticle dimer gratings are integrated above a thin-film Au/Al_2O_3 cavity to create tunable superchiral hotspots through hybrid coupling of Rayleigh anomalies, guided-mode resonances, and localized plasmons. Unlike the extrinsic-chirality nanoholes, the NPoM structure provides inherent three-dimensional chirality and extremely confined optical fields within accessible nanogaps, offering a powerful platform for boosting molecular CD signals. Together, these two metasurface approaches demonstrate that cavity-assisted chiroptical enhancement can substantially improve enantiomer discrimination and biosensing performance, while offering spectral flexibility through geometric and cavity design—significantly surpassing the capabilities of conventional glass- based plasmonic substrates.

Keywords: Circular dichroism (CD), Chiroptical enhancement, Plasmonic metasurfaces, Metal–Dielectric–Metal (MDM) cavities, Nanoparticle–on Mirror (NPoM) cavities, Extrinsic chirality, Intrinsic chirality, Superchiral hotspots, surface plasmon polariton (SPP), Rayleigh anomalies (RA), Guided-mode resonances (GMR)

Abstract (Italiano)

Distinguere la chiralità delle biomolecole è fondamentale in biofisica e in ambito farmaceutico, ma i loro segnali intrinseci di dicroismo circolare (CD) sono tipicamente deboli e localizzati nella regione dell'ultravioletto (UV), richiedendo strumentazione costosa. Per superare questa limitazione, questa tesi introduce metasuperfici plasmoniche e fotoniche sintonizzabili che amplificano in modo significativo i segnali CD nella regione visibile–NIR, dove i componenti ottici sono facilmente accessibili. Nella prima parte di questo lavoro, matrici di nanofori in oro inclinate vengono utilizzate per generare chiralità estrinseca in strutture completamente achirali, consentendo forti risposte chirottiche attraverso la rottura della simmetria geometrica. Integrando queste matrici in una cavità metal–dielectric–metal (MDM), realizziamo un risonatore ibrido plasmonico–fotonico che produce campi vicini intensi e asimmetrici e aumenta il fattore di amplificazione della chiralità, χ, di un ordine di grandezza aggiuntivo. Rispetto a un semplice biostrato su vetro, comunemente utilizzato in studi precedenti, dimostriamo un incremento di 50 volte del segnale CD grazie all'interazione sinergica tra il modo di dipolo magnetico della cavità e la risonanza plasmonica dei nanofori.

Nella seconda parte della tesi, esploriamo una nuova classe di architetture intrinsecamente chirali basate su cavità Nanoparticle–on Mirror (NPoM). In questo caso, reticoli di dimeri nanoparticellari a geometria incrociata sono integrati sopra una cavità a film sottile Au/Al_2O_3, generando hotspot superchirali sintonizzabili attraverso il coupling ibrido tra anomalie di Rayleigh, risonanze delle guide d'onda e plasmoni localizzati. A differenza dei nanofori a chiralità estrinseca, la struttura NPoM offre una chiralità tridimensionale intrinseca e campi ottici estremamente confinati all'interno di nanogap accessibili, rappresentando una piattaforma potente per l'amplificazione del CD molecolare. Nel complesso, questi due approcci basati su metasuperfici dimostrano che l'amplificazione chirottica assistita da cavità può migliorare significativamente la discriminazione degli enantiomeri e le prestazioni di biosensing, offrendo al contempo flessibilità spettrale tramite il design geometrico e della cavità—superando nettamente le capacità dei tradizionali substrati plasmonici su vetro.

Table of contents

List of figures

Chapter 1

Introduction

1.1 The Fundamentals of Chirality and Enantiomers

Chirality is a fundamental geometric property describing objects or molecular structures that cannot be superimposed on their mirror images [1]. The term derives from the Greek cheir ("hand"), reflecting the classic example of left and right hands as non-superimposable mirror images [2]. In molecular systems, chirality typically arises from an asymmetric stereocenter, giving rise to two mirror-image configurations called enantiomers. Although enantiomers possess identical atomic composition and nearly identical physical properties in achiral environments, they interact differently with other chiral systems. When placed in a chiral environment, such as with another chiral molecule or biological receptor, the spatial orientation of their atoms creates different stereochemical relationships that affect how they fit or bind. For example, enzymes (and most biological receptors) are themselves chiral, so often only one enantiomer will fit into the active site, just like only a right hand fits into a right-handed glove. The other enantiomer may not bind, or may produce a different (often unexpected or toxic) effect [3]. This stereospecific behavior is particularly significant in biological contexts where enzymes, receptors, and metabolic pathways discriminate sharply between opposite enantiomers, making enantiomeric purity central to drug development, biochemical recognition, and structural biology. It has been reported that nearly 56% of the pharmaceuticals marketed and used in therapy are chiral compounds, with a significant portion administered as racemates [4].

Understanding, detecting, and enhancing the optical signatures of chirality thus remains a fundamental scientific challenge [5, 6].

1.2 History of Optical Activity and Circular Dichroism

The scientific understanding of chirality developed alongside early discoveries in optical activity begin with the pioneering experiments of Dominique François Jean Arago. In 1811, Arago observed that sunlight passing through a quartz crystal placed between crossed polarizers exhibited unexpected color patterns and changes in polarization direction, which marks the first recorded observation of optical rotation [7, 8]. Building on this, Jean-Baptiste Biot conducted systematic and quantitative studies from 1812 onward, demonstrating that many organic liquids and crystals rotate the plane of linearly polarized light by an amount dependent on concentration, sample thickness, and wavelength. Biot established the first empirical laws of optical rotation [9], showing that chiral substances possess a measurable and reproducible optical signature.

The next major advancement came from Augustin-Jean Fresnel [10], who showed that optical rotation could be explained by different phase velocities of left- and right-circularly polarized light propagating through a chiral medium, an insight that connected optical activity directly to wave theory. Most critically, Louis Pasteur provided the first experimental evidence of molecular-level chirality in 1848. While studying sodium ammonium tartrate salts, he noted that the crystals formed two distinct but mirror-symmetric shapes. Using tweezers and a microscope, Pasteur manually separated these crystals and found that each type rotated polarized light in opposite directions, demonstrating conclusively that optical activity originates from molecular asymmetry [11].

These foundational works laid the groundwork for the discovery of circular dichroism (CD). In 1895, Aimé Cotton observed that chiral molecules absorb left- and right-circularly polarized (LCP and RCP) light to different extents, establishing what is now known as circular dichroism [12]. Unlike optical rotation, which changes only the polarization angle, CD directly measures the difference in absorption or transmission pathways and therefore carries richer information about electronic and structural transitions.

Over the following century, CD evolved into several distinct chiroptical modalities. Electronic CD (ECD) probes electronic transitions in the UV–visible range, making it indispensable for studying proteins, peptides, and small organic molecules [13]. Vibrational CD (VCD) detects differential absorption of infrared circularly polarized light corresponding to vibrational modes, providing detailed stereochemical information [14]. Raman Optical Activity (ROA) measures differences in Raman scattered light for left and right circularly polarized excitation, enabling highly sensitive structural analysis of biomolecules [15].

Although these techniques differ in spectral range and structural sensitivity, all rely on the fundamental asymmetry in the interaction between chiral matter and polarized light.

1.3 Engineered Nanostructures for Amplified Chiroptical Interactions

Although intrinsic CD spectroscopy is powerful, molecular chiroptical signals are extremely weak, which limits the detection of thin films, low analyte concentrations, and small biological samples. This motivated intense efforts throughout the twentieth century to enhance CD responses, but transformative progress came only with the emergence of nanophotonic and plasmonic structures.

Such nanostructures enable control of electromagnetic fields at deeply subwavelength scales, producing large field enhancements, magnetic dipole responses, and strong local asymmetries that dramatically increase the optical chirality experienced by molecules. Chiroptical enhancement strategies can be broadly grouped into five conceptual categories: (i) single chiral plasmonic nanoparticles, where nanoscale geometric chirality produces strong plasmonic CD; (ii) hybrid complexes formed by achiral nanoparticles interacting with molecularly chiral media, where plasmonic near fields boost the molecular CD; (iii) chiral assemblies of plasmonic nanoparticles, where collective arrangement induces macroscopic chirality; (iv) chiral plasmonic metamaterials and chiral photonic crystals engineered for tailored chiroptical responses; and (v) achiral plasmonic nanostructures that become chiral under symmetry-breaking illumination, producing extrinsic chirality [16].

1.3.1 Progress in Plasmonic and Photonic Circular Dichroism Enhancement for Biolayer Characterization

Nanophotonic and nanoplasmonics approaches have significantly expanded the spectral range in which chiroptical signals can be enhanced, moving beyond the UV, where most biomolecules absorb, into the visible and near-infrared, enabling tunable, highly sensitive detection platforms.

The advent of nanostructuring has revolutionized chiroptical enhancement by leveraging the strong electromagnetic field confinement and enhancement capabilities of metallic

nanostructures. Plasmonic systems can generate "superchiral" fields with enhanced optical chirality parameters, enabling detection sensitivities that are improved by orders of magnitude compared with conventional CD measurements. Various plasmonic architectures have been developed, including chiral nanoparticle assemblies, twisted metallic structures, and hybrid plasmonic-photonic systems [17, 18].

Researchers have explored a range of periodic structures as substrates, including 3D nanohelix arrays [19], twisted cross rods [20], racemic nanoplasmonic arrays [20], chiral assemblies of nanoparticles [21], and achiral plasmonic nanostructures [22]. Other approaches include prism-coupled surface plasmon systems at planar silver–solution interfaces for CD enhancement [23], theoretical modeling of plasmonic CD via Coulombic and electromagnetic interactions in chiral nanoparticle assemblies [24], and experimental and numerical demonstrations of tunable CD using vertically aligned gold nanorod arrays embedded with chiral mercury sulfide (HgS) nanocrystals in a polymer matrix, enabling strong CD enhancement in the visible range [25]. Meniscus-guided self-assembly of achiral CdS, CdSe, and CdTe nanoclusters into helical domains results in giant exciton-coupled CD [26], and strategies leveraging biomolecular functionalization of metal nanoparticles facilitate chirality transfer [27], for example CD of chiral Au nanorod seeds [28]. Numerical demonstrations show that a gain medium surrounding twisted gold nanorod dimers enables tunable, orders-of-magnitude enhancement of circular dichroism [29]. Additionally, attachment of chiral mercury sulfide nanocrystals to amorphous selenium nanospheres yields a fivefold enhancement of visible circular dichroism via Mie resonances [30]. Numerical studies reveal that chiral medium patches placed in plasmonic gap antenna hot spots can achieve up to 750-fold circular dichroism enhancement, surpassing chiral dimer designs [31].

Existing research has largely centered on characterizing the inherent chiroptical behavior of substrates, yet the connection between this behavior and the resulting CD signals in the presence of biolayers is still not well established. In practical biosensing scenarios, it is the collective CD response of the substrate–biolayer assembly that is of primary importance, not the substrate alone. Accordingly, several studies have explored CD enhancement by performing comparative analyses with added biolayers [32]. Leite et al. reported CD enhancement in the far-UV regime using Al gammadion arrays, however, this was only sufficient to lift signals just above the noise level for <10 nm tyrosine films, implying an enhancement of less than 5-fold [33]. In plasmonic nanorod metamaterials, a two-fold enhancement of circular dichroism was observed for embedded chiral mercury sulfide nanocrystals [25]. Mohammadi et al. analytically modeled and experimentally demonstrated

CD enhancement for thin chiral layers using dielectric metasurfaces, reporting enhancement values up to 15, utilizing accessible superchiral near-fields driven by tailored electric and magnetic resonances. Venturi et al. predicted a CD enhancement factor of 20 using surface plasmon polaritons (SPP) in Kretschmann and Otto configurations for dilute chiral drug solutions [23], while García-Guirado et al. demonstrated up to 60-fold enhancement in experiments and 170 in simulations using racemic gammadion arrays for enantiomer-selective sensing in the visible range [34]. Vázquez-Guardado and Chanda reported an achiral plasmonic system that generates pure superchiral near fields with zero far-field CD, enabling background-free molecular chirality detection. They achieved approximately a 4 orders of magnitude enhancement in the asymmetry factor g for vibrational circular dichroism (VCD) sensitivity in low-volume chiral analytes, highlighting the system's potential for ultrasensitive biosensing [35]. Wang et al. demonstrate an extrinsic chiral plasmonic sensor based on achiral gold nanohole arrays at oblique incidence, where adding L- or D-phenylalanine yields opposite g factor shifts and a g factor change of 0.027 near 750 nm compared to ~ 0.001 for the pure chiral medium [36].

These studies highlight that appropriately engineered plasmonic and photonic environments can dramatically amplify molecular CD signals. They also reveal that achieving a balance between strong near-field enhancement, spectral tunability, and compatibility with biological thin films remains an active research challenge, one that directly motivates the metasurface, cavity platforms developed in this thesis. In our study, we emphasize two major chiroptical enhancement pathways: extrinsic chirality, which emerges in achiral nanostructures under symmetry-breaking illumination, and intrinsic chirality, which is supported by plasmonic nanoparticle assemblies.

1.3.2 Extrinsic Chirality in Achiral Plasmonic Structures

A particularly intriguing development involves the generation of extrinsic chirality in inherently achiral nanostructures through specific illumination conditions, placing this mechanism within a distinct category of chiroptical enhancement strategies [37]. This approach circumvents the fabrication challenges associated with intrinsically chiral structures while providing tunable control over chiroptical responses. Achiral plasmonic nanostructures, when illuminated with circularly polarized light at oblique incidence, can exhibit strong CD signals due to symmetry breaking in the excitation conditions [36, 38, 39].

Extrinsic chirality has emerged as a powerful mechanism for generating chiroptical responses in otherwise achiral nanostructures. This effect originates from the interaction between light and periodic surfaces under oblique illumination. The oblique incidence introduces in-plane momentum components that satisfy the momentum-matching condition required for SPP excitation. Consequently, the symmetry of the excitation field with respect to the nanostructure is broken, leading to distinct coupling behaviors for right- and left-circularly polarized light. This asymmetric interaction produces angle-dependent CD, where the difference in transmittance (ΔT) between RCP and LCP light results in a measurable CD signal, despite the achiral nature of the structure itself [40, 41, 42].

In the first part of this study, we use achiral gold nanohole arrays whose resonance band could be spectrally tuned by tailoring their geometric parameters, providing a flexible platform for enhancing CD signals through extrinsic chirality. Our analysis shows that the observed CD enhancement arises from chiral near fields that can be characterized by the chirality enhancement factor (χ), which encompasses both biolayer and substrate, and integrates electric and magnetic dipolar resonances. In our approach, we generate extrinsic chirality by tilting an achiral nanostructured substrate with respect to the incident light, which circumvents the need for inherently chiral geometries and offers tunable control over the chiroptical response.

1.3.3 Intrinsic Chirality Through Chiral Plasmonic Nanoparticle Assemblies

Another major category of nanoplasmonic enhancement structures is the assembly of plasmonic nanoparticles into intrinsically chiral configurations, representing a distinct conceptual class of chiroptical platforms. The concept of generating optical chirality purely from the spatial arrangement of achiral nanoparticles has opened one of the most innovative directions in nanoplasmonics. When achiral nanoparticles are arranged into chiral geometries, collective plasmon–plasmon coupling gives rise to hybridized optical modes that produce strong circular dichroism under normal incidence [37]. Early work in this area demonstrated that chirality can emerge solely from geometry. For example, Yan et al. showed that isotropic nanoparticles self-assembled into chiral pyramidal clusters exhibit measurable optical activity despite the achirality of their constituents [43]. Similarly, twisted nanorod dimers and nanoparticle helices formed using DNA-origami scaffolds revealed that precise positional control at the nanoscale can yield substantial chiroptical responses. These studies were

essential in establishing the fundamental mechanism by which geometric asymmetry, rather than material chirality, drives plasmonic circular dichroism [44].

However, while conceptually powerful, these systems are intrinsically limited in scale: DNA-templated assemblies, small chiral clusters, and chemically synthesized oligomers typically produce micron-scale structures and do not translate into wafer-scale, uniform, or device-ready chiral metasurfaces. Their chiroptical response, although strong, is restricted to small ensembles and is difficult to integrate into large-area biosensing or photonic platforms.

Motivated by these limitations, recent advances have shifted toward true scalable bottom-up fabrication capable of producing macroscopic chiral metasurfaces. A landmark example is the colloidal cross-stacked nanoparticle architecture introduced by Probst et al. [45], wherein densely packed nanoparticle chains are assembled via capillarity-assisted deposition and subsequently stacked at controlled angles. This simple geometric transformation converts two achiral layers into a three-dimensional intrinsically chiral metasurface which surpassing many top-down lithographic approaches by orders of magnitude. Crucially, the interlayer gap hosts intense, accessible superchiral hotspots where electric and magnetic fields become co-localized, enabling a tenfold enhancement in chiral biomolecule detection. The scalability, uniformity, and analyte accessibility of this design highlight its importance as the first bottom-up approach capable of generating device-level intrinsic chirality.

Building on these developments, the second part of my thesis introduces a related but distinct strategy based on creating intrinsically chiral visible-near field environments through cross-stacked plasmonic nanoparticle gratings integrated with a metal–dielectric optical cavity. While cross-stacked geometries alone already support strong chiral fields, integrating them with a thin-film cavity provides additional degrees of freedom for spectral tuning, field localization, and electromagnetic mode hybridization. In our design, two oriented gratings of gold nanoparticle dimers are positioned above an Au/Al_2O_3 multilayer, forming what we refer to as a Nanoparticle on-Mirror (NPoM) cavity. The cross-stacked nanoparticle geometry imparts genuine three-dimensional chirality, whereas the underlying photonic resonator introduces cavity modes and field confinement that cannot be achieved by the nanoparticle assembly alone. The coupled system supports hybrid optical resonances combining localized plasmons, Rayleigh anomalies (RA), surface lattice resonances, and cavity-induced magnetic responses, thereby generating highly structured superchiral fields whose intensity and spatial distribution can be tailored through both nanoparticle and cavity parameters [46, 47].

In this part of our study, we therefore employ nanophotonic plasmonic cavities that combine the intrinsic chirality of cross-stacked nanoparticle assemblies with the field-confining

and magnetic-dipole characteristics of the underlying resonant cavity, providing a platform specifically optimized for circular dichroism enhancement.

1.4 Structure of the Thesis

This thesis presents a systematic investigation into enhancing molecular CD response using designed plasmonic and photonic nanostructures. Our study is structured according to the following strategic phases:

(i) Initial Achiral Proof-of-Concept: We conducted detailed numerical and experimental measurements of the CD response of a tilted single gold nanohole array as a substrate.

(ii) Plasmonic Enhancement Validation: We used L-phenylalanine as a chiral biolayer target and studied its CD response in two conditions—isolated and placed on the single gold nanohole array—to quantify the enhancement factor (χ).

(iii) Engineering Enhanced Extrinsic Chirality Using Metal-Dielectric-Metal (MDM) Cavities: We then pursued improvement through the MDM cavity structure. This structure, composed of Au/Al_2O_3/Au with nanoholes in the top gold layer, was fabricated to exploit the effect of the photonic resonator for increased CD enhancement. The primary goal was to combine plasmonic, proving to be a highly promising platform for achieving strong CD signal amplification compared to the single gold nanohole layer.

Recognizing the exceptional field confinement achieved by the MDM cavity architecture, particularly due to the underlying Au/Al_2O_3/Au resonant stack, we sought a chiral platform that could provide comparable enhancement through intrinsic, rather than extrinsic, asymmetry:

(iv) Intrinsic Chiral NPoM Cavity Development: This strategic shift led to a second, distinct project, commenced during my research secondment at the Leibniz Institute for Polymer Research (IPF) in Germany. We developed a new intrinsic chiral cavity structure, the grating-patterned NPoM cavity. This platform integrates cross-stacked dimer gratings of gold nanoparticles assembled above a planar metallic substrate composed of Au/Al_2O_3 layers, leveraging the geometrical asymmetry of the cross-stacked layers to create ultra-strong superchiral hotspots within the plasmonic nanogaps. The NPoM design thus advances the plasmon-assisted chiroptical sensing approach by maximizing the field's strength and accessibility through inherently chiral structural design.

Chapter 2

Theoretical Principles of Chirality and Substrate-Enhanced Circular Dichroism Spectroscopy

2.1 Classical Electromagnetic Theory of Chiral Media

A in-depth understanding of chiroptical enhancement requires defining the electromagnetic behavior of chiral matter through modified constitutive relations derived from Maxwell's equations. In linear, isotropic, non-chiral media, the fundamental Maxwell equations are closed by standard constitutive relations, $D = \varepsilon E$ and $B = \mu H$, where ε and μ are the permittivity and permeability of the medium, respectively [48].

However, in a chiral medium, the electric displacement field (D) is influenced by both the electric field (E) and the magnetic field (H), necessitating a modification of these relations to account for magneto-electric coupling. The general constitutive relations for isotropic, reciprocal chiral media are expressed using the Pasteur parameter (κ_i), which quantifies the material chirality [49, 50]:

$$D = \varepsilon_i E - j\kappa_i \sqrt{\varepsilon_0 \mu_0} H \tag{2.1}$$

$$B = \mu_i H + j\kappa_i \sqrt{\varepsilon_0 \mu_0} E \tag{2.2}$$

Here, ε_i and μ_i are the permittivity and permeability of the chiral sample, ε_0 and μ_0 are the corresponding vacuum values, and κ_i is the dimensionless Pasteur parameter, which quantifies the strength of electromagnetic coupling between the electric and magnetic fields in a chiral medium. The sign of κ_i differentiates between right- and left-handed chiral media (enantiomers). These coupled constitutive relations confirm that the RCP and LCP components propagate independently within the chiral medium, experiencing distinct effective refractive indices ($n_\pm$). The imaginary component of κ_i is directly responsible for the differential absorption loss, which is the physical origin of circular dichroism [40].

Building on the electromagnetic description of intrinsic circular dichroism, it is also important to consider that measurable CD signals can arise in achiral systems through geometric or illumination asymmetry. Such extrinsic chirality can effectively act as a substrate-assisted enhancement for the CD response of chiral molecular layers, which we examine in the following section on its intrinsic CD. This phenomenon does not rely on the material's internal handedness but instead results from the broken symmetry between the incident wavevector and the structure's orientation. To establish a unified theoretical foundation, the next section formulates the CD signal within this tilted illumination framework, illustrating how symmetry breaking in the light–matter interaction can induce chiroptical effects even in nominally achiral planar systems.

2.2 Circular Dichroism (CD) Characterization in Tilted Illumination

In general, the CD signal is defined as the differential absorption or transmission between RCP and LCP light. If I_R and I_L represent the transmitted power intensities for RCP and LCP excitations, respectively, the CD signal is defined as [22]:

$$\mathrm{CD} = \tan^{-1}\left(\frac{I_R - I_L}{I_R + I_L}\right) \tag{2.3}$$

This expression quantifies the imbalance in transmission between the two helicities of light, providing a direct measure of the chiroptical response of the system. In the following, we explore a mechanism that intentionally breaks symmetry, enhancing the transmission imbalance and thereby increasing the CD signal.

2.2.1 Tilt-Induced Symmetry Breaking and Its Effect on Chiroptical Response

In intrinsically achiral planar nanostructures, circular dichroism does not arise under normal incidence because the system preserves mirror symmetry with respect to the incident light. However, this symmetry can be intentionally broken by tilting the incident wavevector k, introducing extrinsic chirality. This concept, often referred to as wavevector engineering, enables tunable control over the chiroptical response without modifying the geometry of the structure itself.

When a planar achiral nanostructure is illuminated at oblique incidence, the tilt breaks the mirror symmetry relative to the incident light. The magnitude of the wavevector in free space is $k_0 = 2\pi/\lambda$. When the sample is tilted, the wavevector is defined by the polar angle (θ, the tilt angle between k and the surface normal) and the azimuthal angle (ϕ, the rotation angle in the plane) [51, 35]:

$$k = k_0\big(\sin\theta\cos\phi,\, \sin\theta\sin\phi,\, \cos\theta\big) \tag{2.4}$$

The angular tilt introduces non-zero in-plane momentum components:

$$k_x = k_0\sin\theta\cos\phi \quad \text{and} \quad k_y = k_0\sin\theta\sin\phi \tag{2.5}$$

These components are crucial because they satisfy the momentum-matching condition required for the efficient excitation of resonant modes, such as surface plasmon polaritons or surface lattice resonances (SLRs), on the periodic nanostructures [52, 53].

2.2.2 The Polarization Basis and Circular States

The symmetry-breaking mechanism is physically understood by examining how the angularly dependent incident field interacts with the structure. The incident electric field $E = E_0 e^{i(k\cdot r)}$ is expressed as a superposition of the orthogonal S-polarized ($\hat{e}_s$) and P-polarized ($\hat{e}_p$) basis vectors, which are defined relative to the plane of incidence determined by θ and ϕ.

The Cartesian coordinate system $(\hat{x}, \hat{y}, \hat{z})$ is employed to describe the incident wave and polarization basis vectors. The incident wave vector $\vec{k}$, defined by the incidence (polar) angle θ and azimuthal angle ϕ, is:

$$\vec{k} = k_0\big(\sin\theta\cos\phi\hat{x} + \sin\theta\sin\phi\hat{y} + \cos\theta\hat{z}\big) \tag{2.6}$$

The s-polarization unit vector $\hat{e}_s$ perpendicular to the plane of incidence (and thus orthogonal to both $\vec{k}$ and the surface normal $\hat{z}$) is defined by [54, 55, 56, 57]:

$$\hat{e}_s = \frac{\hat{z}\times\vec{k}}{|\hat{z}\times\vec{k}|} \tag{2.7}$$

Computing the cross product explicitly:

$$\begin{aligned}\hat{z}\times k &= k_0\big[\sin\theta\cos\phi\,(\hat{z}\times\hat{x}) + \sin\theta\sin\phi\,(\hat{z}\times\hat{y})\big] \\ &= k_0\big[\sin\theta\cos\phi\hat{y} - \sin\theta\sin\phi\hat{x}\big]\end{aligned} \tag{2.8}$$

Followed by normalizing, which removes k_0, we obtain:

$$\hat{e}_s = -\sin\phi\hat{x} + \cos\phi\hat{y} \tag{2.9}$$

The P-polarization unit vector $\hat{e}_p$ lies within the plane of incidence, orthogonal to both $\vec{k}$ and $\hat{e}_s$. It is naturally defined via a cross product:

$$\hat{e}_p = \frac{\vec{k}\times\hat{e}_s}{|\vec{k}\times\hat{e}_s|} \tag{2.10}$$

so,

$$\hat{e}_p = -\cos\theta\cos\phi\hat{x} - \cos\theta\sin\phi\hat{y} + \sin\theta\hat{z} \tag{2.11}$$

Circularly Polarized Light (CPL) is defined by combining these linear components with a $\pm 90^\circ$ phase shift ($\pm i$), such that the RCP and LCP incident unit vectors, $\hat{e}^R$ and $\hat{e}^L$, are explicitly dependent on the tilt angles θ and ϕ.

The vector representation for the incident RCP light ($\hat{e}^R$) is

$$\begin{aligned}\hat{e}^R &= \frac{1}{\sqrt{2}}\left(\hat{e}_s + i\hat{e}_p\right) \\ &= \frac{1}{\sqrt{2}}\Big[\left(-\sin\phi + i\cos\theta\cos\phi\right)\hat{x} + \left(\cos\phi + i\cos\theta\sin\phi\right)\hat{y} - \left(i\sin\theta\right)\hat{z}\Big]\end{aligned} \tag{2.12}$$

The vector representation for the incident LCP light ($\hat{e}^L$) is

$$\begin{aligned}\hat{e}^L &= \frac{1}{\sqrt{2}}(\hat{e}_s - i\hat{e}_p) \\ &= \frac{1}{\sqrt{2}}\Big[(-\sin\phi - i\cos\theta\cos\phi)\hat{x} + (\cos\phi - i\cos\theta\sin\phi)\hat{y} + (i\sin\theta)\hat{z}\Big]\end{aligned} \tag{2.13}$$

Equations 2.12 and 2.13 explicitly show the critical role of the incident angles θ and ϕ on the polarization state. For the polar angle (θ), a non-zero tilt ($\theta \neq 0$) introduces a non-zero longitudinal component ($E_z \propto \sin\theta$) to the electric field vector. The ratio between the S and P components, which the achiral structure interacts with differently, is fundamentally changed when $\theta \neq 0$, leading to asymmetric coupling. The azimuthal angle ϕ dictates the specific rotation of the transversal (x, y) components of the incident field relative to the periodic structure's lattice orientation. The $\sin\phi$ and $\cos\phi$ terms in the E_x and E_y components determine the plane of incidence, which is essential for satisfying the momentum-matching condition ($k_{||}$) required for exciting surface resonances [58, 59].

This angular dependence ensures that the achiral structure couples differently to the S and P components, whose weighting in the incident CPL field is determined by θ and ϕ.

2.2.3 Dependence of the CD Response on Tilt

Tilting the sample introduces angular components to the incident field. The field for each circular polarization can be expressed as $\vec{E}^{L/R} = \vec{E}_0^{L/R} e^{i(\vec{k}\cdot\vec{r})}$. When the incident angle increases from normal incidence, the longitudinal field component (E_z) and the altered weighting between the S and P contributions change the overlap between the incident field and the structure's resonant modes. As a result, the transmitted electric fields for the two circular polarizations acquire distinct amplitudes and phase profiles. Since the transmitted intensity is proportional to the squared magnitude of the field, $T \propto |\vec{E}|^2$. the transmission

difference $\Delta T = T_R - T_L$ becomes explicitly dependent on the incidence angle θ. This asymmetry directly manifests in the measurable CD response, which is quantified by the transmission difference defined in Equation 2.3.

This angular dependence governs the strength of extrinsic chirality: as the tilt increases, the asymmetry between RCP and LCP interactions initially grows due to enhanced in-plane coupling. Beyond a certain range, however, the mismatch between the illumination geometry and resonance condition causes the effect to weaken. Consequently, both theoretical modeling and experiments predict a parabolic dependence of ΔT (and thus of the CD signal) on θ.

2.3 Intrinsic Circular Dichroism (CD_b) of an Isolated Biolayer

The fundamental electromagnetic description of chiral media provides the basis for quantifying the intrinsic CD response of an isolated chiral biolayer. This conventional scenario considers the chiral sample as a homogeneous slab of thickness w_b, placed in free space. To analytically compute the CD signal of an isolated biolayer (CD_b), the transmission amplitudes for RCP and LCP excitations are found separately at normal incidence. This calculation requires solving a boundary value problem expressed in an 8×8 matrix. By inserting the resulting transmission intensities into equation 2.3, the analytical expression for the CD response of the biolayer is derived as [60]:

$$CD_b = -\tan^{-1}\left[tanh\big(2k_0 w_b \mathrm{Im}\{\kappa_b\}\big)\right] \tag{2.14}$$

where $k_0 = 2\pi/\lambda$ is the magnitude of the wavevector in free space, w_b is the thickness of the biolayer, and $\mathrm{Im}\{\kappa_b\}$ is the imaginary part of the Pasteur parameter, representing chiral loss. For very thin chiral layers, where $k_0 w_b \ll 1$, the expression simplifies into the linear relationship [61].

$$CD_b \approx -2k_0 w_b \mathrm{Im}\{\kappa_b\} \tag{2.15}$$

This linear scaling reveals that the intrinsic CD signal is proportional to both the material chirality and the film thickness. The fact that these intrinsic signals are typically weak

necessitates employing strategies, such as nanophotonic substrates, to enhance the interaction locally.

2.4 Generalized Analytical Model for Substrate-Enhanced CD (CD_{total})

To identify the parameter that impacts the spectral maxima of the CD signal, we adopted an analytical approach, in which the CD was calculated following equation 2.16 [61]. The results were compared with those of finite element simulations, demonstrating good agreement, which validates our previous modeling approach.

$$CD_{total} = CD_s + \left\{ \frac{k_0 w_b \mathrm{Im}\{\varepsilon_b\}}{2\sqrt{\mathrm{Re}\{\varepsilon_b\}}} \left(\mathscr{F}_L - \mathscr{F}_R\right) + \frac{CD_b}{2} \left(\chi_R + \chi_L\right) \right\} sech\left(4k_0 w_s \mathrm{Im}\{\kappa_s\}\right) \tag{2.16}$$

Equation 2.16 calculates the total CD of the structure, taking both the contribution of the nanohole array (CD_s) and the biolayer (CD_b) into account. κ_s and w_s represent the Pasteur parameter and thickness of the substrate, respectively. The parameter $\mathscr{F}_{L(R)}$ represents the local intensity factors determined by ($\mathscr{F}_p^{loc} = (|E|^2_{near})/(|E|^2_{far})$), and $\chi_{L(R)}$ denotes the chiral enhancement factors ($\chi_P^{loc} = \mathrm{Im}\{E \cdot H^*\}_{near}/\mathrm{Im}\{E \cdot H^*\}_{far}$) [41]. The χ factor is calculated by averaging χ across all points in the specified volume. Specifically, the near-field zone is defined as a volume of the same size as the chiral sample, immediately on top of the substrate, while the far field extends to the end of the physical simulation domain. We conducted full-wave range calculations of the CD signal for three configurations: a single nanohole array, a biolayer on glass, and a gold nanohole array-supported biolayer [32].

Equation 2.16 provides analytical insights into two influential factors: the sech coefficient and the χ factor. The former represents the chiral absorption of the substrate ($k_0 w_s \mathrm{Im}\{\kappa_s\}$) in the CD spectroscopy and is weak, while χ plays a crucial role in enhancing CD of the biolayer. Maximizing χ requires regions where E and H fields are strong, co-localized, and possess a non-zero phase difference. This requirement means that simply boosting the electric field intensity is insufficient; true chiral enhancement requires the generation of strong magnetic field components (H) as well, ensuring a robust coupling term $\mathrm{Im}\{E \cdot H^*\}$. To achieve this and drastically increase detection sensitivity, platforms are designed to create highly

localized, strongly twisted electromagnetic fields, commonly referred to as "superchiral" fields, in the vicinity of the biolayer.

2.5 Nanophotonic Substrate Mechanisms for Optimal CD Enhancement

2.5.1 Chiroptical Amplification via chiral MDM Cavities

We begin by considering a tilted single-layer gold nanohole array and its capacity to generate a chiroptical response in the presence of a chiral medium. This substrate-mediated CD can be further enhanced by integrating the nanostructure with an optical cavity, such as an MDM configuration which includes Au/Al_2O_3/Au nanohole array (as shown in Figure 5.5a) [62, 63]. Within the MDM cavity, the electromagnetic fields interact with both the metallic and dielectric layers, producing characteristic current and displacement distributions. Specifically, the alternating metal and dielectric layers support the formation of closed-loop displacement currents, which give rise to localized magnetic dipole resonances [64]. According to the Biot–Savart law, a current loop generates a magnetic field whose direction and magnitude are determined by the shape and intensity of the circulating current [65]; in this context, the closed-loop displacement currents produce strong magnetic fields that spatially overlap with the electric field, creating regions of high optical chirality density. In contrast, a single-layer gold nanohole array does not support such circulating currents, and its chiroptical response is dominated by comparatively weaker electric-dipole interactions rather than the combined electric- and magnetic-dipole modes present in the MDM cavity architecture [64].

2.5.2 NPoM Cavities and Their Hybrid Mode Coupling for Enhanced Chiral Sensing

Another class of nanophotonic cavity is the grating-patterned NPoM structure [66, 67], in which two stacked layer of gold nanoparticle dimers are positioned above a continuous gold film and separated by a nanometric Al_2O_3 spacer (as shown in Figure 3.7). This configuration forms gap cavities that support confined plasmonic modes, enabling strong local-field enhancement and significant amplification of circular dichroism signals. In these NPoM cavities, the interaction of diffractive resonance such as Rayleigh anomalies [68] with

the fundamental electromagnetic resonances in the cavity plays a critical role in shaping the spectral and distribution of the optical fields. These couplings influence the field confinement, and ultimately the chiroptical response of the system.

2.5.2.1 Fundamental Resonant Modes

The NPoM system relies on the interplay of several fundamental electromagnetic resonances. The Localized Surface Plasmon Resonance (LSPR) [69] involves the collective, non-propagating oscillation of free electrons within individual metal nanoparticles, generating sharp spectral features and strong electromagnetic near-field enhancements. SPPs [70] are propagating electromagnetic waves coupled to the electron oscillations at a metal-dielectric interface. They are commonly excited either by prism-coupling in planar films (Kretschmann/Otto geometries) or by periodic nanostructures such as gratings, which provide the required momentum via reciprocal lattice vectors. The Guided Mode Resonance (GMR) [71] is a photonic effect that occurs in periodic waveguide structures when a diffracted order is phase-matched to propagate as a guided mode within the waveguide layer, leading to sharply resonant spectral variations.

2.5.2.2 The Role and Types of Rayleigh Anomaly (RA)

Rayleigh Anomalies (RAs) arise in periodic nanostructures when a diffracted order transitions between being propagating and evanescent. Physically, an RA marks the wavelength at which a grating order begins to graze along the surface, causing a sudden redistribution of optical energy. This redistribution often manifests as sharp features in transmission or reflection spectra and, importantly, provides phase-matching conditions that enable coupling to guided or plasmonic modes [72].

For a periodic structure with lattice period Λ , illuminated by light of wavelength λ at incident angle θ, with n_{medium} the refractive index of the medium into which the diffracted order is directed, the condition for the mth diffraction order to become grazing (transition to/from propagation) is [73]

$$\lambda_{RA} = \frac{\Lambda}{m}\Big(n_{medium} \pm \sin\theta\Big) \tag{2.17}$$

In an asymmetric structure like the NPoM cavity, two distinct types of RAs emerge, dependent on the surrounding medium's refractive index (n):

- RAs (Substrate Rayleigh Anomaly) occurs at the interface with the substrate (below the nanostructure). Since the substrate refractive index (n_s) is typically high (e.g., glass $\approx$1.45), RAs appears at longer wavelengths.
- RAc (Cover Rayleigh Anomaly) occurs at the interface with the cover medium (above the nanostructure). Because the cover refractive index (n_c) is generally lower (e.g., air $\approx$1.0), RAc appears at shorter wavelengths for the same grating period [46].

2.5.2.3 Mode Hybridization and Chiral Enhancement

The precise spectral and angular coincidence of the RA provides the momentum for efficient coupling between the grating and other confined modes. This mode hybridization is crucial for concentrating electromagnetic energy. In RA-GMR coupling, the RA wavelength spectrally coincides with a guided mode resonance, and the diffracted orders efficiently extract the energy stored in the guided mode, producing a narrow and intense spectral peak . In the case of RA-SPP/LSPR coupling, the RAs couple with SPP and LSPR modes to generate hybrid resonances (often Fano-shaped) that combine the large scattering cross-section of plasmons with the diffractive orders, thereby maximizing field enhancement. The strong electromagnetic confinement achieved through these hybrid modes boosts the local optical chirality enhancement factor, $\chi \propto \mathrm{Im}\{E^* \cdot H\}$, which is the physical prerequisite for significant CD enhancement [74, 75, 76].

The schematic in Figure 2.1 summarizes the optical modes and hybrid interactions supported by the nanoparticle-on mirror metasurface incorporating an Al_2O_3 dielectric spacer. In the case of the transverse localized surface plasmon resonance (LSPR(T)), the incident light polarization is perpendicular to the particle gratings, so only the nanogap hotspots formed across the dimer axis (transverse to the grating direction) are excited. The electric field is driven across the dimer axis and becomes tightly confined within the nanogap, corresponding to the shorter-wavelength resonance that couples efficiently to the cover-side Rayleigh anomaly. For the longitudinal localized surface plasmon resonance (LSPR(L)), the incident light polarization is parallel to the particle gratings, exciting the longitudinal (super-radiant) mode. This configuration produces very strong electromagnetic enhancement along the particle gratings. The longitudinal mode appears at longer wavelengths compared to the transverse resonance, because all dipoles align head-to-tail, their near fields add constructively along the chain, and this strong longitudinal coupling lowers the mode energy, shifting the resonance to longer wavelength than the weakly coupled transverse mode. Within

the Al_2O_3 spacer, grating-mediated coupling excites guided-mode resonances (GMRs), depicted as green propagating fields. As these guided modes intersect the substrate-side Rayleigh anomaly (RAs), they form GMR–RAs hybrids that radiate into the ± 1 diffraction channels. To the right, phase matching between the grating and the metal film launches a surface plasmon polariton along the Au/glass interface, shown as a tightly confined surface wave. When the SPP dispersion couples with the Rayleigh anomaly, an SPP–RAs hybrid is formed, combining strong interface localization with diffractive leakage. Overall, the figure highlights the coexistence and hybridization of LSPR(L), LSPR(T), GMR, RA, and SPP modes, which collectively define the resonant behavior of the metasurface.

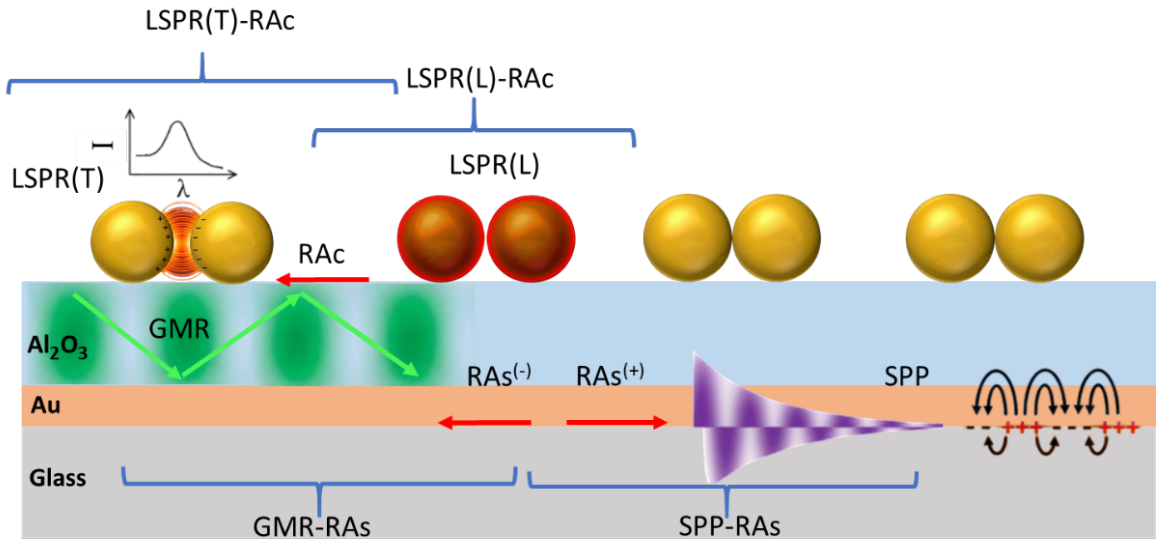

Figure 2.1 Schematic of LSPR(L), LSPR(T), GMR, RA, and SPP modes in the metasurface and their associated hybrid interactions.

2.5.3 Collinear E-H Alignment in Plasmonic Cross-Stacked Dimer Arrays

The cross-stacked configuration of the dimer nanoparticle arrays (or dimer gratings) within the NPoM cavities is used to maximize field enhancement by creating ultra-confined inter-layer vertical nanogaps. Primarily, the architecture is highly effective at generating collinear electric and magnetic field alignment ($E \parallel H$) necessary to maximize the chirality enhancement factor $\chi \propto \mathrm{Im}\{E^* \cdot H\}$. When the localized plasmon mode is excited, the oscillation of electrons in the metallic nanogap drives a strongly enhanced electric field component normal to the surface (along the vertical z-axis, E_z). This intense field compression inside the nanogap

induces circulating displacement currents that loop around the nanoparticle edges while simultaneously flowing vertically across the gap. According to the Biot–Savart law, these circulating currents generate a magnetic field component that is also oriented predominantly along the z-direction. Thus, both the electric and magnetic fields become spatially co-localized and aligned (collinear) within the nanogap region. This directional overlap is precisely what amplifies the chirality enhancement factor, since χ increases when E and H share both direction and phase [77]. Furthermore, the introduction of a cross-stacked geometry strengthens hybridization between the localized LSPR mode and the collective lattice-supported photonic/plasmonic modes. This coupling sharpens the resonance and increases the energy stored in the nanogap. Finally, because the strongest superchiral fields are concentrated directly in the inter-layer nanogap, the chiral "hotspot" remains fully accessible to analyte molecules, maximizing the field–matter interaction volume and enhancing CD sensitivity.

In summary, this chapter has outlined the theoretical basis for chiroptical enhancement in nanostructured plasmonic systems. Beginning with the classical electromagnetic description of chiral media, we examined how intrinsic and extrinsic chirality lead to differential light–matter interactions under circularly polarized illumination. We then discussed how nanopatterned substrates such as MDM and NPoM cavities generate superchiral near-fields through hybridization between guided-mode, plasmonic, and Rayleigh anomaly resonances. Building on these principles, the next chapter turns to the practical realization of these architectures, detailing the fabrication procedures used to produce the nanophotonic substrates investigated in this work.

Chapter 3

Fabrication Methodology of Achiral and Chiral Metasurface Cavities

The fabrication of the substrates was partitioned into two distinct methodological approaches. The first approach, utilized for the achiral single-layer gold nanohole arrays and the MDM cavities, relied on classical top-down fabrication, specifically Electron Beam Lithography (EBL) [78] combined with physical vapor deposition, to create geometrically precise gold nanohole gratings designed for chiroptical enhancement via extrinsic chirality (oblique illumination). The second approach, employed for the chiral NPoM cavity, was based on bottom-up self-assembly, leveraging Laser Interference Lithography (LIL) [79] masters and a Template-Assisted Self-Assembly (TASA) [80] technique to create nanoparticle dimer gratings whose chirality is intrinsic to their mechanically achieved layered geometry.

3.1 Fabrication of single-layer gold nanohole arrays substrate

The nanohole arrays were fabricated on a clean fused silica substrate (12×12 mm^2) using EBL. Initially, a positive electron-beam resist (PMMA, 950k A4) approximately 180 nm thick was spin-coated at 4000 rpm for 60 seconds and subsequently baked at 180°C for 5 minutes. The EBL exposure was performed using an acceleration voltage of 20 kV, a beam current of 45 pA, and an exposure dose of 120 μC/cm^2, with a writing speed of nearly 70 μm^2/s, to pattern arrays covering a 200×200 μm^2 area featuring nanohole diameters of

400 nm and a lattice constant of 530 nm. Following exposure, the resist was developed in a MIBK:IPA (1:3) solution for 60 seconds, rinsed with IPA, and dried under nitrogen. A conductive aluminium layer was temporarily deposited, and after aluminium removal, gold was deposited via electron beam evaporation at a rate of 0.6 Å/s onto the patterned substrate. Finally, the PMMA layer was removed using an ultrasonic acetone bath. The schematic of the fabrication process and the corresponding SEM image of the gold nanohole array substrate are shown in Figure 3.1 [32].

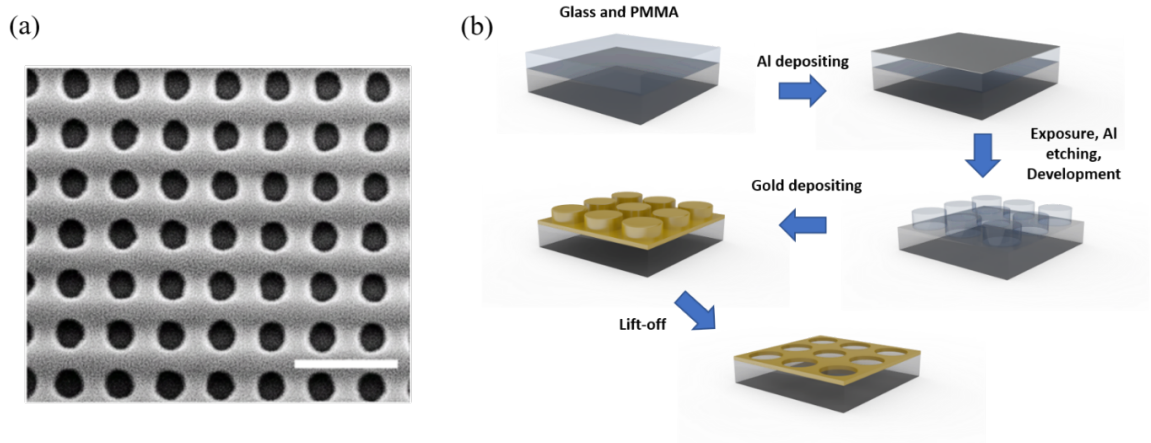

Figure 3.1 (a) SEM image of the fabricated periodic gold nanohole array exhibiting uniform morphology with a lattice periodicity of 530 nm and a nanohole radius of 200 nm. The scale bar corresponds to 500 nm. (b) Schematic illustration of the fabrication process for the single-layer gold nanohole array, including glass substrate cleaning, PMMA resist coating, aluminium hard-mask deposition for charge dissipation, electron-beam exposure, aluminium etching and resist development, gold deposition, and final lift-off.

3.1.1 Deposition of L-Phenylalanine Chiral Biolayer on Gold Nanohole Structures

As a chiral biolayer, the L-phenylalanine biolayer was deposited using thermal evaporation of L-phenylalanine powder (density 1.34 g/cm^3) at a controlled deposition rate of approximately 0.3 Å/s. The deposition was carried out at a substrate temperature of about 100°C under a high vacuum environment maintained at approximately 5×10^{-5} mbar, conditions carefully maintained to promote the formation of a homogenous layer. The film thickness was monitored using a QCM-based sensor (model SQC-330) in the thermal evaporator, which measures deposition rate and film thickness via quartz crystal microbalance. Atomic force microscopy (AFM) was employed to assess the uniformity of the approximately 60 nm

thick film, confirming minimal thickness variation and consistent surface morphology across multiple locations on the substrate, as shown in the AFM image Figure 3.2(a-b). A line profile, shown in Figure 3.2a, was extracted across a defined step on the film, confirming an average thickness of approximately 60 nm. Figure 3.2b presents a representative AFM topographic image, revealing the overall surface characteristics. The AFM analysis substantiates the formation of a continuous L-phenylalanine layer, suitable for its intended function as a chiral biolayer.

The fabrication protocol closely followed the method outlined in the reference [34], which utilized a similar thermal evaporation technique under comparable conditions. The optical transmission measurements of the bare L-phenylalanine film, displayed in Figure 3.2b, were recorded for S- and P-polarized light over the visible wavelength range, displaying a nearly flat profile without significant peaks or dips. Such a transmission signature indicates a uniform, continuous film with negligible scattering or inhomogeneities.

Thermal evaporation of L-phenylalanine was conducted at moderate temperatures ($\sim$100°C), well below its thermal decomposition onset (157-210°C), preserving molecular integrity during deposition. Thermogravimetric and calorimetric studies in the literature confirm L-phenylalanine's thermal stability below these temperatures. During CD measurements, illumination intensities and substrate temperatures were carefully controlled to avoid thermal or photochemical degradation, ensuring the photostability of the solid film [32, 81].

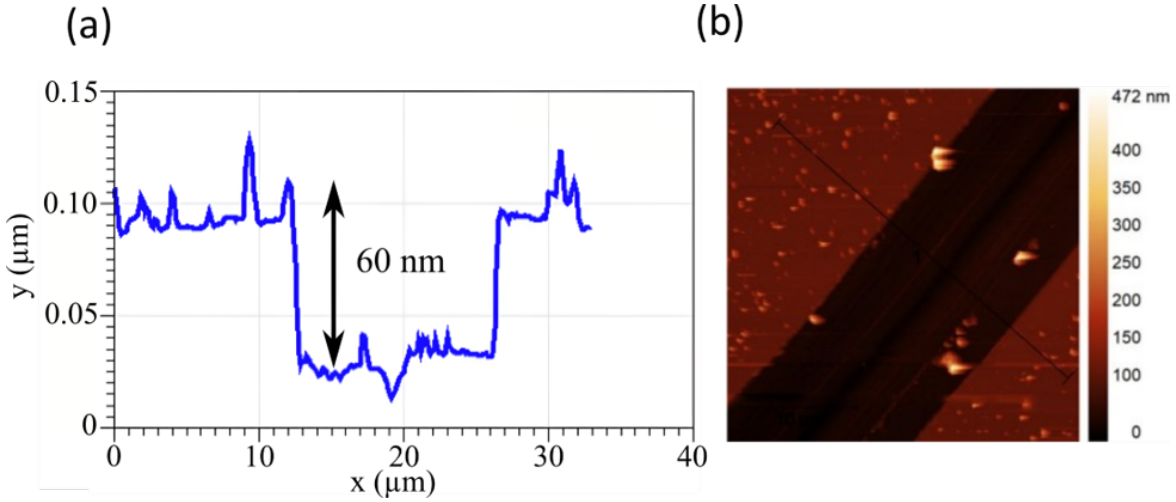

Figure 3.2 Atomic Force Microscopy (AFM) image (a) and corresponding height profile (b) of the thermally evaporated L-phenylalanine thin film on a glass substrate. Reproduced from ref [32]. Copyright 2020 American Chemical Society.

3.2 Fabrication of $Au/Al_2O_3/Au$ structure

A 12×12 mm^2 fused silica substrate was first coated with a 5 nm titanium adhesion layer, followed by deposition of a 30 nm gold layer and a 170 nm Al_2O_3 dielectric spacer via electron beam evaporation with a rate of 0.5 $/$s and 1 $/$s for the gold layer and dielectric spacer, respectively. A PMMA layer was then spin-coated on top of the Al_2O_3 surface, and nanohole arrays were patterned using EBL under the same conditions described above. After the development step, a 60 nm gold top layer was deposited, and lift-off was performed in an acetone bath. The resulting structure consisted of nanohole arrays embedded in the top gold layer, forming the final $Au/Al_2O_3/Au$ trilayer configuration, as schematically illustrated in Figure 5.5a. An SEM image of this configuration is displayed in Figure 3.3. The L-phenylalanine biolayer (60 nm thick) was deposited onto the $Au/Al_2O_3/Au$ structure via thermal evaporation, following the same procedure as for the single-layer sample [32].

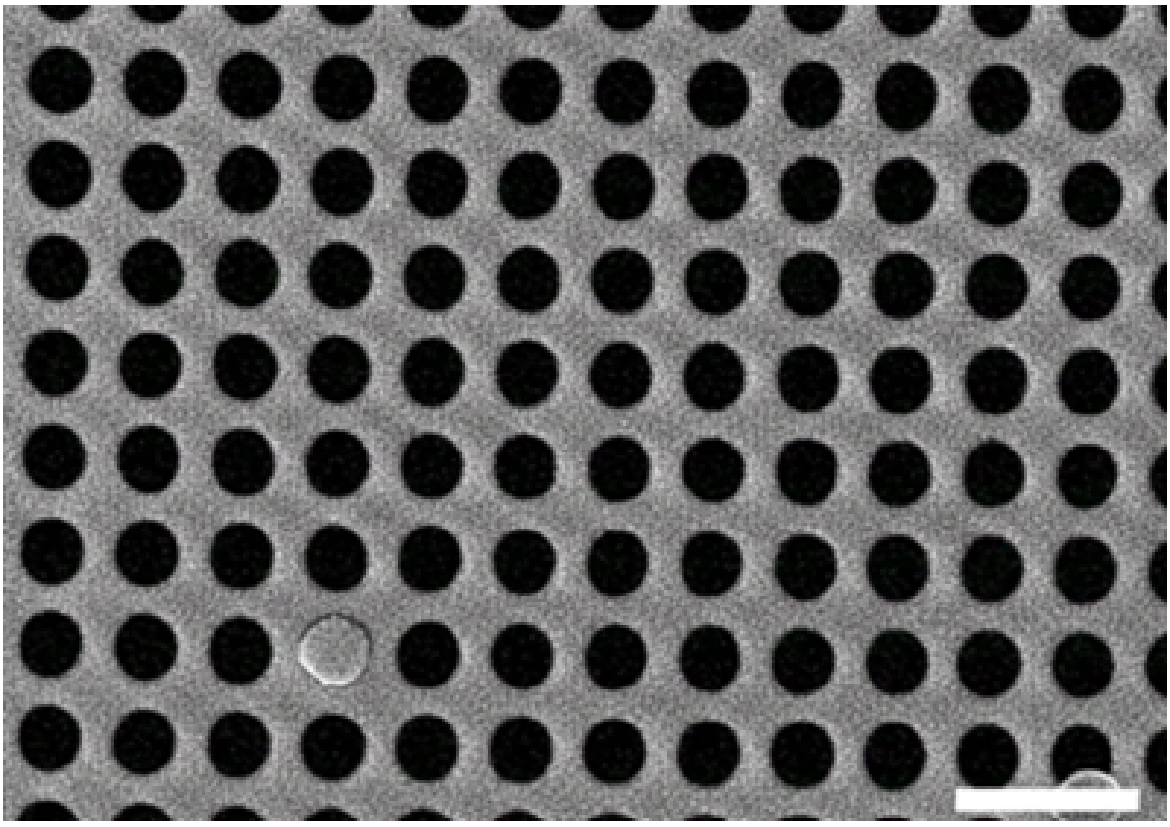

Figure 3.3 SEM image of the MDM-nanohole array fabricated on a glass substrate, consisting of a 170 nm Al_2O_3 layer sandwiched between a 30 nm bottom Au layer and a 60 nm top Au layer with nanoholes. The nanoholes have a radius of 200 nm and are arranged in a lattice with a 530 nm constant. Scale bar is 1 μm.

3.3 Fabricating NPoM Cavities with Cross-Stacked Nanoparticle Dimer Gratings

The NPoM structures utilize a hybrid architecture, combining a solid-state bottom cavity with a colloidally assembled gold nanoparticle grating. The fabrication process is schematically shown in Figure 3.5.

3.3.1 Molding and LIL-Template-Assisted Self-Assembly

Laser interference lithography was used to create the structured master template on a glass substrate. For this purpose, glass slides were cut into 20 mm $\times$ 20 mm pieces and were cleaned in a mixture of deionized (DI) water and isopropyl alcohol with a ratio of 1:1 by sonication at 37 kHz for 15 min. After sonication, the glass substrates were dried by a stream of compressed nitrogen. Spin-coating was used to deposit a negative photoresist (ma-N-405) on the cleaned glass substrates. The parameters of the spin-coating were 3000 rpm with an acceleration of 1000 rpm/s for 33 s. After the deposition of the photoresist, the substrate was baked at 100°C for 60 s and exposed to a 325 nm laser with a power of 150 μW/cm^2 for 5s. The back side of the glass substrate was covered with black adhesive tape to prevent any unwanted reflection during the exposure. The exposed glass substrate was immersed in a developer (ma-D 532/S) for 20 s, rinsed with DI water, and dried with nitrogen to develop the periodic structures. The periodic templates were fabricated using LIL, producing a photoresist master consisting of parallel ridges with a periodicity of 620 nm.

In the LIL setup, a continuous-wave He-Cd laser (325 nm) is used for exposure (Figure 3.4) [46]. The laser beam is directed through mirrors (M1, M2) and a spatial filter (MO, PH, L) to achieve an expanded and collimated beam. This beam propagates freely before being reflected by a mirror (M3) and directed towards the beam splitter (BS). The transmitted and reflected beams from the BS are further reflected by mirrors (M4, M5) to create the two interfering beams interacting with the photoresist-coated sample on the sample stage (SS). By adjusting the distance (z) of the sample stage (SS) from the midpoint of the line connecting mirrors M4 and M5 while keeping the mirror separation (d) fixed at 22 cm, we can control the interference angle (θ) and consequently the periodicity (λ) of the resulting structures. The angle of interference is given by $\theta = tan^{-1}(d/2z)$ whereas the periodicity is given by $\lambda = \lambda/[2\sin\theta] = \lambda/[2\sin(\tan^{-1}(d/2z))]$. This allows us to create a variety of structures with different periodicities. An electronic shutter (ES) controls the exposure time, while a

neutral density filter adjusts the laser intensity. The maximum patterned area achievable using LIL is dependent upon the dimensions of the collimated beam, which, in turn, is influenced by the spatial filtering setup. Employing a microscope objective with higher magnification, paired with a collimating lens of greater diameter, facilitates the generation of a pristine Gaussian beam. The size of this beam is limited only by the physical dimensions of the optical components incorporated within the setup. In the current configuration, this results in a patternable area that can extend up to a diameter of 25.4 mm.

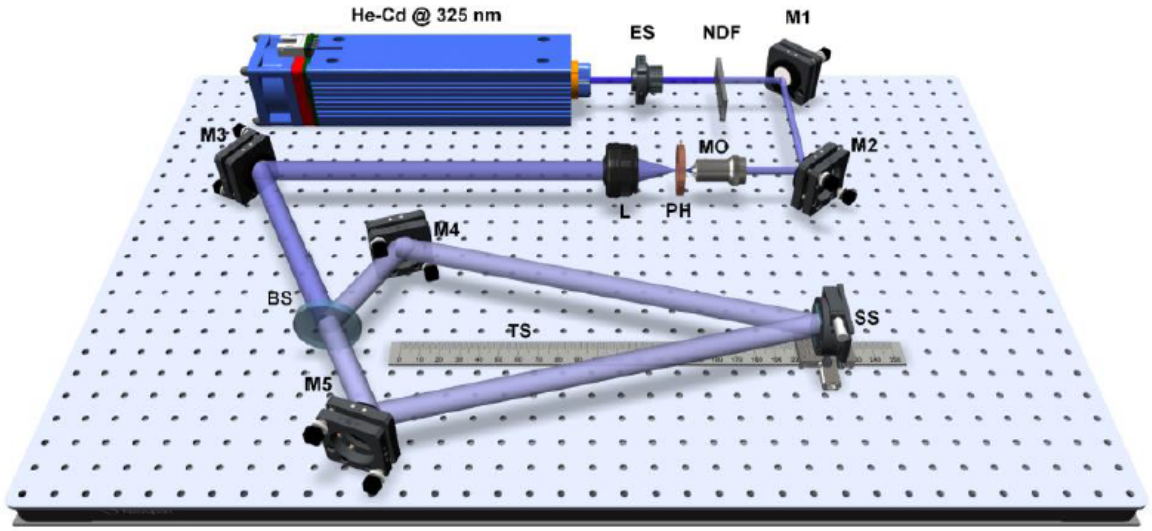

Figure 3.4 Schematic of the experimental setup for Laser Interference Lithography. He-Cd: Helium Cadmium Laser; NDF: ND Filter; M1, M2, M3, M4, M5: Plane mirrors, MO: Microscope Objective; PH: pin-hole; L: Collimating Lens; BS: Beam splitter; TS: Translation stage, SS: Sample stage. Reproduced with permission from Adnan et al. Adv. Opt. Mater. 2025, 13, 2403397. Copyright 2025 Wiley-VCH GmbH. [46]

As shown in Figure 3.5, after the periodic structure was developed, the glass master was modified by trichloro (1H,1H,2H,2H-peruorooctyl) silane (448931, Sigma-Aldrich) in a desiccator overnight. The modified glass master was molded by a silicone kit (Sylgard 184 Silicone Elastomer) and a curing agent with a mixture ratio of 10:1 to produce the elastomeric structured polydimethylsiloxane (PDMS). Furthermore, the mixture was cured at 50°C for 6 h. After the curing process, the structured PDMS template was peeled off of the glass master, and the unstructured areas were trimmed (Figure 3.6a). The nanoparticle gratings were produced using this PDMS template. First, a silica glass was divided into 20 mm $\times$ 20 mm pieces. The individual silica glass pieces were placed into a mixture of DI water and isopropyl alcohol with a ratio of 1:1. The silica glass substrates were cleaned by ultrasonication at 37 kHz for 15 min. Afterwards, they were dried under the stream of

nitrogen. 5 μl of the water-based colloidal dispersion of plasmonic nanoparticles with a 2.8 mg/mL concentration was drop cast onto the cleaned glass substrates via a micropipette. Afterward, the PDMS template was placed on the solution immediately. The colloidal solution was confined without an external force, ensuring close contact between the substrate and template [82]. The self-assembly process was carried out for 6 h at room temperature until the residual water was dried. The PDMS was then peeled off, leaving the particle dimer grating on the target substrate (Figure 3.6b). The nanoparticles have a diameter of 80 nm, while the grating channels of the PDMS template have a periodicity of 620 nm, guiding the particles to assemble as dimers within each channel.

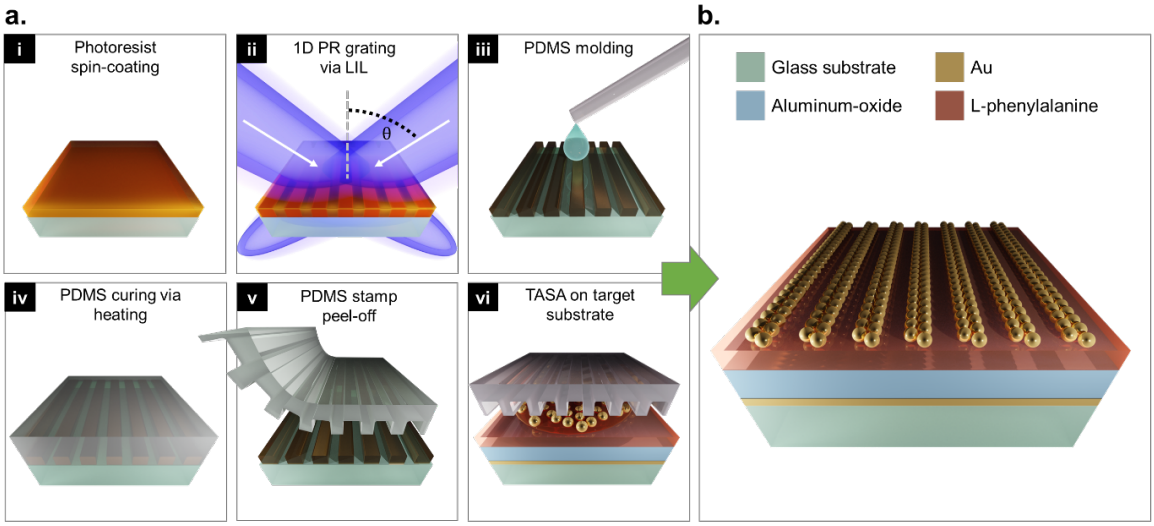

Figure 3.5 Schematic illustration of the fabrication process for single nanoparticle dimer chains. (a) Stepwise procedure: (i) spin-coating of photoresist, (ii) 1D grating patterning via LIL, (iii) PDMS molding, (iv) PDMS curing, (v) PDMS stamp peel-off, and (vi) Template-Assisted Self-Assembly of gold nanoparticles onto the target substrate. (b) Resulting nanoparticle dimer grating on the substrate, showing the arrangement of Au nanoparticles on glass/Al_2O_3/L-phenylalanine layers.

3.3.2 Comparative Substrate Engineering for Layer-Specific Analysis

To isolate the individual contributions of plasmonic and photonic layers to the overall chiral enhancement, we applied the single nanoparticle dimer grating sequentially to four distinct substrate configurations for comparative optical measurements as shown in Figure 3.7(a-d). These sequential structures included: Structure 1, a glass substrate (baseline); Structure 2, a glass/Au-coated substrate (30 nm Au) to isolate the effect of the planar metallic mirror;

Structure 3, a glass/Au/Al_2O_3 structure (30 nm Au, 170 nm Al_2O_3) to analyze the NP dimer grating interaction with the full MDM-cavity at the bottom; and Structure 4, the glass/Au/Al_2O_3 coated with a 60 nm L-phenylalanine film to introduce the chiral analyte into the structure before the final NPoM layer. The Au and Al_2O_3 thin films were deposited using electron-beam evaporation under the same conditions described earlier. Following the thin-film preparation, the nanoparticle chain arrays were placed onto each substrate using the same assembly procedure previously described for positioning the nanoparticle chains on glass.

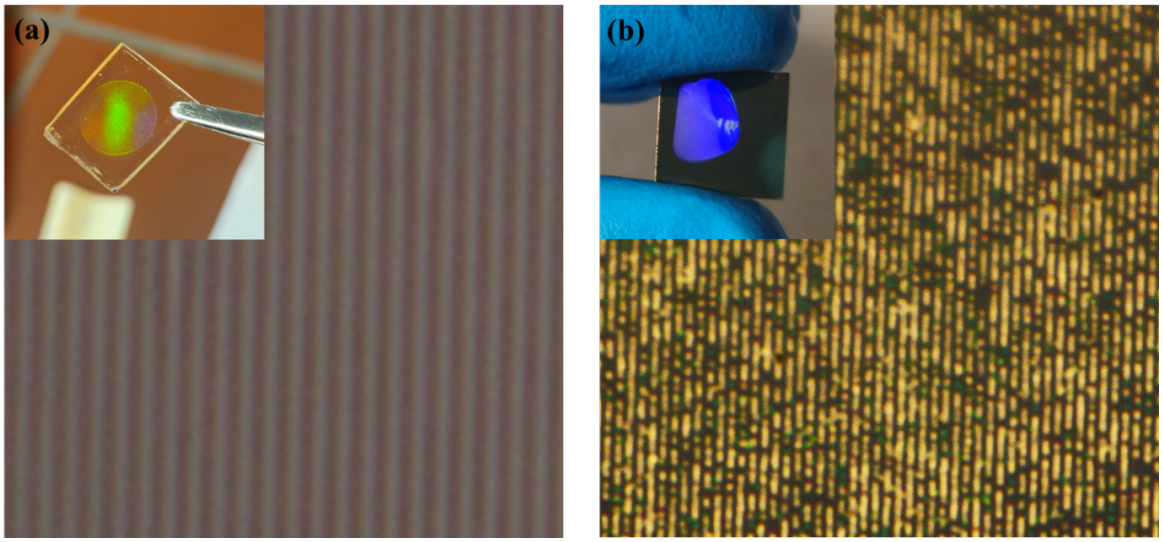

Figure 3.6 (a) Microscope image of the fabricated periodic PDMS grating exhibiting well-defined periodicity (620 nm). (b) Microscope image of self-assembled spherical plasmonic particles with 80 nm size on a dimer grating pattern fabricated on a glass/Au/Al_2O_3 multilayer substrate with gold and alumina thicknesses of 60 nm and 170 nm, respectively.

3.3.3 Tunable Chiral Induction in NPoM Structures via a Reversible Second-Layer (Cross-Stacked Nanoparticle Dimer Grating)

Finally, the chiral NPoM architecture was completed by adding a second, cross-aligned nanoparticle dimer layer on top of the first. The resulting geometric asymmetry is responsible for generating the enhanced chiral response. To achieve this, a second nanoparticle-loaded PDMS stamp (identical to the first) was laminated face-to-face onto the prepared single-layer structure (Figure 3.8). This technique resulted in a reversible bilayer structure (i.e., the second layer can be removed, reoriented, and restacked without permanent bonding). Crucially,

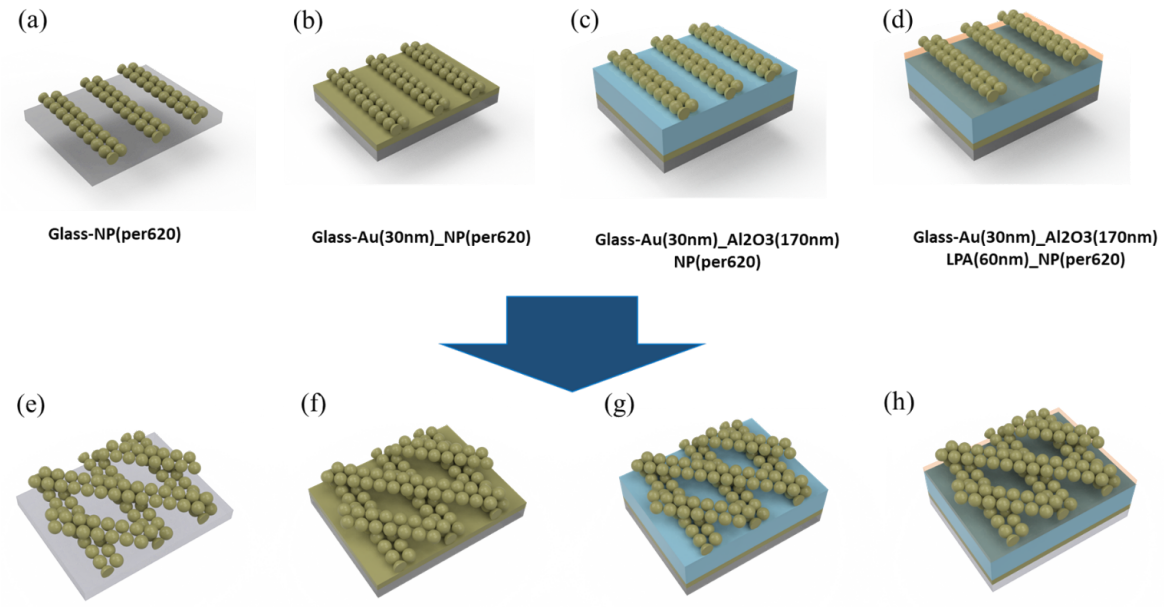

Figure 3.7 Schematic illustration of nanoparticle dimer grating architectures. The top row (a–d) depicts single-layer nanoparticle dimer gratings assembled on different substrate configurations: (a) glass, (b) glass/Au, (c) glass/Au/Al_2O_3, and (d) glass/Au/Al_2O_3/LPA. The bottom row (e–h) shows the corresponding stacked (bilayer) nanoparticle gratings for each structure above, where a second nanoparticle layer is laminated at a controlled oblique angle relative to the first, introducing chiral asymmetry. This stacked configuration enables a tunable and strong chiroptical response through reversible angular stacking and nanoscale gap coupling between the two layers.

the second layer was placed at a controlled cross-wise oblique stacking angle (15°, 30°, or 45°) relative to the direction of the first nanoparticle chains. This rotational misalignment creates the chiral geometry, allowing for reversible tuning of the CD response magnitude and sign via angular adjustment. The elastic nature of the PDMS allowed for repeated stacking and restacking to measure the CD spectra across these different angular configurations. The stacked layer was added on top of four distinct initial structures, as shown in Figure 3.7(e-h), to perform CD measurements separately.

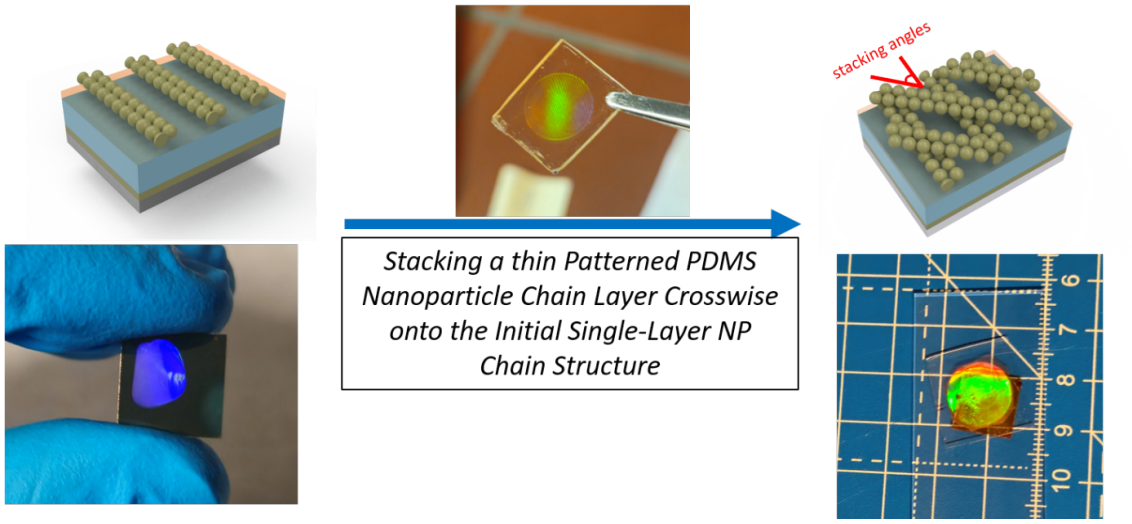

Figure 3.8 Schematic and photographic overview of the crosswise stacking of a thin patterned PDMS nanoparticle (NP) chain layer onto an initial single-layer NP chain structure. The process is used to control stacking angles and create multi-layered plasmonic nanostructures.

This chapter detailed the fabrication methodologies of all plasmonic nanostructures designed for chiroptical characterization. Achiral single-layer gold nanohole arrays and $Au/Al_2O_3/Au$ nanohole array cavities were precisely fabricated using electron beam lithography and physical vapor deposition, while a uniform 60 nm L-phenylalanine biolayer was thermally evaporated to introduce controlled molecular chirality. In parallel, intrinsically chiral NPoM cavities were realized through LIL and TASA to form nanoparticle dimer gratings. These diverse fabrication routes provided a comprehensive platform encompassing both extrinsic and intrinsic chirality mechanisms. The subsequent chapter focuses on the optical transmission and CD measurements performed on all fabricated structures to evaluate and compare their chiroptical responses.

Chapter 4

Optical Measurement and Electromagnetic Simulation of Achiral and Chiral Metasurface Cavities

The characterization of chiroptical metasurfaces demands an experimental setup capable of controlling the incident polarization and angle, complemented by robust numerical simulations to predict and validate the complex electromagnetic interactions. This chapter details the experimental and numerical protocols employed across both the achiral nanohole array studies (single-layer and MDM cavity) and the chiral NPoM cavity investigations.

4.1 Experimental Characterization of Achiral Metasurfaces

The measurement of CD enhancement in the achiral nanohole array structures (single-nanohole array and MDM-nanohole array) relied on generating extrinsic chirality by precisely tilting the sample. This necessitated a custom optical transmission setup capable of controlling the polarization state and the angle of incidence (θ and ϕ) with spatial accuracy for optimization.

4.1.1 Custom Optical Setup for Extrinsic Circular Dichroism

The chiroptical measurements were performed using an optical transmission setup designed to operate over the visible-to-near-infrared (Vis-NIR) range (400–800 nm). The setup's architecture, illustrated in a schematic (Figure 4.1a) and a photograph of the physical arrangement (Figure 4.1c), ensures accurate control over the illumination and detection path.

The key components and their functions are: A Xenon Lamp as the broadband light source, a focusing objective that collects the lamp output, and a second objective that collimates and directs the beam toward the sample. The collimated beam then passes through a linear polarizer, which defines a well-controlled linear polarization state, followed by an achromatic achromatic Quarter-Wave Plate (QWP), which is rotated to generate sequential Right Circularly Polarized (I_R) and Left Circularly Polarized (I_L) light states necessary for CD measurement. The circularly polarized beam is focused onto the sample surface using an objective lens (Thorlabs MY20X-824, 20×, NA = 0.4, WD = 8.24 mm). The sample is mounted on a custom-designed Rotatable Sample Holder, which is equipped with dual rotation axes as shown in Figure 4.1b (θ and ϕ) to enable precise control over the polar angle and the azimuthal angle, as described in Section 2.2.1. This mechanical control is fundamental to induce and tune the extrinsic chirality of the achiral nanostructures for finding optimal fixed angles. A CMOS Camera is integrated into the setup to facilitate the precise alignment of the patterned nanohole area with the center of the incident light beam during measurements. Finally, transmitted light is collected by another objective lens and directed to a high-resolution spectrometer for spectral analysis over the range of 400–800 nm for both I_R and I_L excitations.

4.1.2 Transmission and CD Measurement

The transmission spectrum (T) for a given polarization (p) is determined directly from the spectrometer output as $T_p = I_p/I_{ref}$ under optimal oblique incidence angles (θ =10° and ϕ =30°) identified during preliminary optimization. CD is quantified based on the differential transmission between the two circular polarization states. The measured CD signal is calculated in millidegrees using equation 2.3.

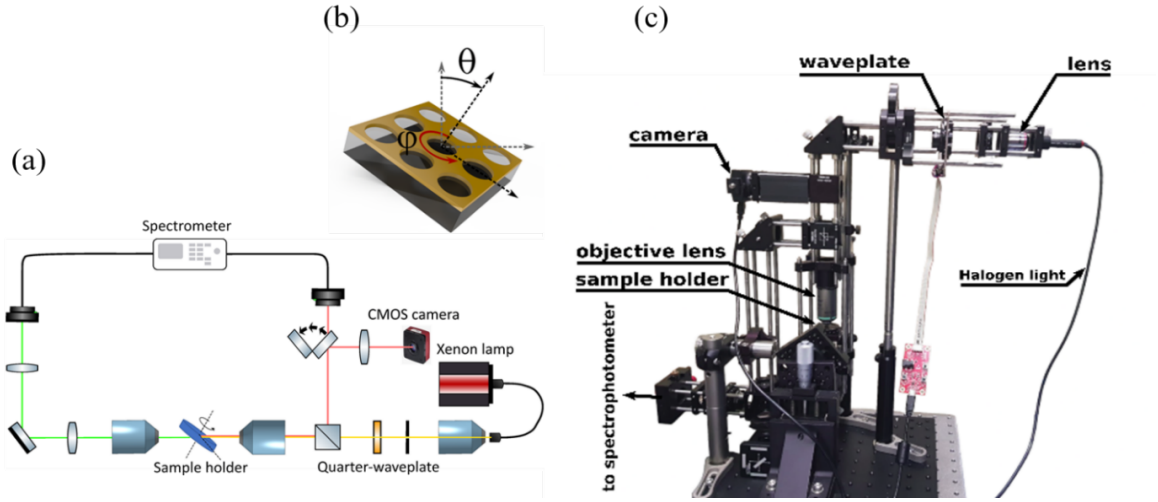

Figure 4.1 Experimental setup for angle-dependent CD measurements. (a) Schematic illustration of the optical setup for simultaneous microscopy and angle-resolved CD spectroscopy. (b) Schematic detailing the experimental geometry, specifically the definition of rotation angles θ and ϕ used for angle-resolved measurements. (c) Photograph of the actual experimental apparatus.

4.1.3 Numerical Modeling of Achiral Metasurfaces

The experimental results were validated and optimized using finite element method (FEM) calculations implemented in COMSOL Multiphysics software. This numerical approach allows for detailed analysis of the electromagnetic field distributions and the calculation of key chiroptical parameters, such as the chirality enhancement factor (χ), to identify the optimal geometric parameters for maximizing the chiral response.

The nanostructured arrays were modeled using the Electromagnetic Waves, Frequency Domain physics interface in a 3D configuration, maintaining identical geometric parameters to those used in the fabricated samples (Figure 4.2).

The numerical simulations were carried out under the following settings and modelling assumptions:

- Geometry and Boundary Conditions: The simulation domain was restricted to a single unit cell using Periodic Boundary Conditions applied to the lateral faces to simulate an infinite array.

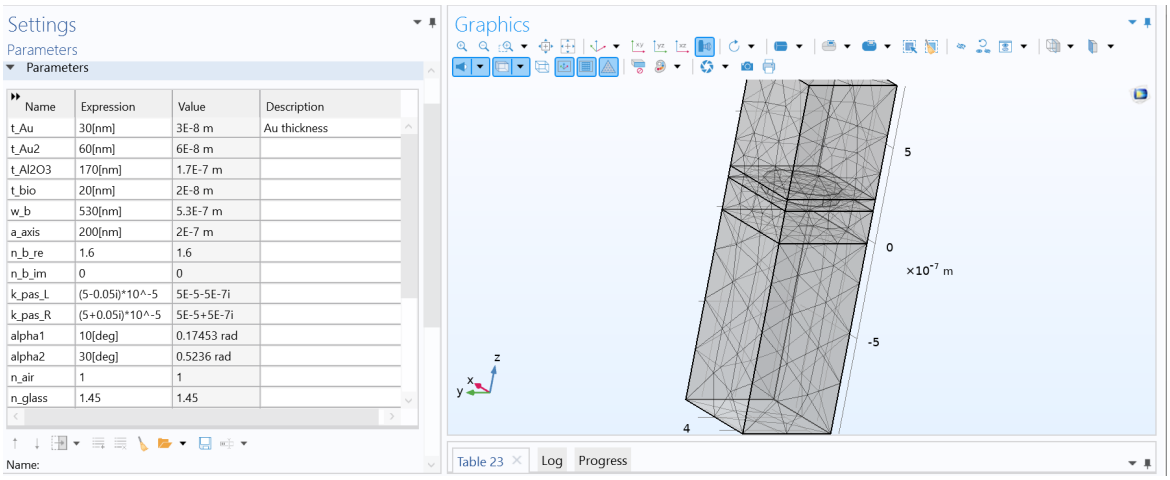

Figure 4.2 Numerical model and simulation parameters for a single gold nanohole array under oblique incidence. (Left) Screenshot of the COMSOL parameters table, listing the variables used in the simulation. The parameters alpha1 (θ) and alpha2 (ϕ) define the two angular components of the oblique incident light in the far-field excitation setup. Other parameters include the layer thicknesses (t_Au, t_Al2O3), dimensions of periodicity and radius (w_b, a_axis), refractive indices of glass and air and LPA (n_b, n_air, n_glass). (Right) The corresponding 3D meshed geometry used for the finite element simulation, illustrating the physical domain and mesh discretization of the gold nanohole structure.

- Material Properties: The complex refractive indices for the constituent materials (Gold, Al_2O_3) were determined experimentally using Spectroscopic Ellipsometry and incorporated into the model for accurate plasmonic dissipation modeling (Figure 4.3).

- Excitation and Polarization: Excitation was implemented via Ports on the top and bottom surfaces. Circularly Polarized Light fields were defined based on the Jones Matrix formalism.

- Oblique Incidence Implementation: The polar angle θ and azimuthal angle ϕ, were specified directly in the port settings under the elevation and azimuth angle of incidence input fields.

- Solution and Meshing: A parametric sweep was performed over the frequency range, and mesh refinement was applied around the nanoholes to ensure accuracy in field distribution calculations.

- Output Analysis: The simulation results primarily focused on transmission spectra and the resulting field distributions. These data were used to calculate the differential transmission (ΔT) and the volume-averaged χ factor. The key metric, the chirality

enhancement factor (χ), was calculated by defining the local optical chirality density, $C \propto \mathrm{Im}\{E \cdot H^*\}$, using custom variables for the complex electric (E) and magnetic (H^*) fields for both RCP and LCP excitations. The near-field response ($\mathrm{Im}\{E \cdot H^*\}_{near}$) was volume-averaged over the specified biolayer regions (top biolayer surface and analyte volume) using a dedicated Boundary Probe to integrate the localized field flux. This average was then normalized by the constant far-field chirality density ($\mathrm{Im}\{E \cdot H^*\}_{far}$) to yield the χ factor, which accurately predicts the CD enhancement.

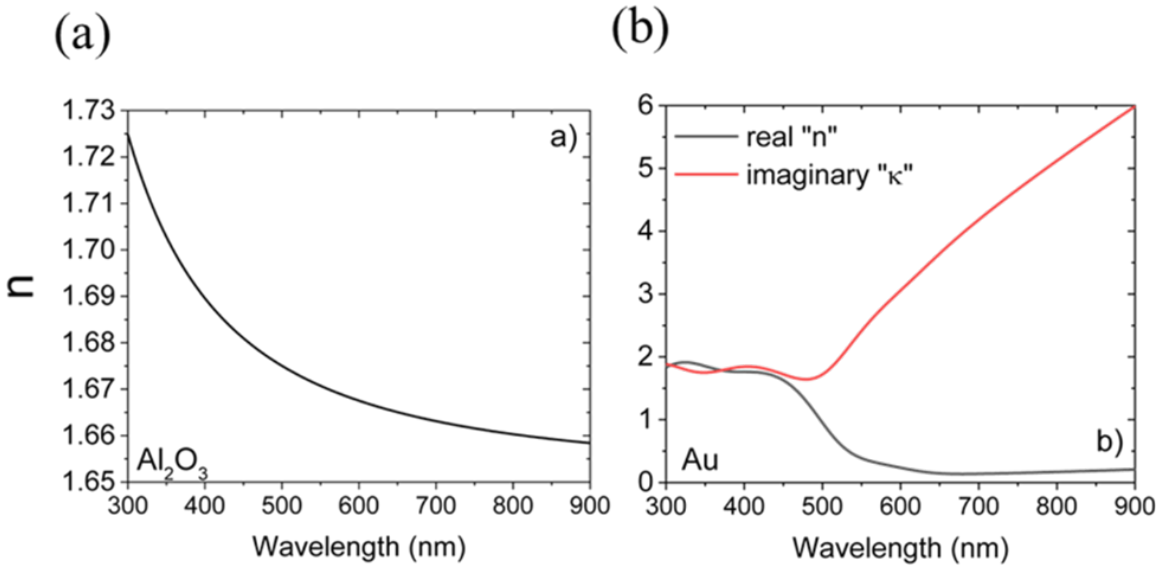

Figure 4.3 Refractive index of the Al_2O_3 and Au films used in the simulations. Reproduced from ref [32]. Copyright 2020 American Chemical Society.

4.2 Characterization of Hybrid Nanoparticle on-Mirror Cavities

The second part of this study focuses on the characterization of the hybrid NPoM cavities composed of gold, Al_2O_3, and cross stacked-dimer nanoparticle gratings. These measurements were conducted at the Leibniz Institute of Polymer Research (IPF) in Dresden, Germany, utilizing optical spectroscopy techniques to probe their chiroptical properties.

Given the complex hybrid resonant behavior of the NPoM structures, a combination of spectroscopic techniques was employed to characterize their chiroptical responses thoroughly.

Prior to CD measurements, both normal-incidence and angle-resolved transmission spectra were recorded to identify hybrid plasmonic and photonic guided-mode resonances and their coupling with diffraction modes, which can influence the CD response.

4.2.1 Optical Characterization: Circular Dichroism and Angle-Resolved- and Normal-Incidence Transmission

Circular dichroism spectra were recorded using CD spectrometer (Jasco J-810). Normal-incidence transmission and angle of incidence (AOI) measurements across the range of 300–1100 nm were performed using an Cary 5000 UV–vis–NIR spectrophotometer, enabling the identification of resonance wavelengths for both S- and P-polarized light (TE and TM modes). The photometric transmission geometry of the spectrophotometer was used to capture the optical response of each fabricated structure over the desired spectral range. An electronically controlled rotatable polarizer allowed systematic investigation of polarization-dependent effects for incident light aligned along the X- or Y-axis, particularly under angular illumination conditions. For AOI measurements, the detector arm was fixed at 180°, while the sample stage was rotated in 1° increments, providing high angular resolution to resolve the subtle spectral shifts associated with the different resonant geometries [46, 83]. By mapping the transmission as a function of the angle of incidence, dispersion plots were generated that clearly reveal the hybridization between resonant features such as the Rayleigh Anomaly (RA) and guided-mode resonance (GMR) modes. AOI-dependent measurements were performed for both S- and P-polarizations, as the emergence of these resonances governs the strength of the chiroptical response. The dispersion maps pinpoint the specific wavelength–angle combinations at which RA or other hybrid modes are excited, indicating the spectral regions with the highest electromagnetic field enhancement. Identifying these resonance conditions is essential for determining where the local chirality enhancement factor (χ) and consequently the CD amplification is maximized. AOI dispersion measurements were carried out for all four substrates (Figure 3.7(a-d)) allowing the progressive influence of each added layer on the emergence, shifting, and strengthening of resonant modes to be systematically resolved.

4.2.2 Electromagnetic Simulation Method

The angle-of-incidence (AOI) and normal-incidence transmission spectra were computed for both TE and TM polarizations using numerical simulations to allow direct comparison with experimental results.

A commercial-grade simulator based on the finite-difference time-domain (FDTD) method was used to perform the calculations (FDTD: 3D electromagnetic simulator). A plane wave source simulated the optical response, illuminating the structure at normal incidence with polarization angles of 90° and 0°, corresponding to TM- and TE-polarized light (aligned with the grating lines), respectively. Broadband illumination in the range of 400–1600 nm was used to simulate transmission data. To simulate the dispersion diagram of the structures in the classical diffraction regime, the angle of incidence was varied from $-45°$ to 45° in 1-degree increments. Perfectly matched layer boundary conditions were applied in the Z-direction, while periodic boundary conditions were used along the X and Y axes. Plasmonic particles were modeled as spheres with a 80 nm diameter, positioned on the surface with a 2 nm gap between them. The plasmonic particle gratings were represented as dimer particle lines. Frequency-domain field monitors were utilized to obtain the optical responses of the setup. To ensure optimal simulation stability, the mesh area was defined around the existing structure in all three principal directions, with a mesh step size of 2 nm. For the dielectric function of gold, data from Johnson and Christy [84] were fitted using six coefficients with a root mean square error (RMSE) of 0.22. The object-defined refractive index for L-phenylalanin was set to 1.6 [34] and the refractive index of the glass substrate was set to 1.45. For the dielectric properties of Al_2O_3, data from Palik [85] were used, while the surrounding refractive index was set to 1. The corresponding results and their interpretation will be provided in the Results and Discussion chapter.

This chapter outlined the experimental and numerical methodologies employed to characterize the chiroptical response of the fabricated plasmonic and photonic nanostructures. For the achiral nanohole and MDM arrays, a custom-built optical transmission setup was used to induce and measure extrinsic circular dichroism under controlled polarization and oblique incidence conditions. Finite element simulations in COMSOL Multiphysics software complemented the experiments, providing detailed insight into field distributions and chirality enhancement factors. The NPoM cavities were characterized using advanced spectroscopic techniques, including angle-resolved transmission and CD spectroscopy, to analyze their hybrid mode interactions. The next chapter presents and discusses the experimental and simulated results derived from these comprehensive characterization approaches.

Chapter 5

Results and discussion

In this study, the first project focused on investigating the CD response of two types of achiral metasurfaces. One was a single-layer gold nanohole array, shown in the SEM image (Figure 3.1a) and schematically in Figure 3.1b. The second was a multilayer Au/Al_2O_3/Au nanohole structure, as illustrated schematically in Figure 5.5a. Both substrates were coated with a thin layer of the chiral molecule, L-phenylalanine. In the second project, we analyzed the CD response of chiral NPoM cavities featuring dimer gratings of gold nanoparticles.

5.1 Results of Achiral Metasurfaces: Single Gold Nanohole Array

We conducted full-wave range calculations of the CD signal for three configurations: a single nanohole array, a biolayer on glass, and a gold nanohole array-supported biolayer.

Figure 5.1(a-b) shows the electric and magnetic field distributions at resonance wavelength of 725 nm for the perpendicular and tilted configurations with $\theta = 10^\circ$ (out of plane) and $\phi = 30^\circ$ (in plane). This analysis demonstrates how tilting the sample, as depicted in Figure 4.1, disrupts its structural symmetry and induces chiroptical activity.

The CD spectra of the fabricated gold nanohole structure, measured using the optical transmission setup (Figure 4.1) and calculated using equation 2.3, exhibit distinct peaks at 619 nm and 656 nm at the selected incidence angles ($\theta = 10^\circ$ and $\phi = 30^\circ$), as shown by the red curve in Figure 5.1c. The simulated CD responses at the same angular orientations, represented by the black curve in Figure 5.1c, align well with the experimental results with

corresponding valleys and peaks in both signals. The optimal thickness of the gold layer was determined numerically. The transmission colormap in Figure 5.1d reveals that a structure with an 80 nm thick gold layer exhibits a pronounced transmission peak in the 700-750 nm wavelength range, which coincides with the range of interest for CD enhancement. A second weaker transmission band can be observed around 640 nm for layer thicknesses up to 100 nm.

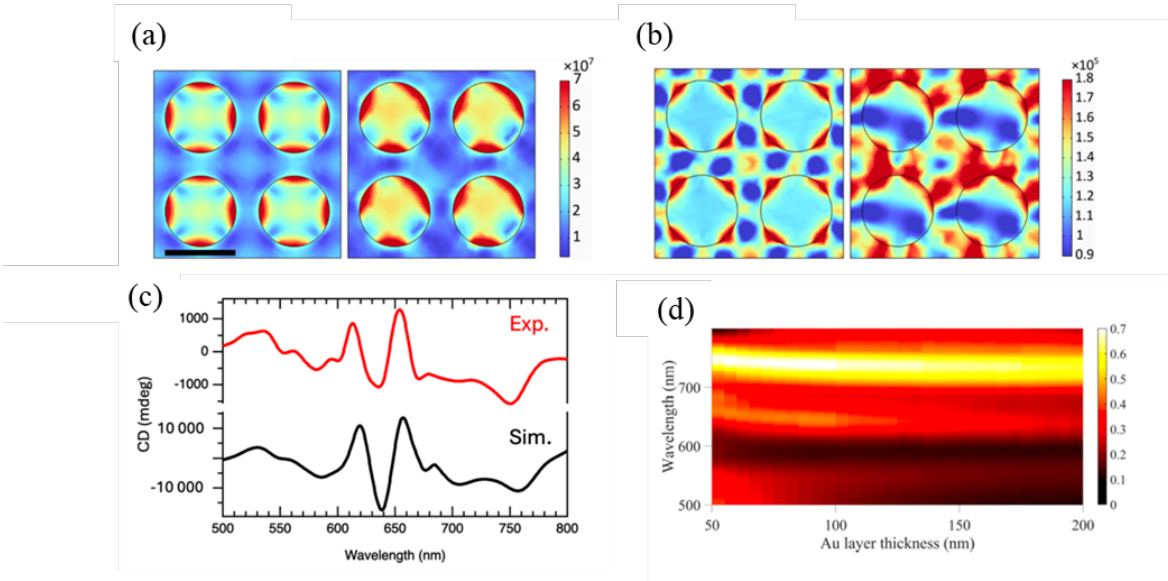

Figure 5.1 (a) Calculated electric and (b) magnetic field distributions. The left panel corresponds to perpendicular incidence ($\theta = 0°$ and $\phi = 0°$), displaying mirror-symmetric patterns at the transmission resonance wavelength of 725 nm. The right panel represents the enhanced asymmetric electric field distribution under oblique incidence ($\theta = 10°$ and $\phi = 30°$). Scale bar is 500 nm for all panels. (c) CD response of the gold nanohole array: experimental results (red curve) compared with simulation data (black curve). (d) The color map of transmission as a function of gold thickness and wavelength. The plot highlights regions of significant transmission, with a pronounced bright band observed around 80 nm of gold thickness in the 700-750 nm wavelength range. Reproduced from ref [32]. Copyright 2020 American Chemical Society.

5.1.1 Angle of Incidence Dependence of Circular Dichroism

Figure 5.2(a-f) presents a comparison of CD measurements and simulations for varying ϕ and constant θ, demonstrating very good agreement. For both simulation and experimental data, increasing the ϕ angle causes a shift in the CD response, and the magnitude starts to increase. The dashed curves represent negative ϕ angles, which exhibit similar behavior.

To investigate how the incident angle θ influences the chiroptical response, as discussed in chapter 2, we start from the general plane wave equations. Upon tilting the sample, the wavevector $\vec{k}$ is no longer purely in the z-direction but gains in-plane components k_x and k_y, which are functions of the polar angle θ and azimuthal angle ϕ. This angular dependence modifies the phase and amplitude of the transmitted field differently for RCP and LCP light. By calculating the $T \propto |\vec{E}|^2$ and substituting this into the definition of ΔT, we obtain an expression showing that ΔT depends on the incidence angle θ. This theoretical approach predicts a parabolic variation of ΔT with respect to θ, which is consistent with the simulation results in the range of 10° – 60°, as shown in Figure 5.2g.

The differential transmission ΔT between right- and left-circularly polarized light was evaluated at wavelengths of 725 nm and 640 nm, which correspond to prominent resonance features in the transmission colormap (see Figure 5.1d). This result confirms that changing θ enhances ΔT and leads to measurable CD signals, indicating the emergence of extrinsic chirality. Notably, the maximum ΔT was observed at $\theta = 30^\circ$; however, due to the limited numerical aperture (0.4) of the microscope objectives used in our setup, the experimental measurement of the CD response was constrained to tilt angles up to 10°. At larger tilt angles, the incident and transmitted beams deviate beyond the acceptance cone defined by the NA, resulting in partial light collection and reduced measurement accuracy.

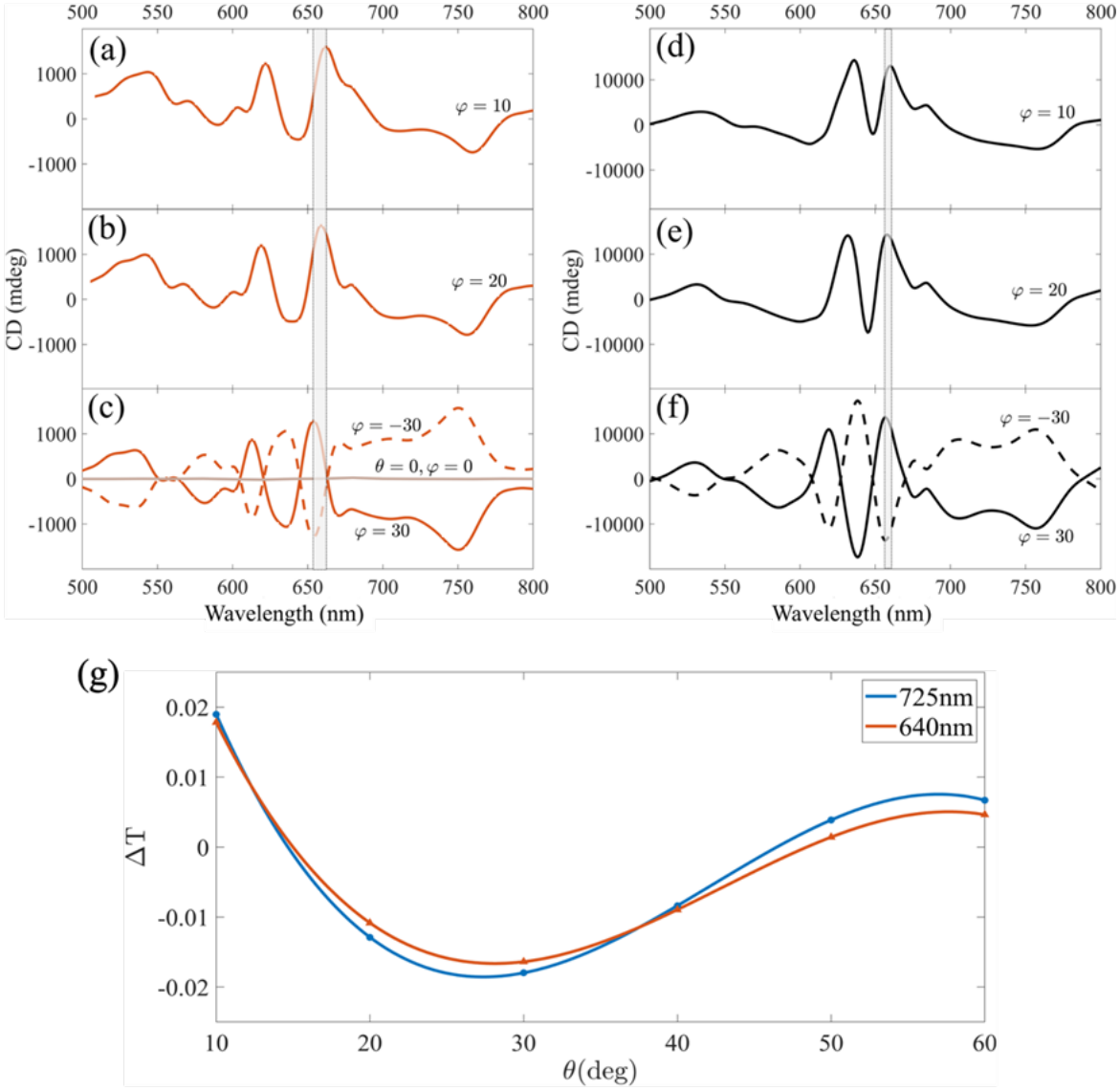

Figure 5.2 (a-g) Angular dependence of CD in gold nanohole arrays. (a–c) Experimental and (d–f) calculated angle-dependent CD signals of a gold nanohole array as a function of azimuthal angle ϕ and constant $\theta = 10°$. Dashed curves in (c) and (f) represent negative ϕ angles, and the range around 650 nm is marked to emphasize the small shift of the maximum with increasing ϕ. (g) Parametric plot showing the simulated transmission difference (ΔT) between right- and left-circularly polarized light versus incident angle of θ at resonant wavelengths of 725 nm and 640 nm in the transmission spectra. The parabolic trend observed from 10° to 60° highlights the angular dependence of chiroptical response in the tilted nanostructure. The maximum ΔT occurs at $\theta \approx 30°$, indicating an optimal tilt angle for enhancing the CD signal. Reproduced from ref [32]. Copyright 2020 American Chemical Society.

5.1.2 Simulation results of an isolated biolayer

To gain an understanding of the combined system consisting of substrate and biolayer, we first examine the properties of an isolated chiral biolayer. The L-phenylalanine layer was modeled as a chiral slab positioned in free space, characterized by a refractive index of $n_b = 1.6$ and a Pasteur parameter of $\kappa_b = (5 - 0.05i) \times 10^{-5}$ [34], which quantifies the material's chirality. The wave vectors for the RCP and LCP waves are denoted as $\pm\kappa_b$. To analytically compute the CD signal, the transmission amplitudes for RCP and LCP excitations were calculated separately under oblique incidence using chiral media in COMSOL Multiphysics. The governing equations in the software were modified according to equations 2.1 and 2.2, as discussed in Chapter 2, to accurately model the chiral response.

Figure 5.3(a,b) shows the CD of the simulated L-phenylalanine as a chiral biolayer with a thickness of 60 nm, and we have investigated the UV-CD of the biolayer coatings on silica as well as the CD response of our plasmonic sensors. Figure 5.3a depicts the CD spectra of a biolayer in the UV/Vis/NIR range, 200–800 nm for two separate coatings with L- and D-phenylalanine. CD spectra of both coatings of L- and D-phenylalanine reveal a main peak at 250 nm. Although the CD signal of the biolayer resides in the UV range, we design our sensor substrates for the Vis and NIR regions because sensing in the UV is more demanding concerning optical components.

With our strategy of using substrates that enable tunable resonances in the Vis-NIR range, we develop a sensor that effectively captures the analyte's response while ensuring straightforward compatibility with standard optical sensing. We show the full-wave simulations of both single L- and D-phenylalanine in Figure 5.3a. These calculated CD values in the visible range were then used to calculate and compare the magnitude of the enantiomeric-enhanced signals when the molecules were deposited on the sensors [32].

We employed analytical calculations based on equation 2.16 to estimate the CD of the biolayer in the Vis-NIR spectral range that we target for sensing, and compared the results with simulations [86]. Figure 5.3b shows good agreement between the two approaches.

Figure 5.4a presents the gold nanohole array on a glass substrate, with the biolayer positioned on top, and Figure 5.4b displays the induced CD enhancement measured by tilting it within the optical setup. The red curve represents the CD signal of the nanohole array, while the blue curve corresponds to the CD response of the single biolayer of L-phenylalanine on silica glass. Remarkably, a 20-fold enhancement in CD was observed when the biolayer was on the tilted nanohole arrays.

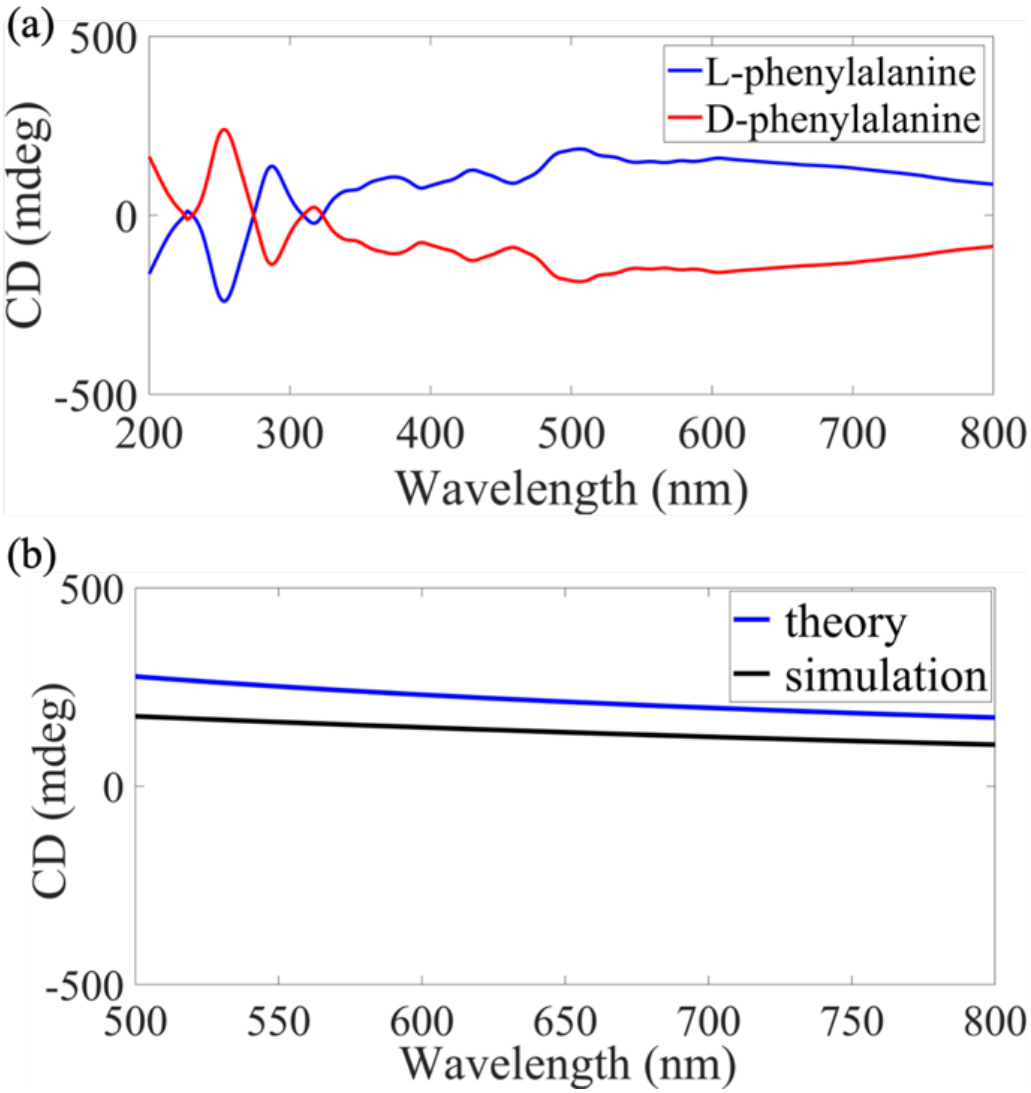

Figure 5.3 (a) Simulated CD spectra of the L-phenylalanine (blue curve) coatings and its enantiomer, D-phenylalanine (red curve), in the 200–800 nm range, revealing a main peak at 250 nm. (b) Comparison of the CD response of an L-phenylalanine from simulated (black curve) and theoretical (blue curve) studies in the visible range. Reproduced from ref [32]. Copyright 2020 American Chemical Society.

The overall CD response features a pronounced peak at 725 nm, accompanied by two valleys at approximately 715 nm and 735 nm. Moreover, COMSOL Multiphysics simulations for the nanohole array-biolayer configuration successfully reproduced these results, as shown by the black curve in Figure 5.4b. The small discrepancies in the CD signal between the experimental and simulation data result from imperfections intrinsic to experimental mea-

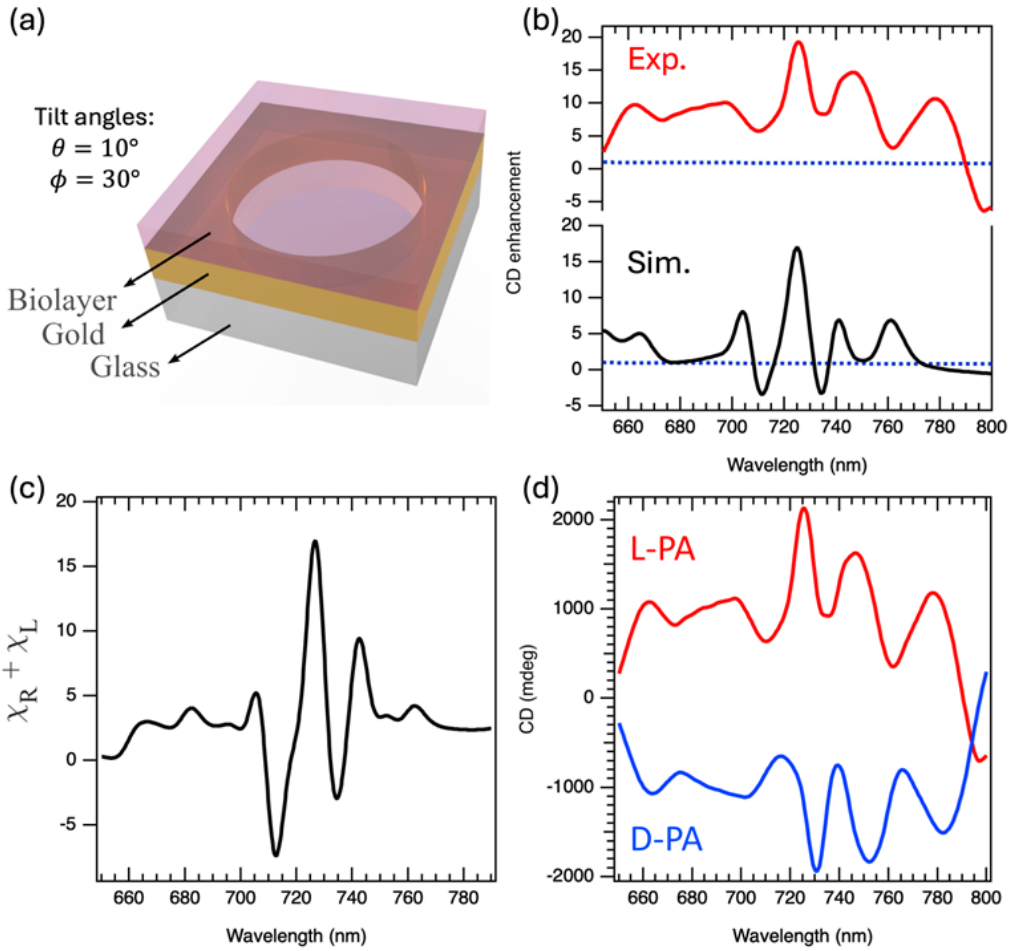

Figure 5.4 (a) Unit cell of the Au nanohole array on glass with biolayer. (b) Simulated (black curve) and experimental (red curve) CD spectra of the biolayer on gold nanohole array that exhibit valleys at 715 nm and 735 nm, with a pronounced peak at 725 nm. The blue-dashed line in both charts illustrates the normalized CD response of a single biolayer of L-phenylalanine. (c) Analytically calculated χ, displaying valleys and a peak at similar wavelengths as in the CD spectra in (b). (d) Experimental CD spectra of L-phenylalanine (L-PA-red) and D-phenylalanine (D-PA-blue). Reproduced from ref [32]. Copyright 2020 American Chemical Society.

surements, such as deviations in the precise geometry of the nanohole array, and collimation and angle of the optical light beam.

The enantiomers on top of the nanohole array show strong CD signal in the range from 700-750 nm (Figure 5.3b), distinct from the CD peak wavelength of the bare nanohole array (Figure 5.1c) but inside the transparency windows of nanohole substrate (Figure 5.1d). This happens due to the synergistic effect of the local optical chirality and the field enhancement of the nanohole array, which selectively amplify the residual CD of the enantiomers in

the visible-NIR range. The signal enhancement stems from an imbalance in the near-field distribution of the gold nanohole array, where at certain frequencies the plasmonic modes interact more effectively with the enantiomers.

As discussed in Chapter 2, to identify the parameters influencing the spectral maxima of the CD total which included single gold nanohole structure with L-phenylalanine, an analytical approach was employed in which the CD was calculated using Equation 2.14. From this analysis, the chirality enhancement factor (χ) was derived, and its value for this configuration was subsequently calculated, as described in the simulation section of Chapter 3. The spectra in Figure 5.4c show that the sum of the χ factors for RCP and LCP excitations exhibits two valleys at 715 nm and 735 nm and a peak at 725 nm, which aligns well with the CD enhancement observed in Figure 5.4b. These results indicate that the χ factor serves as a key parameter for assessing the substrate's capability to function as an effective biosensor. Figure 5.4b shows that the tilted nanohole array substrate provides very high CD enhancement of a factor of 20 at the resonance (725 nm) compared to a biolayer on bare glass (blue-dashed line). The CD spectra for both enantiomers, L- and D-phenylalanine, are shown in Figure 5.4d. Assuming that the two biolayers differ only in their CD signatures, which corresponds to opposite signs of the imaginary part of the Pasteur parameter, and reversing the handedness of the biolayer should result in a sign reversal of the CD signal, as clearly evident in the spectra [32].

5.2 Results for Achiral Metasurfaces: Optimized Metal-Dielectric-Metal cavity

The substrate-mediated chiroptical enhancement can be further increased by combining the plasmonic nanohole array with an optical cavity. We designed and fabricated a metasurface MDM structure [87, 88], in which the Au film with the nanohole array is the top metal layer, as illustrated in Figure 5.5a. This engineered non-chiral planar metasurface supports strong near-field electromagnetic effects, enabling significant amplification of optical chirality and CD [62]. To find the optimal thickness of the dielectric layer, we simulated the transmission spectra of the MDM nanohole array structure over a range of Al_2O_3 thicknesses (Figure 5.5b). A thickness of 170 nm was selected, as it supports optical resonances in approximately the same spectral region as the single-layer gold nanohole substrate to illustrate the effect of the nanohole array within the MDM structure. We expect synergies of the cavity and

plasmonic enhancement effects, and this geometry allows for a straightforward comparison in enhancement efficiency with the nanohole array. Thus, the MDM structure consists of a 170 nm-thick Al_2O_3 layer sandwiched between a 30 nm bottom gold film and a 60 nm top gold film patterned with nanoholes [32].

For further optimization, we evaluated the factor χ with respect to the nanohole radii ranging from 120 nm to 250 nm (Figure 5.5c). The results revealed a maximum χ value at a radius of 200 nm. The enhancement of the χ value is attributed to the near-field enhancement induced by the MDM-nanohole array cavity, in particular, with respect to the magnetic field at resonance. Simulation of the current density distribution, shown in Figure 5.5d (XY plane cross section of the nanohole array unit cell), demonstrates the formation of closed-loop displacement patterns within the MDM layers, as discussed in Chapter 2. These loops generate localized magnetic field. In contrast, the single-layer gold nanohole structure does not support such circulating displacement currents, indicating that its chiroptical response arises primarily from comparatively weaker electric-dipole interactions rather than the magnetic-dipole modes supported in the MDM-nanohole array architecture [32].

As shown in Figure 5.5(e-f), the electric and magnetic field distributions in the MDM-nanohole array structure are significantly stronger than those observed in the single-layer gold nanohole array [64].

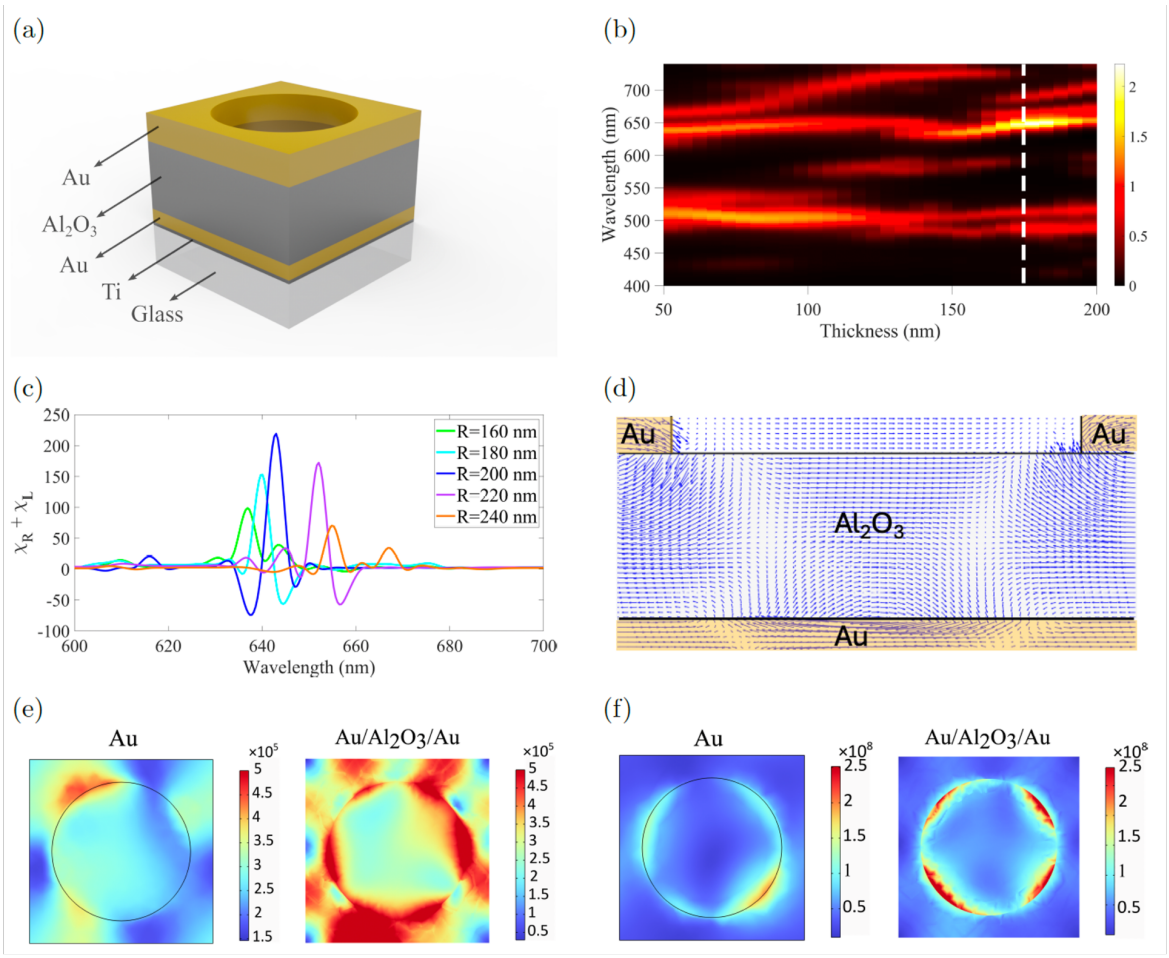

Figure 5.5 (a) Unit cell of the $Au/Al_2O_3/Au$ nanohole array structure. (b) Colormap of simulated transmission as a function of Al_2O_3 thickness and wavelength. The color scale was adjusted to [0-2] to enhance the contrast of the narrow transmission peaks associated with the MDM cavity. (c) Calculated average optical chirality enhancement factor (χ) for varying nanohole radii. The maximum χ occurs at a radius of 200 nm. (d) Snapshot of the displacement current distribution in the xy-plane for the $Au/Al_2O_3/Au$ nanohole array structure at $\lambda = 643$ nm. (e) Magnetic and (f) electric field distributions at transmission resonance $\lambda = 725$ nm for a single-layer gold nanohole array (left) and at transmission resonance $\lambda = 643$ nm for the $Au/Al_2O_3/Au$ nanohole array structure (right), under oblique illumination ($\theta = 10°$, $\phi = 30°$). Magnetic and electric fields are in A/m and V/m, respectively. Reproduced from ref [32]. Copyright 2020 American Chemical Society.

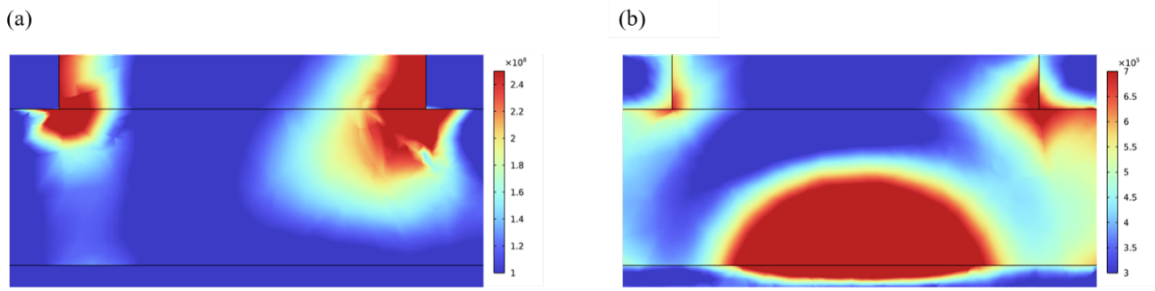

Figure 5.6 E-field and H-field Distributions for the Au/Al_2O_3/Au nanohole array structure. Cross-sectional (ZY plane) plots illustrating the calculated (a) electric field and (a) magnetic field at the resonant wavelength of 643 nm.

Figure 5.6 shows the cross-sectional field distributions of the Au/Al_2O_3/Au nanohole array at its resonant wavelength. In Figure 5.6a, the electric field is primarily concentrated at the sharp edges of the top gold layer surrounding the nanohole opening, forming intense hotspots that are characteristic of a plasmonic resonance. In Figure 5.6b, the magnetic field is strongly confined and enhanced both around the nanohole edges and within the central Au/Al_2O_3/Au dielectric gap. This pronounced H-field confinement indicates the presence of a magnetic plasmon resonance, or MDM cavity mode, arising from circulating currents along the metal–dielectric interfaces.

To experimentally validate the sensing capability of the MDM-nanohole array substrate, a 60 nm of L-phenylalanine biolayer was deposited on both glass and the MDM-nanohole array substrates. CD measurements in Figure 5.7a show a ∼50-fold enhancement in CD signal when the biolayer was placed on the MDM-nanohole array substrate, compared to glass. Under similar conditions, the single-layer gold nanohole substrate exhibited a 20-fold CD enhancement. Simulations further predicted up to 80-fold CD amplification for the MDM-nanohole array configuration as shown in Figure 5.7b (red curve), underscoring its superior sensitivity to chiral interactions. As shown in Figure 5.7b (black curve), the optimized MDM-nanohole array structure exhibited a χ factor that shows similar behavior to the CD spectra, and which is larger than that of the single-layer gold nanohole array approximately with a factor of 10. Therefore, our simulations indicate that further enhancement can be possible, which renders this system as a highly promising candidate for ultrasensitive, enantioselective biosensing applications.

The transmission and reflection spectra of the MDM-nanohole array metasurface (Figure 5.7c) reveal a prominent resonance at $\lambda = 643$ nm. This feature aligns with peaks observed in both χ factor and CD response (Figure 5.7b). Based on its asymmetric profile, this

resonance is attributed to a Fano resonance, which could arise from the interference between a broad surface lattice resonance (SLR) of the periodic gold nanohole array [74] and a discrete Fabry-Pérot cavity mode within MDM nanohole architecture. This mutual coupling generates the characteristic Fano interference observed in the transmission spectra [89, 90]. The Fano resonance is well known to generate enhanced near-field intensities and strong local electromagnetic confinement beyond what is achievable by isolated resonances, thereby amplifying optical effects at the nanoscale [89, 90]. The simultaneous spatial concentration and amplification of both electric and magnetic field components markedly increase the local optical chirality density, which directly influences the differential transmission of right- and left-handed circularly polarized light through chiral molecules adsorbed on the surface [60, 91]. To quantify the resonance's asymmetry and enhancement, we fitted the measured transmission spectra shown in Figure 5.7d with the standard Fano line shape function [92] and obtained an asymmetry factor $q \approx 3.3$. In the Fano model, the asymmetry parameter q quantifies the relative contribution of the discrete resonant mode to the spectrally broad background channel and therefore determines how strongly asymmetric the resulting line shape is. Values of q close to unity correspond to strongly asymmetric peak–dip profiles, whereas large q (typically $\gtrsim$ 5–10) approach a symmetric Lorentzian response. Accordingly, the fitted value $q \approx 3.3$ indicates a pronounced but moderate asymmetry, consistent with Fano interference between a discrete resonance and a broader spectral continuum [93].

We investigated the sensitivity of our MDM-nanohole array devices with CD measurements on L-PA films with different thicknesses, ranging from 20 – 140 nm (Figure 5.8a). To quantify the sensitivity we consider an operational spectral bandwidth of 680-700 nm, and normalize the integrated signal as $CD_{NORM}(t) = (CD_{Film}(t) - CD_{Substrate})/CD_{Substrate}$ in this spectral range. The profile of $CD_{NORM}(t)$ resembles roughly a sigmoidal shape (Figure 5.8b), and we rationalize the saturation of the CD signal for large film thicknesses (exceeding 100 nm) with the increasing distance of the analyte molecules from the metasurface that reduces the efficiency of the signal enhancement. Based on this data set we can establish an upper detection limit of around 20 nm film L-PA film thickness that corresponds to 108 molecules in a spot size of 1 μm^2 [32].

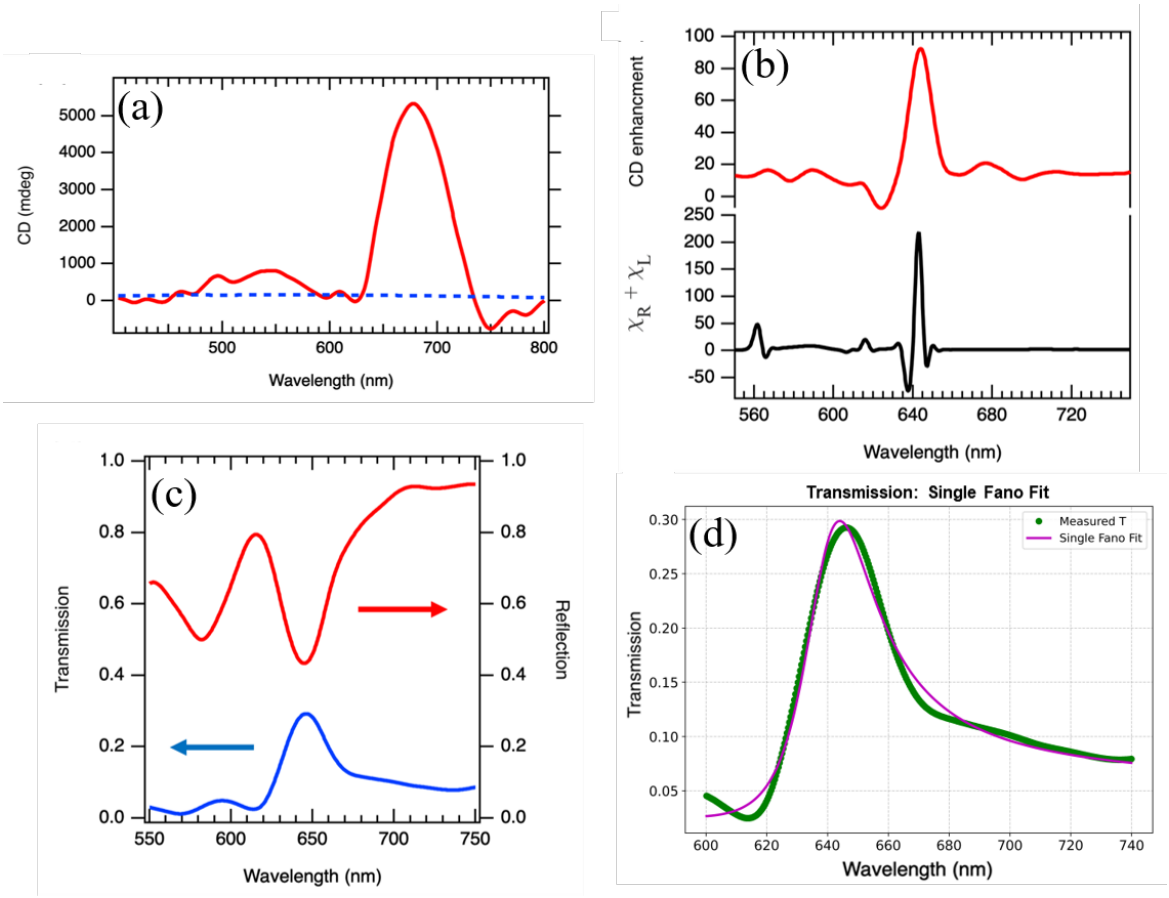

Figure 5.7 (a) Experimental CD spectra of L-phenylalanine deposited on the $Au/Al_2O_3/Au$ nanohole array substrate (red curve) and on glass (blue-dashed line). A $\sim$ 50-fold enhancement in CD signal is observed for the $Au/Al_2O_3/Au$ nanohole array configuration. (b) Simulated CD enhancement (red curve) for the $Au/Al_2O_3/Au$ nanohole array structure, predicting up to an 80-fold amplification of the CD signal for L-phenylalanine. Averaged optical chirality enhancement factor χ (black curve) for the $Au/Al_2O_3/Au$ nanohole array structure at a nanohole radius of 200 nm. (c) Simulated transmission and reflection spectra of the $Au/Al_2O_3/Au$ nanohole array structure, showing a Fano resonance centered at 643 nm. Reproduced from ref [32]. Copyright 2020 American Chemical Society.

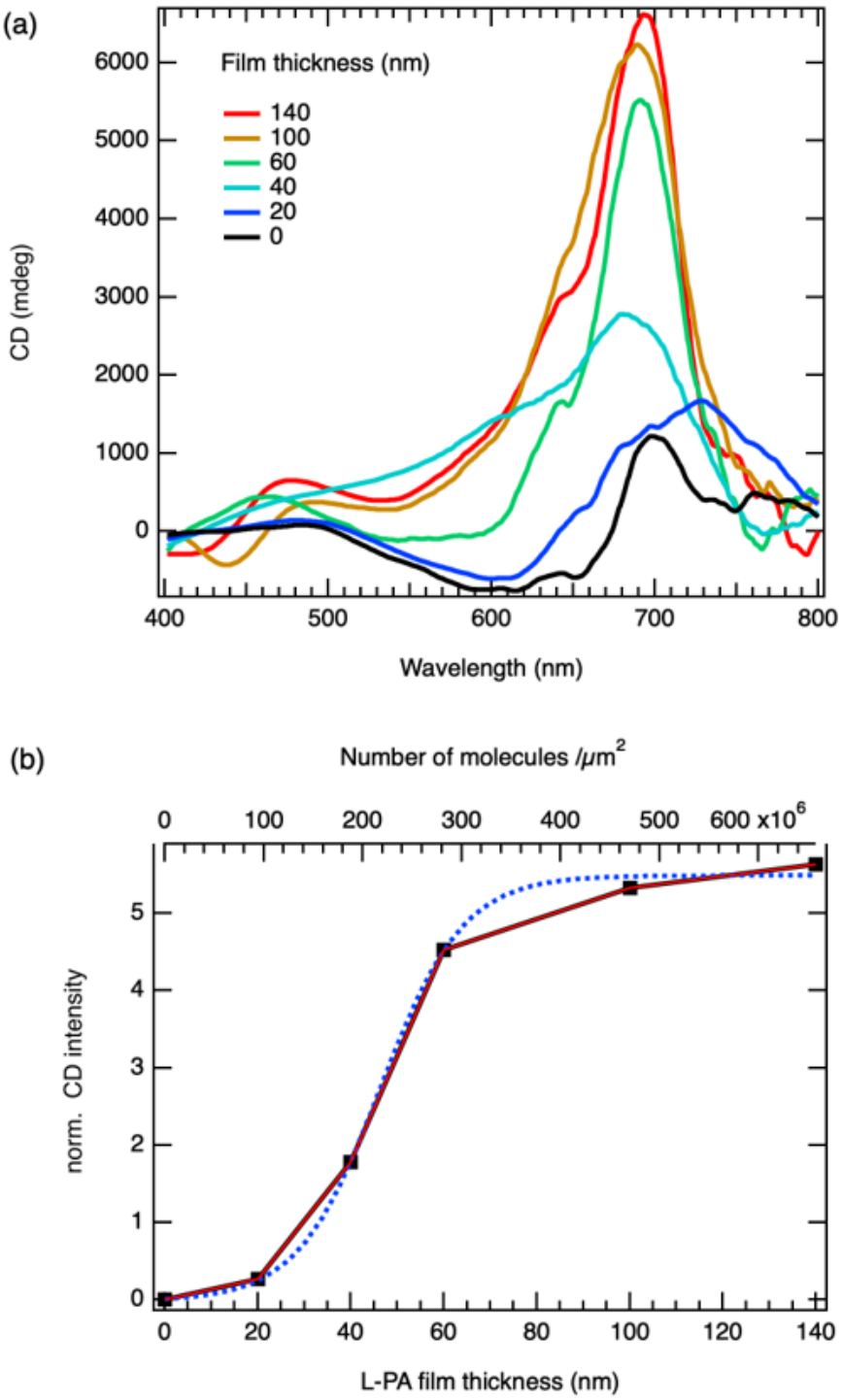

Figure 5.8 (a) CD spectra for L-phenylalanine (L-PA) films with different thicknesses in the range from 20-140 nm. (b) CD enhancement versus film thickness, and number of molecules in a 1 μm spot region. The dashed blue line shows a sigmoidal fit to the data. Reproduced from ref [32]. Copyright 2020 American Chemical Society.

In conclusion, regarding the tilted achiral samples, we presented a comprehensive investigation on enhancing chiroptical responses using achiral nanostructures under oblique illumination. By introducing extrinsic chirality through tilted gold nanohole arrays, we achieved significant amplification of CD signals approximately by a factor of 20 in the presence of L-phenylalanine as a chiral biolayer compared to when it is placed on glass, which we obtained by both experimental measurements and numerical simulations. We demonstrated that the χ factor is a key parameter in understanding and optimizing substrate-mediated chiroptical amplification. Building on these insights, we developed a multilayer $Au/Al_2O_3/Au$ nanohole structure, which exhibited a superior loop-formed current density distribution that boosts enhanced near-field interactions. The optimized MDM-nanohole array platform achieved a nearly 10-fold increase in the χ factor and a factor of 2.5 increase in CD signal compared to single-layer gold nanohole arrays. This MDM-nanohole array substrate reached a 50-fold enhancement for L-phenylalanine, highlighting its potential for ultrasensitive, enantioselective biosensing applications.

Our findings establish extrinsic chirality engineering and χ factor optimization as powerful strategies for advancing plasmonic chiral sensors. This approach paves the way for the development of next-generation nanophotonic platforms with high sensitivity and selectivity for enantiomer detection.

5.3 Results for Chiral Metasurfaces: NPoM Cavities

In this section we investigate the NPoM cavity to explore the benefits of hybrid plasmonic-photonic mode coupling in colloidally assembled gratings. To obtain a solid base for this investigation we begin with a systematic layer-by-layer isolation strategy.

5.3.1 AOI and Transmission Analysis of NPoM Cavities with Single-Layer Nanoparticle Dimer Gratings

We recorded Angle of Incidence (AOI) dispersion maps and normal-incidence transmission spectra for all structures with single layer of NP dimer grating shown in Figure 3.7(a-d). This step was crucial for identifying the specific hybrid mode interactions (SPP, GMR, and RA), shown schematically in the Figure 2.1, that strongly influence local chirality and dictate the spectral positions of maximum CD enhancement.

5.3.1.1 Structure 1: Glass/NP Dimer Grating (Figures 5.9, 5.10)

To interpret the optical response of Structure 1, we begin by summarizing the relevant grating–plasmon modes and their polarization dependence. The one-dimensional nanoparticle dimer grating supports two Rayleigh anomalies. Rayleigh anomaly conditions of the grating at the normal incidence ($\theta_{inc} = 0$) and for the first order ($m = \pm 1$), satisfy $\lambda_{RA}(0) = nP$, which yields $\lambda_{RAc}(0) = n_{air}P \approx 1.0 \times 620$ nm = 620 nm for the cover, and $\lambda_{RAs}(0) = n_{glass}P \approx 1.45 \times 620$ nm = 899 nm for the substrate. As seen in the AOI maps, they follow their angle-dependent grating dispersion as θ changes [94].

The dimer chains additionally sustain two polarization-dependent plasmonic modes as explained in the section 2.5.2.3. A long-axis (longitudinal-like) mode that is excited when the electric field is oriented along the chain (LSPR(L)), and a short-axis (transverse-like) mode driven when the field is polarized across the dimer gap (LSPR(T)). These chain modes couple to the diffracted orders when their spectral positions overlap [95].

As shown in the simulated normal-incidence transmission spectra in Figure 5.9a, the TE transmission spectrum of Structure 1 shows two distinct spectral features near the Rayleigh anomalies, located at $\lambda \approx 588$ nm and $\lambda \approx 975$ nm. The dominant response arises at $\lambda \approx 975$ nm, where the substrate-side anomaly RAs coincides with the long-axis plasmonic mode. At this wavelength, the simulated electric-field map (Figure 5.10a) shows the characteristic pattern of the longitudinal mode hybridized with RAs, where the electric field is distributed more around the particle perimeters and the energy leakage into the substrate corresponds to the RAs diffraction channel. This behavior directly reflects the fact that super-radiant chain modes redistribute their fields around the particle and couple efficiently to radiative diffraction orders (LSPR(L)–RAs) [96, 97, 95]. The weaker TE feature near $\lambda \approx 588$ nm results from the spectral overlap between the long-axis plasmon and RAc. The longitudinal LSPR involves charge oscillation along the long axis of the nanoparticle dimer chain, yielding strong electromagnetic coupling between particles, a large effective dipole moment, and consequently a redshift toward longer wavelengths [98, 99, 95]. Thus, the $\lambda \approx 588$ nm at the short wavelength which coupled with RAc is weaker than $\lambda \approx 975$ nm. In experimental TE transmission spectrum in Figure 5.9e the dominant resonance associated with the RAs–longitudinal hybrid appears at $\lambda \approx 914$ nm, accompanied by a weaker feature near $\lambda \approx 548$ nm that corresponds to the RAc–longitudinal interaction, both of which are in excellent agreement with the simulated spectra.

As shown in the Figure 5.9b for simulated TM polarization in the 0th-order (normal-incidence) transmission, the strong resonance associated with LSPR(T)-RAc at $\lambda \approx 581$ nm, while another weaker TM feature appears near $\lambda \approx 903$ nm, where LSPR(T) couples with RAs. The strong resonance at $\lambda \approx 581$ nm arises because LSPR(T) is naturally resonant at short wavelengths. LSPR(T) involves charge oscillation across the short axis of the dimer, directly across the nanogap, producing a smaller radiating dipole and a resonance shifted toward shorter wavelengths than LSPR(L) for the same geometry. This trend is confirmed experimentally (Figure 5.9f): the strong RAc–transverse hybrid appears at $\lambda \approx 541$ nm, while a much weaker feature near $\lambda \approx 907$ nm corresponds to the RAs–transverse interaction, in agreement with the simulated TM spectra.

In TM polarization because the incident field has a strong E_x component directed across the gap that in the XZ electric-field map, yields a localized $|E|$ hotspot in the nanogap [100]. The associated magnetic field H_y wraps tightly around this $E_x - E_z$ bridge across the gap and forms compact H-field lobes just above and below the gap region, as shown in Figure 5.10b. This magnetic-field pattern follows directly from Maxwell's curl equation,$\nabla \times E = -\mu_0 \frac{\partial H}{\partial t}$ which requires that strongly varying electric fields generate circulating magnetic fields. In the transverse plasmon, the electric field changes extremely rapidly across the nanogap (large $\partial E/\partial x$ and $\partial E/\partial z$), forcing the magnetic field into tightly confined circulation loops. Because the field is concentrated over a very small gap width, the magnetic energy density is extremely localized, producing the compact H_y lobes observed in the field maps [101].

The simulated H-field map (Figure 5.10b) shows the characteristic signature of a strong transverse-RAc hybrid: an extremely bright H-field nanogap hotspot, together with RA beams region at the expected diffraction angles, produced coupling of LSPR(T)-RAc at $\lambda \approx 581$ nm.

For this structure, the AOI dispersion map (Figure 5.9c) for TE polarization shows the angle-dependent RAs diffraction line intersecting a broad longitudinal LSPR(L) band near $\lambda \approx 975$ nm, and their crossing produces the strong hybrid resonance observed. In the AOI map for TM (Figure 5.9d), the RAc branch crosses the strong LSPR(T) band near $\lambda \approx 581$ nm, forming the corresponding TM resonance seen in the normal-incidence spectrum. The experimental AOI map in Figure 5.9(g and h) for both TE and TM exhibit the same dispersion characteristics, confirming the presence of the same hybrid mode.

Overall, Structure 1 exhibits strong RA–LSPR hybridization in TM at short wavelengths and strong hybridization in TE at long wavelengths due to the strong LSPR(L), consistent with the distinct physical nature of the transverse and longitudinal plasmon modes. These

conclusions are supported by the normal transmission spectra, the field distributions, and the AOI measurements. The experimental normal-incidence transmission spectra confirm this behavior, showing modulations at nearly the same wavelengths for both TE and TM polarizations.

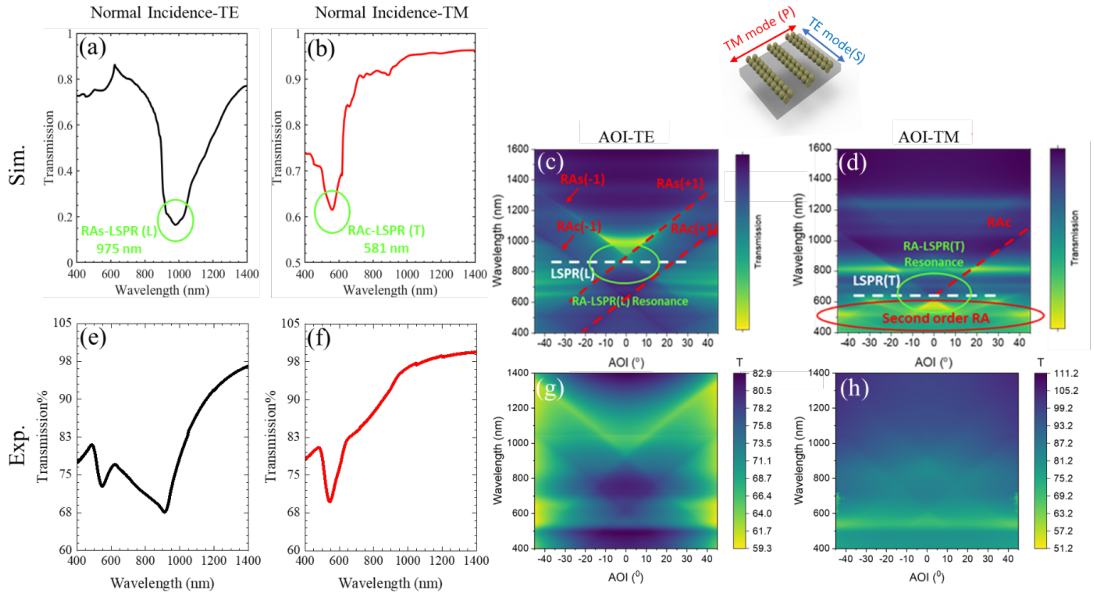

Figure 5.9 Simulated and experimental optical response of the glass/NP dimer chain structure. Panels (a) and (b) show the simulated normal-incidence transmission spectra for TE (black) and TM (red) polarizations, where the TE spectrum exhibits a pronounced RAs–LSPR(L) hybrid resonance near 975 nm and the TM spectrum reveals the RAc–LSPR(T) coupling around 581 nm. In the corresponding experimental spectra, panels (e) and (f), the main hybrid resonances appear near 914 nm for TE and 541 nm for TM, confirming the polarization-dependent RA–LSPR coupling. Panels (c) and (g) present the simulated and experimental AOI-dispersion maps for TE polarization, highlighting the angle-dependent RA branches and their hybridization with the longitudinal LSPR(L) band, while panels (d) and (h) show the corresponding TM maps, where the RAc–LSPR(T) hybrid and an additional second-order Rayleigh anomaly are visible.

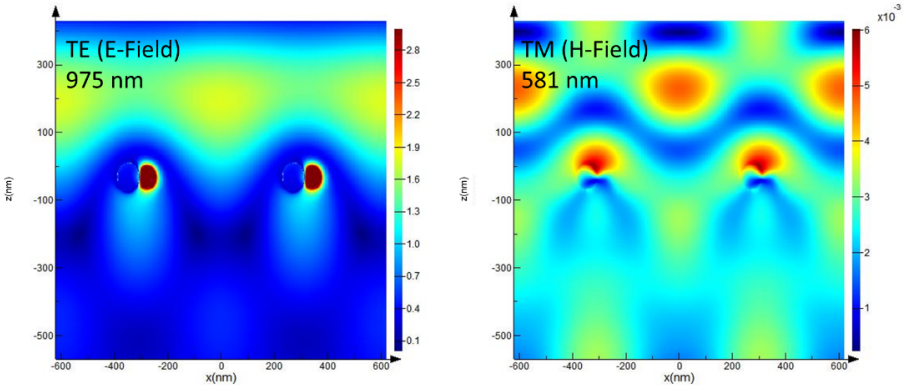

Figure 5.10 (a) TE-polarized electric field at $\lambda \approx 975$ nm, showing the field pattern of the longitudinal chain mode (LSPR(L)) hybridized with the RAs. (b) TM-polarized magnetic field at $\lambda \approx 581$ nm, corresponding to the transverse chain mode (LSPR(T)) coupled to the RAc.

5.3.1.2 Structure 2: Glass/Au Film/NP Dimer Grating (Figures 5.11, 5.12, 5.13)

When the 30 nm gold film is introduced beneath the nanodimers, SPPs become possible at the metal–dielectric interfaces, but they exist only for TM polarization. Surface plasmon polaritons also contribute strongly in TM because an SPP requires an electric-field component normal to the metal surface to drive charge oscillations along the metal-dielectric interface. TE polarization lacks this normal electric-field component, so it cannot excite SPPs. TM polarization, however, provides both E_x and E_z, enabling strong interface charge build-up and tightly bound surface waves; therefore, SPP-associated resonances appear exclusively and strongly in TM which we explain this resonance at the following of TM polarization section [102].

The presence of the continuous gold layer, as observed in both the TE and TM normal-incidence transmission spectra and AOI dispersion maps (Figure 5.11), introduces a characteristic interband-transition feature around ∼508 nm. Thin Au films with filled 5d bands exhibit a pronounced spectral response when photons have sufficient energy to excite electrons from the 5d band into the 6sp conduction band. Just below this interband threshold the absorption is relatively low and a transmission peak may appear; as the photon energy increases further, the absorption rises and the transmission correspondingly decreases [103]. In the TE and TM spectra of this structure, the broad feature centered near $\lambda \approx$508 nm is therefore attributed to the Au interband response, which is polarization-insensitive and independent of the grating period, as also reflected in the AOI maps for both polarizations (Figure 5.11(c,d)). The

electric-field map corresponding to the TE interband feature at 508 nm is presented in Figure 5.12a.

In addition, no SPP is observed in TE, and the TE spectrum of Figure 5.11a is dominated by a single broad resonance associated with the LSPR(L) around $\lambda \approx 1047$ nm. Its close AOI in Figure 5.11c confirms the localized nature of the mode, and its absence in the TM spectrum at the same wavelength range further supports its assignment as a purely longitudinal chain mode that couples primarily to the TE field oriented along the chain. The electric-field distribution (Figure 5.12b) shows strong concentration around each nanoparticle with negligible extension into the substrate or cover beyond the evanescent near field.

In TM polarization (Figure 5.11b), both the LSPR(T) and SPP modes are supported, and their coupling to the Rayleigh anomalies produces a richer set of resonances. The LSPR(T) couples strongly to the RAc at $\sim$643 nm. The corresponding H-field map (Figure 5.13a) shows an intense nanogap hotspot, combined with distinct ± 1 diffractive beams, revealing an RAc–LSPR(T) hybrid.

More importantly, in this structure, the TM AOI map (Figure 5.11b) reveals angle-dependent dispersions lying slightly below the substrate light line at longer wavelengths. These branches correspond to hybrid modes formed by the coupling of Au/glass interface SPPs with the Rayleigh anomaly, giving rise to a resonance at $\lambda \approx 718$ nm at normal incidence, consistent with the feature observed in the TM transmission spectrum. Their identification as SPPs follows directly from two elements: their presence exclusively in TM and their interface-localized fields. As these SPP dispersions approach RAc, the H-field maps (Figure 5.13b) show the coexistence of a confined interface field with strong ± 1 diffraction beams, indicating RAc–SPP hybridization. Another RA–SPP interaction apears near $\sim$1000 nm in AOI map (Figure 5.11d); however, its strongest coupling occurs at oblique angles, so the normal-incidence transmission samples only the weak tail of the resonance. This angle-selective behavior is characteristic of high-Q RA–SPP hybrids: the SPP is a tightly bound, low-loss surface wave, and only at the specific angles where its dispersion intersects the Rayleigh condition does perfect momentum matching occur. At these angular crossing points, radiative leakage is minimized and the hybrid becomes high-Q. Away from this phase-matching condition the coupling collapses, so the resonance disappears at normal incidence [104, 105]. Both of these angle-dependent SPP-RA diffraction branches are observed in the AOI map Figure 5.11d.

Experimentally, the normal-incidence TE and TM transmission spectra (Figure 5.11(e,f)) exhibit resonances near $\sim$500 nm that match the simulated interband response. Although

some features in the experimental spectra are less pronounced, likely due to fabrication imperfections and slight deviations from the ideal simulated geometry, the TM experimental AOI map (Figure 5.11h) shows an angle-dependent dispersion line that likely corresponds to the RAc–SPP hybrid, appearing at the same position as in simulation. Additionally, in the TE experimental AOI map (Figure 5.11g), around ∼1100 nm an angle-independent line is observed, attributed to the LSPR, in agreement with the simulated response.

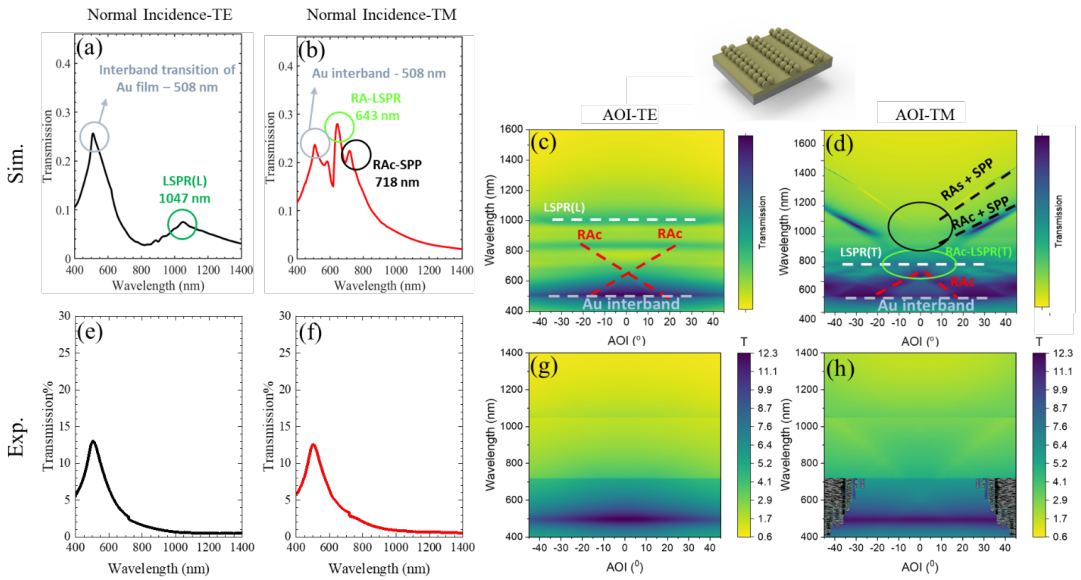

Figure 5.11 Simulated and experimental optical response of the glass/Au/NP-chain structure. Panels (a) and (b) show the simulated normal-incidence transmission spectra for TE (black) and TM (red) polarizations, where the TE spectrum exhibits a longitudinal LSPR(L) resonance near 1047 nm and the spectral onset of the Au interband transition around 508 nm, while the TM spectrum displays an RAc–SPP hybrid near 718 nm together with the RAc–LSPR(T) feature around 643 nm. In the corresponding experimental spectra, panels (e) and (f), the dominant peak near 506 nm reflects the Au interband-related mode. Panels (c) and (g) present the simulated and experimental AOI-dispersion maps for TE polarization, highlighting the broad LSPR(L) band around 1000 nm and the Au interband around 500 nm. Panels (d) and (h) show the TM AOI maps. The dispersive branches could be the same (RAc–LSPR(T)) in simulation.

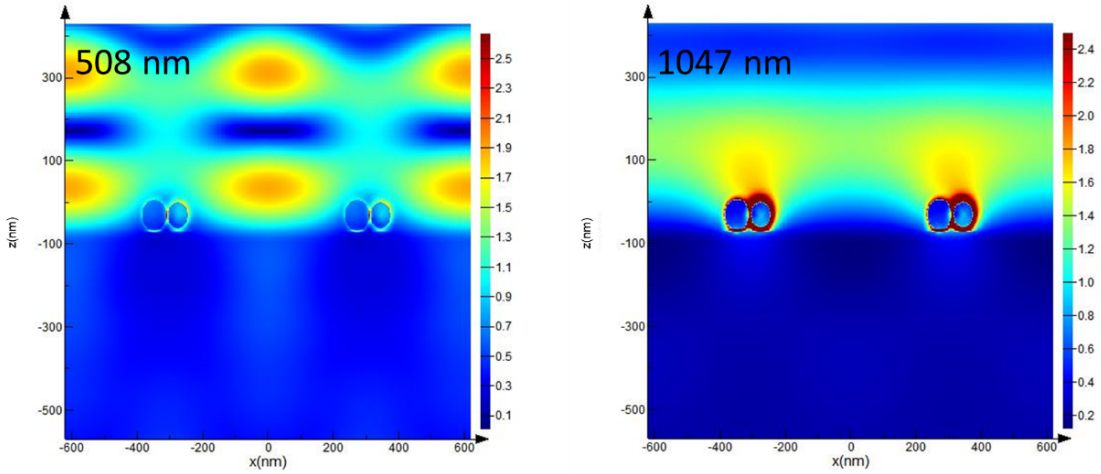

Figure 5.12 Electric-field distributions (XZ plane) for Structure 2 under TE polarization at the wavelengths of the two TE resonances. (a) at $\lambda \approx$508 nm, the field pattern reflects the Au interband response. (b) at $\lambda \approx$ 1047 nm, the field distribution is consistent with the longitudinal chain mode LSPR(L).

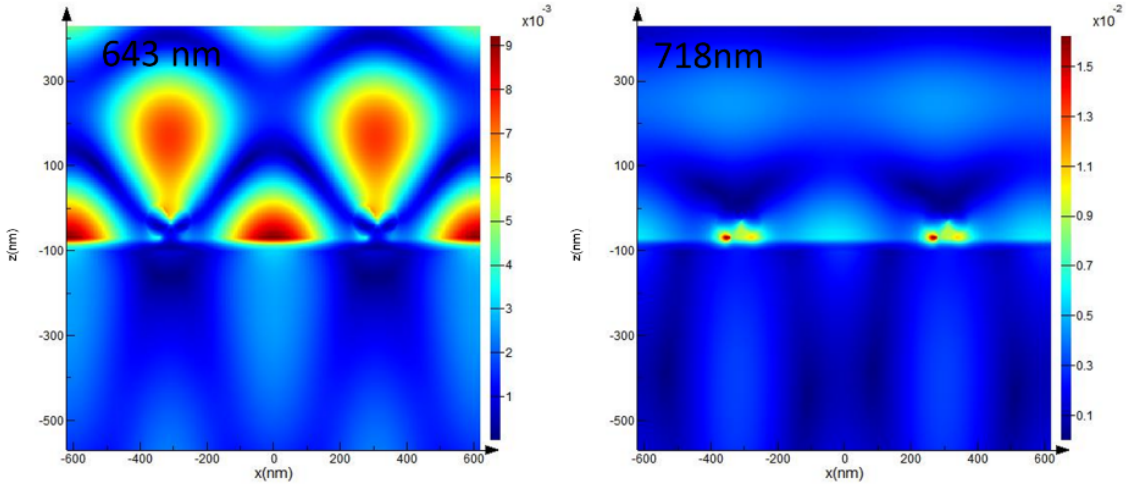

Figure 5.13 Magnetic-field distributions (XZ plane) for Structure 2 under TM polarization at the wavelengths of the two TM resonances.(a) at the $\lambda \approx$ 643 nm, this resonance corresponds to an RAc–LSPR(T) hybrid. The field pattern exhibits the symmetry of the transverse chain mode together with upward $\pm$1 diffracted orders associated with the RAc. (b) at $\lambda \approx$ 718 nm, this resonance corresponds to an SPP–RAs hybrid. The field is concentrated along the Au–glass interface, accompanied by diffraction signatures of the RAs.

5.3.1.3 Structure 3: Glass/Au/Al_2O_3/NP Dimer Grating (Figures 5.14, 5.15, 5.16)

Introducing the high–refractive-index Al_2O_3 layer fundamentally changes the optical response because the slab provides sufficient refractive-index contrast to confine light laterally, allowing the formation of waveguide modes that do not exist in the previous structures. Adding the 170 nm Al_2O_3 slab enables guided-mode resonances (GMRs) (Figure 2.1). These resonances arise when incident light couples, via the grating, to slab-guided modes of the Al_2O_3 layer. For a grating at normal incidence, the phase-matching condition for coupling into a guided mode of effective index n_{eff} and grating order m can be written as $\beta_{mode} = k_0 n_{eff} = 2\pi m/P$, so that the resonance condition becomes $\lambda_{GMR} = n_{eff}P/m$ [106].

The TM-GMR branch appears at a shorter wavelength than the TE-GMR branch because TM guided modes in a dielectric slab always possess a lower effective index than TE modes of the same order. In a conventional dielectric GMR structure with a high-index grating, the wavelength separation between TE and TM guided modes can often be interpreted in terms of their different effective indices in the slab waveguide. However, in the present structure the grating is formed by plasmonic nanoparticle chains on top of the Al_2O_3 slab and an underlying Au film, therefore, the observed resonances are hybrid GMR modes rather than purely dielectric slab modes. As discussed by Sahoo et al., such hybrid GMRs arise from the coherent coupling of the waveguide guided mode with plasmonic resonances, leading to mixed photonic–plasmonic branches whose spectral positions and polarization dependence are governed by the strength of this coupling. In our case, the TE branch couples predominantly to the longitudinal chain mode and behaves more like a photonic GMR with the field strongly confined inside the Al_2O_3 slab, while the TM branch has a larger contribution from plasmonic and metal-assisted components (transverse chain modes and SPP-like fields near the metal), which reduces the effective index of the hybrid mode and therefore shifts the TM GMR to shorter wavelengths compared with its TE counterpart. This interpretation is consistent with the field maps, where the TE hybrid GMR shows slab-confined standing waves with symmetric leakage, while the TM branch exhibits more asymmetric, metal-enhanced localization, consistent with the hybrid-GMR and metal-assisted GMR [107].

In the TE spectrum of Figure 5.14a, the resonance near $\sim$694 nm initially resembles an RA hybrid with GMR because it lies close to the cover RAc line. However, the corresponding field E-field map (Figure 5.15a) shows a clear standing-wave pattern within the Al_2O_3 slab, with multiple nodes characteristic of a guided TE mode with radiative beams from RAc.This combined behavior identifies the mode as an RAc–GMR hybrid. A pure RA, in contrast,

would not produce such slab-confined standing waves. Thus, the mode is not a simple RA but involves a guided TE mode. The AOI map (Figure 5.14c) confirms this interpretation: the TE GMR branch follows a angle depended dispersion, as expected for a guided mode, and undergoes an avoided crossing with the RAc line around ∼694 nm at normal transmission.

Besides this RAc–GMR hybrid, the TE spectrum Figure 5.14a exhibits another resonance near ∼902 nm that was initially assigned as a hybrid of RAs with GMR. Its field distribution reveals that it is again a hybrid involving a guided TE mode. At ∼902 nm, the field map (Figure 5.15b) shows a standing-wave pattern within the Al_2O_3 slab together with leakage in the ± 1 directions which is associated with RAs-GMR. The AOI map (Figure 5.14c) shows that the corresponding branch follows a slightly curved, indicating an avoided crossing between the TE guided mode and RAs.

In TM as Figure 5.14b, the LSPR(T) and the TM guided mode both interact with the RA. The curved TM-GMR branch intersects the RAc near ∼624 avoided crossing in the AOI map in Figure 5.14d similar to the TE case. The blueshift of the RAc–GMR resonance in TM is evident when compared with the corresponding TE mode, consistent with our earlier discussion. The H-field map (Figure 5.16a) at wavelength of 624 nm shows a standing-wave pattern confined within the Al_2O_3 slab together with Rayleigh-directed ± 1 beams, confirming again that the resonance is an RAc-GMR hybrid.

At longer wavelengths, near ∼914 nm and 1042 nm (Figure 5.14b), the TM dispersion is drawn towards the RAs and a nearby SPP-like branch supported at the Au/glass interface. The H-field map (Figure 5.16(b,c)) for both wavelengths in this region demonstrates intense confinement at the Au/glass interface alongside strong ± 1 diffraction lobes into the glass, identifying these mode as an RAs–SPP hybrids. A genuine GMR would exhibit primarily slab localization, whereas here the dominant localization occurs at the metal/glass interface, combined with RA-mediated leakage, confirming the SPP-like nature of these modes.

The experimental results in Figure 5.14 follow the same behavior. A resonance near ∼512 nm appears in TE, corresponding to the interband response seen in the simulations for this structure. Additional peaks near ∼642 nm (RAc–GMR) and ∼850 nm (second RAs–GMR hybrid) show good agreement with the simulated spectrum. A blueshift is observed in experimental TE compared with its simulation. Experimental TM resonances appear near ∼652 nm, ∼905 nm, and ∼1000 nm, corresponding to the simulated RAc–GMR and RAs–SPP features, respectively.

The thickness-dependent measurements in Figure 5.17 provide direct confirmation of the presence of GMR modes in this structure. When the Al_2O_3 thickness is varied, the wavelengths of both TE GMR branches in Figure 5.14 (the RAc–GMR hybrid at 694 nm and RAs–GMR hybrid the $\sim$902 nm) change, because the slab thickness enters the guided-mode dispersion relation. This clear dependence of the TE resonances on slab thickness is a strong indication that they originate from slab-guided modes coupled to RAc and RAs. In the thickness series of Figure 5.17, the GMR branch in TM moves with thickness, while the RA and SPP wavelengths remain nearly unchanged, confirming that this resonance arises from slab-guided TM modes coupled to the RA, whereas the RA and SPP features are insensitive to the spacer thickness, remain essentially unchanged. Rayleigh anomaly wavelengths depend only on the grating periodicity and the refractive index of the external medium in which the diffracted order propagates; therefore, they are independent of the Al_2O_3 spacer thickness. In contrast, changing the Al_2O_3 thickness modifies the guided-mode dispersion $n_{eff}(\lambda, d)$ in both TE and TM [108].

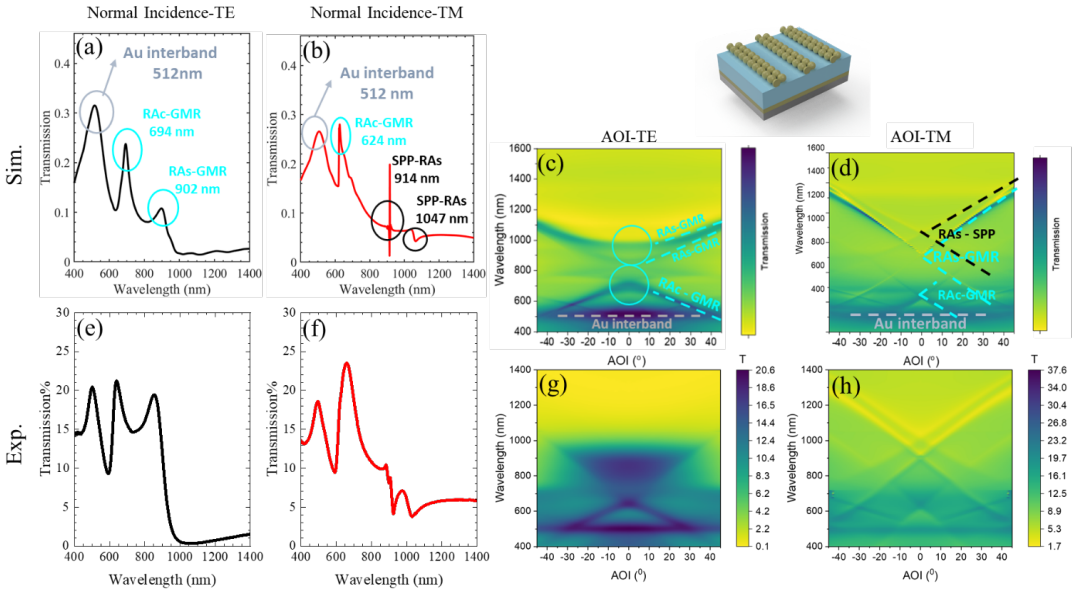

Figure 5.14 Simulated and experimental optical response of the glass/Au/Al_2O_3/nanoparticle chain structure. Panels (a) and (b) show the simulated normal incidence transmission spectra for TE (black) and TM (red) polarizations, respectively: in TE, the Au interband feature appears near 512 nm, while RA–GMR and RAc–GMR hybrids occur around 902 nm and 694 nm; in TM, the RAc–GMR mode appears near 624 nm and SPP–RAs hybrids are found at ∼914 nm and ∼1047 nm. Panels (e) and (f) present the corresponding experimental spectra, where a resonance near 512 nm in TE matches the simulated Au interband response, and additional peaks at ∼642 nm and ∼850 nm agree with the first and second RA–GMR hybrids, albeit with an overall blueshift relative to the simulations; the TM spectrum shows resonances near ∼652 nm, ∼905 nm, and around ∼ 1000 nm that correspond to the simulated RAc–GMR and RAs–SPP features. Panels (c) and (g) display the simulated and experimental AOI dispersion maps for TE polarization, highlighting the nearly dispersionless Au interband band together with the RAc–GMR and RA–GMR branches at the above wavelengths. Panels (d) and (h) show the TM AOI maps, where the dispersive RAs and RAc lines hybridize with the guided mode resonance (RAc–GMR) and with SPP modes on the Au film (RAs–SPP), in direct correspondence with the TM resonances identified in panels (b) and (f).

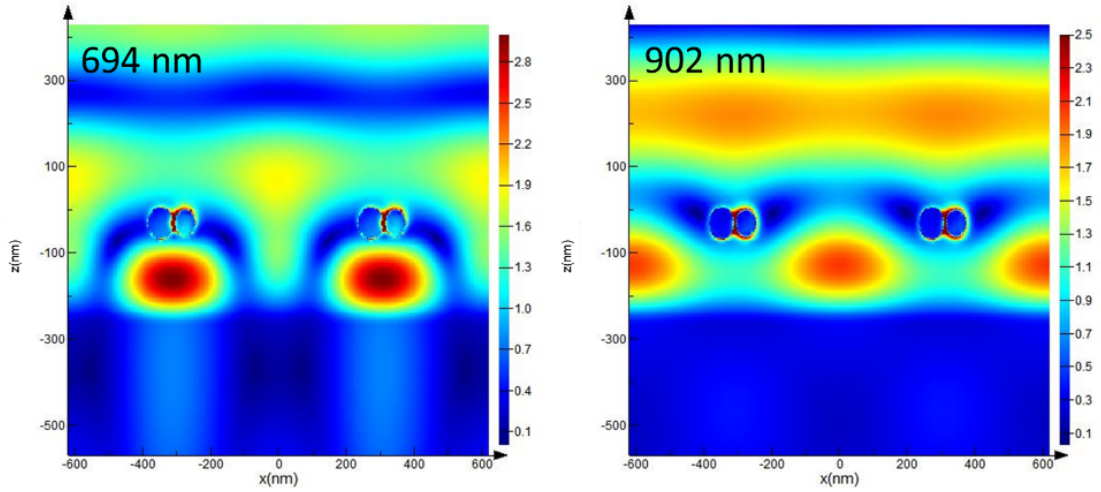

Figure 5.15 Electric-field distributions (XZ plane) for Structure 3 under TE polarization at the wavelengths of the two TE resonances. (a) At $\lambda \approx 694$ nm, the mode corresponds to an RAc–GMR hybrid. (b) At $\lambda \approx 902$ nm, the mode corresponds to an RAs–GMR hybrid.

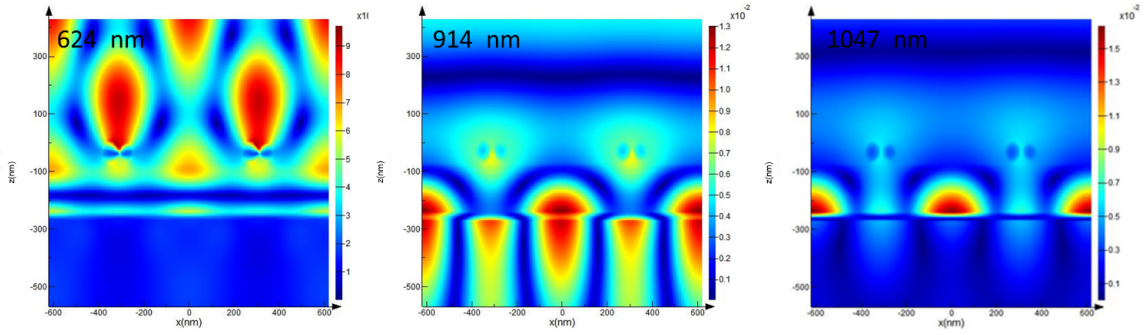

Figure 5.16 Magnetic-field distributions (XY plane) for Structure 3 under TM polarization at the wavelengths of the three TM resonances. (a) At $\lambda \approx 624$ nm, the field pattern identifies the mode as an RAc–GMR hybrid. (b) and (c) At $\lambda \approx 914$ nm and $\lambda \approx 1047$ nm, the H-field is tightly confined along the Au–glass interface, indicating excitation of an interface-bound SPP, and together with the diffraction RAs confirms these modes as RAs–SPP hybrids.

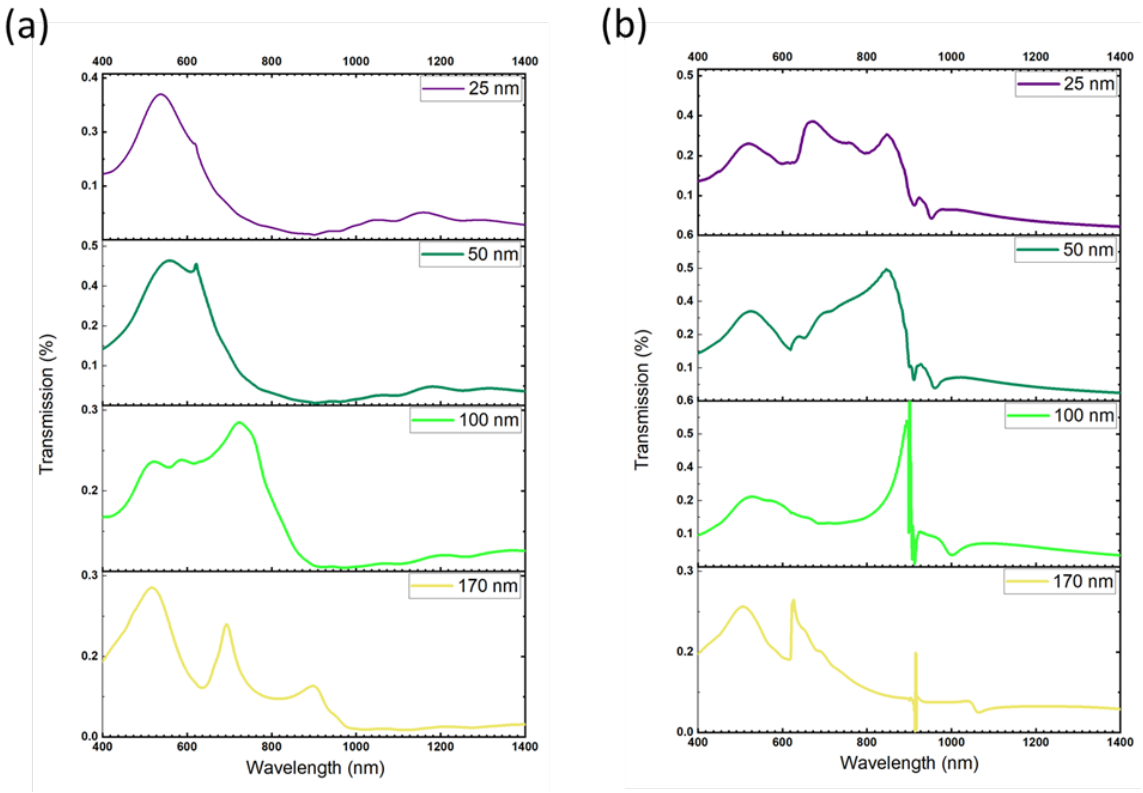

Figure 5.17 Normal-incidence transmission spectra of Structure 3 for different Al_2O_3 spacer thicknesses under (a) TE and (b) TM polarization. The GMR-related resonances exhibit strong thickness dependence, shifting systematically with increasing slab thickness due to changes in the guided-mode effective index. In contrast, thickness-independent features, such as the fixed Rayleigh-anomaly positions, the Au interband response near ∼500–520 nm, and the long-wavelength SPP–RA hybrid in TM, remain essentially unchanged. The clear redshift of the GMR modes with spacer thickness provides direct evidence that the corresponding resonances originate from slab-guided modes rather than Rayleigh or plasmonic excitations.

5.3.1.4 Structure 4: Glass/Au/Al_2O_3/L-Phenylalanine/NP Dimer Grating (Figure 5.18)

The AOI maps (Figure 5.18) for Structure 4 show that the dispersion shapes of the RAc–GMR, RAs–GMR, and RAs–SPP hybrids are essentially unchanged relative to Structure 3. However, coating the metasurface with an L-phenylalanine layer modifies the optical environment above the Al_2O_3 slab by increasing the effective refractive index and slightly increasing the overall optical thickness of the cavity. As a result, as shown in Figure 5.18 in both AOI and normal transmission spectra, all modes whose wavelength depends on the refractive indices at the interfaces exhibit a redshift relative to Structure 3 (Figure 5.14). The guided-mode resonances (both TE and TM) also redshift because filling the space above the slab with a

higher-index analyte increases the effective index n_{eff} of the guided modes and therefore, via the coupling condition $n_{eff}\lambda \approx mP$, shifts their resonance wavelengths. The RA–SPP hybrid appears at $\sim$919 nm and does not shift noticeably with the addition of the L-PA layer, indicating that it does not respond to the refractive-index change in the cover region, because this mode is dominated by the SPP at the Au/glass interface and by the substrate-side Rayleigh anomaly, both of which largely depend on the metal–glass optical environment.

Beyond this redshift, the L-PA layer also causes a moderate enhancement of the resonance intensities. This effect can be understood in terms of improved index matching and increased optical path length in the cavity. By partially matching the refractive indices of the cover and the Al_2O_3 spacer, the L-PA layer reduces Fresnel reflection losses at the top interface and allows more energy to be coupled into the slab and plasmonic modes [109]. At the same time, the increase in optical thickness enhances the confinement of the guided modes and hybrid resonances, leading to stronger field amplitudes in the cavity [110]. The corresponding normal-incidence transmission spectra exhibit slightly deeper dips or higher peaks at the new resonance wavelengths, reflecting this enhanced coupling. In the CD spectra, the strongest chiroptical signals appear near these hybrid resonances, and their intensities are larger than in the corresponding structure without L-PA (structure 3), consistent with the analyte's intrinsic chirality coupling to the superchiral near-fields of the NPoM cavity.

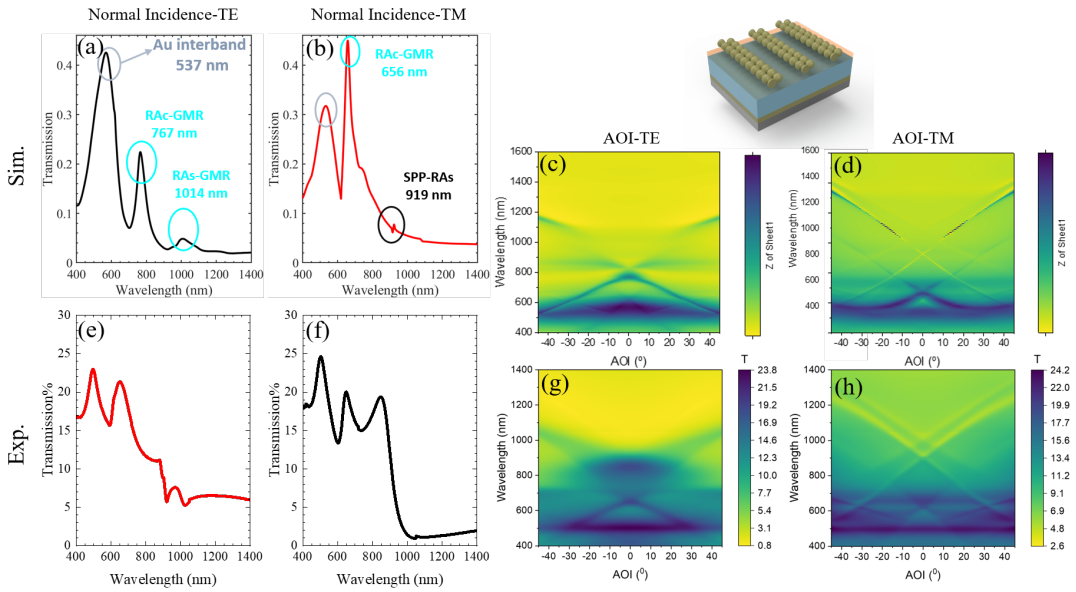

Figure 5.18 Simulated and experimental optical response of the glass/Au/Al_2O_3/L-PA/NP chain structure. Panels (a) and (b) show the simulated normal incidence transmission spectra for TE (black) and TM (red) polarizations, where TE exhibits the Au interband feature near 537 nm and RA–GMR resonances at ∼767 nm and ∼1014 nm, while TM displays an RAc–GMR mode around 656 nm and an SPP–RAs hybrid near 919 nm. The corresponding experimental spectra in panels (e) and (f) reveal similar modal features with simulation ones. Panels (c) and (g) present the simulated and experimental AOI dispersion maps for TE polarization, in which the RA–GMR branches and Au interband band match the TE resonances in panel (a) and (e). Panels (d) and (h) show the TM AOI maps, where the dispersive RAs branches and their coupling to the guided and SPP modes correspond directly to the TM resonances identified in panels (b) and (f), with a clear branch shift reflecting the overall red shifted response of the L-PA loaded structure.

5.3.2 CD Enhancement NPoM Cavities with Single Layer of NP dimer grating

Since the hybrid resonances identified in the transmission and AOI analyses directly determine the local field distributions responsible for chiroptical enhancement, we next examine how these mode interactions manifest in the experimentally measured CD response (calculated as the difference between right- and left-circularly polarized light). The measured CD response for these isolated structures revealed a progressive increase in chiroptical activity, confirming the systematic assembly of resonant components into the final hybrid cavity. The glass/NP dimer structure exhibited CD enhancement (Figure 5.19a) at wavelengths of 544 nm

and 909 nm, the latter can correspond to where RA-LSPR hybrid modes appeared in the transmission spectra. The glass/Au/NP dimer structure (Figure 5.19b) produced amplified CD extrema around 540 nm (associated with interband transitions) and 720 nm compared to the bare glass baseline; this can be attributed to the excitation of SPP modes by the planar mirror. Finally, the glass/Au/NP dimer structure (Figure 5.19c), featuring the full photonic cavity, further boosted the CD signal, particularly around 853 nm, which can be linked to RA-GMR hybrid coupling.

Finally, the single-layer NPoM structure, glass/Au/Al_2O_3/L-PA/NP dimer (Figure 5.19d), yielded the strongest single-layer CD amplitude around 628 nm, along with several strong peaks near 1000 nm arising from GMR-RA and SPP-RA modes. This represents a slight enhancement over the previous structure (Glass/Au/Al_2O_3/NP dimer) which is primarily due to the analyte's inherent chirality (κ) coupling with the superchiral near-field, providing the first direct measure of the amplification of CD within the NPoM cavity.

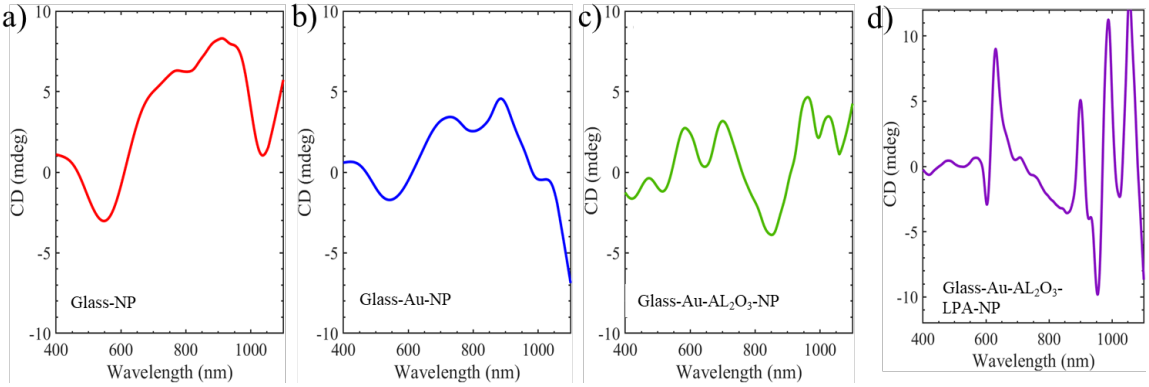

Figure 5.19 The measured CD for four distinct nanohole array configurations: (a) glass/NP chains, (b) glass/Au/NP chain, (c) glass/Au/Al_2O_3/NP chain, and (d) glass/Au/Al_2O_3/L-PA/NP chain.

5.3.3 Cross-Stacked Dimer: Maximum Intrinsic Chiral Enhancement

The ultimate step involved stacking a second NP layer at an oblique angle (15°, 30°, 45°) to create the intrinsically chiral cross-stacked dimer grating and maximize the field localization in the inter-layer gap.

A consistent observation across the structures with stacked layer (two layer of dimer gratings of NP) was that their transmission spectra were significantly broader than the single-layer configurations (Figure 5.20(a-d))). the overall transmission spectra of Cross-

Stacked structures tend to broaden due to enhanced radiative scattering and strong inter-layer coupling, while the strong CD response persists. Spectral broadening is fundamentally linked to increased total optical losses, where the resonance linewidth ($\Delta\lambda$) in relation to the quality factor Q is proportional to the total damping rate ($\Delta\lambda \propto \Gamma_{rad} + \Gamma_{non-rad}$) [111]. The addition of the second layer of nanoparticles dimers increases radiative scattering by providing additional diffraction channels for light outcoupling [112]. This means the second periodic layer acts as a new diffraction grating, increasing the number of possible momentum vectors (diffraction orders) that can couple the confined light out of the structure, thereby enhancing radiative decay (Γ_{rad}). Concurrently, strong inter-layer coupling results in hybridization between the modes of the two layers, substantially increasing the density of states and spectral complexity [113, 114], and thus significantly increasing the non-radiative ohmic losses ($\Gamma_{non-rad}$) due to a larger volume of metal [115], leading to a broader overall FWHM. This sustained strong CD, despite spectral broadening, is attributed to several factors facilitated by the Cross-Stacked geometry.

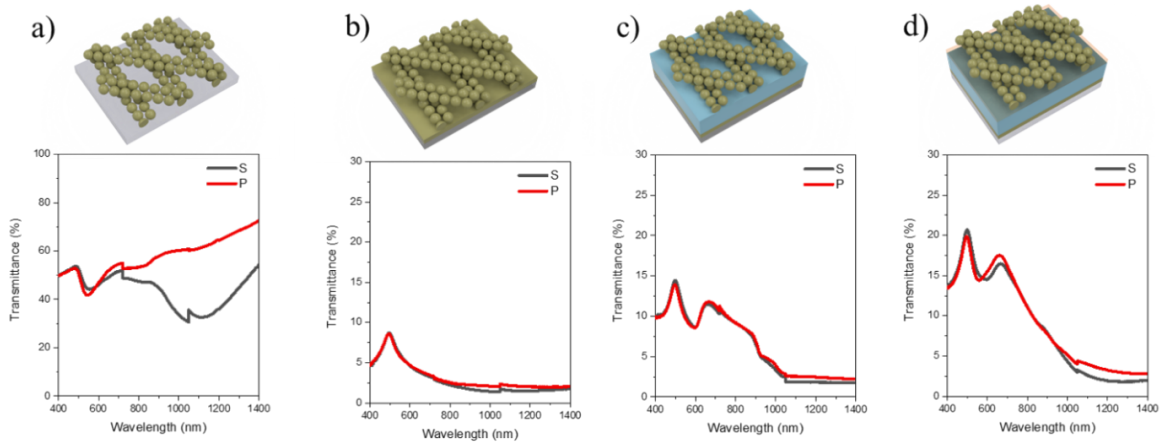

Figure 5.20 Experimental transmission spectra of TE (black) and TM (red) polarized light for each metasurface structure with a stacking angle of 45°. Schematics of metasurface structures consisting of cross-stacked nanoparticle chain layers (a second nanoparticle chain layer added at an oblique stacking angle): (a) glass/cross-stacked nanoparticle chain layers, (b) glass/Au/cross-stacked nanoparticle chain layers, (c) glass/Au/Al_2O_3/cross-stacked nanoparticle chain layers, and (d) glass/Au/Al_2O_3/L-PA/ cross-stacked nanoparticle chain layers.

Despite this broadening, the CD intensity increased substantially across all Cross-Stacked Configuration, resulting in a 100 times enhancement over the maximum CD response of

single layer of dimer. The CD response magnitude was dynamically dependent on the stacking angle (Figure 5.21(a-d)).

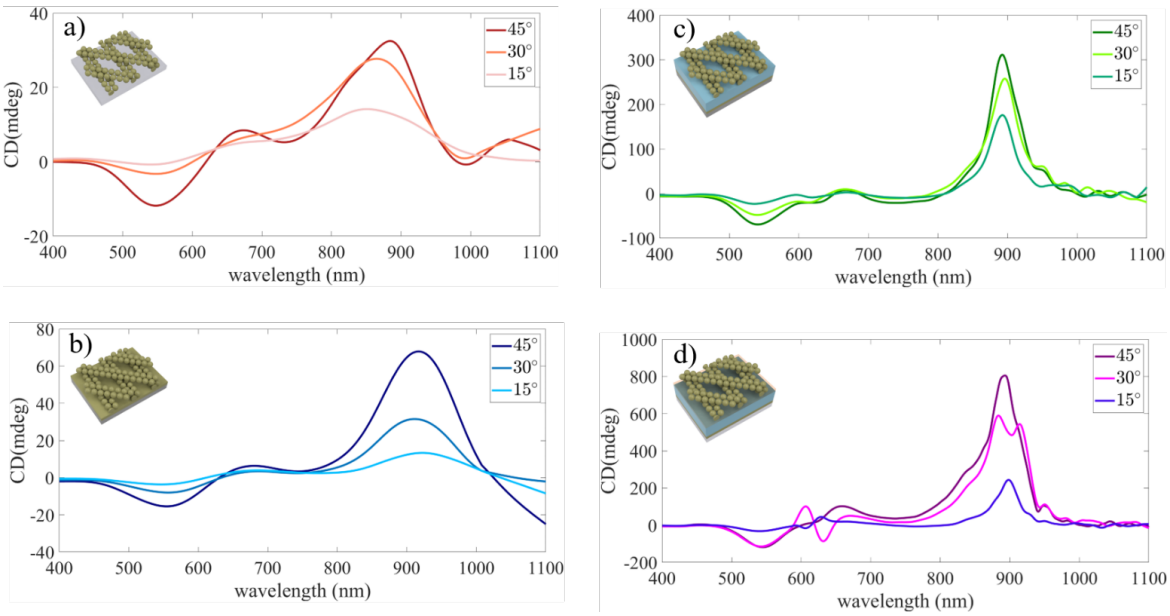

Figure 5.21 CD spectra of the corresponding metasurfaces at various stacking angles (15°, 30°, and 45°) for: (a) glass/ cross-stacked nanoparticle chain layers, (b) glass/Au/cross-stacked nanoparticle chain layers, (c) glass/Au/Al_2O_3/cross-stacked nanoparticle chain layers, and (d) glass/Au/Al_2O_3/L-PA/cross-stacked nanoparticle chain layers.

We investigated the chiroptical response of the metasurface by varying the stacking angle between the crossed nanoparticle chain layers. This angle, which represents the inter-layer rotation between the two stacked layers (each containing a nanoparticle dimers), directly governs the chiroptical response and circular dichroism strength of the metasurface. We placed the stacked layer structures at different angles, specifically 15°, 30°, and 45°, and recorded the corresponding CD responses. Our observations confirmed that the stacking angle 45° yielded a stronger CD response compared to the other angles investigated.

For the bare Glass/NP cross-stacked dimer gratings structure (Figure 5.21a) the CD extrema became stronger compared to the single-layer baseline. The CD amplification occurs at wavelengths located in the vicinity of the hybrid-mode resonances revealed in the single-layer case. The Glass/Au/cross-stacked dimer gratings structure (Figure 5.21b) further increased the CD magnitude due to the planar plasmonic mirror. The CD enhancement happen in the wavelength which CD of single layers shows enhancement because of the hybrid modes.In the Glass/Au/Al_2O_3 structure (Figure 5.21c), multiple CD peaks persisted near 900 nm despite the absence of clear transmission feature (Figure 5.20c). This phenomenon

is consistent with strong scattering and absorption from highly hybridized modes, which maintain high CD via maximal helicity coupling even when transmission dips are damped.

The largest CD magnitude of ∼800 mdeg was recorded for the full Glass/Au/Al_2O_3/L-PA cavity with the cross-stacked dimer (Figure 5.21d) where we can see the active role of L-PA in comparison with the structure without L-PA. The superior enhancement of this CD compared to its counterpart single-layer structure is due to the primary mechanisms outlined in Chapter 2. Briefly, the generation of nearly collinear Electric and Magnetic fields within the vertical nanogap, which is essential for maximizing the chirality enhancement factor $\chi \propto \mathrm{Im}\{E^* \cdot H\}$. This vertical nanogap acts as the chiral hotspot, ensuring the most intense superchiral fields are localized in the region highly accessible to the analyte molecules, maximizing the sensing volume overlap.

Furthermore, the bilayer stacking substantially increases the hybridization strength between the RAs with localized LSPR modes and the photonic/plasmonic lattice modes. Crucially, the presence of the L-PA film significantly amplified the CD response compared to the bare Glass/Au/Al_2O_3/cross-stacked dimer gratings structure (Figure 5.21(c-d)). This additional boost occurs because the molecular chirality (κ) of the L-PA strongly enhances the coupling to the localized superchiral fields where the field is maximized due to the amplified hybridization. We clearly observed that the Glass/Au/Al_2O_3/L-PA/NP dimer grating cavity exhibits a markedly stronger CD response compared to the glass substrate with only a single dimer grating, consistent with the hybrid modes identified earlier. The strong CD enhancement demonstrated by the glass/Au/Al_2O_3/L-PA motivates further optimization. As future work, we will conduct numerical simulations of the cross-stacked double-layer design to refine its geometry, and we will compute AOI dispersion maps and near-field distributions to fully characterize the additional hybrid modes arising from the bilayer configuration.

Chapter 6

Conclusion

This thesis presented a comprehensive investigation into enhancing molecular circular dichroism through engineered plasmonic and photonic metasurfaces, with both extrinsic and intrinsic chirality mechanisms. Beginning with achiral gold nanohole arrays, we demonstrated how controlled oblique illumination breaks the symmetry of an otherwise mirror-symmetric lattice, enabling sizeable CD responses in the visible region. These nanohole arrays were fabricated using electron-beam lithography followed by metal evaporation, ensuring precise control over hole diameter, periodicity, and gold thickness. A custom-built optical transmission setup, equipped with rotation axes to control the polar angle (θ) and azimuthal angle (ϕ), was used to induce and tune extrinsic chirality, as described in detail in the instrumentation chapter. By systematically correlating these measurements with finite-element simulations, we clarified how the incidence angle redistributes the electric and magnetic near fields, leading to measurable and tunable extrinsic chiroptical activity.

Building on this foundation, the single-layer nanohole substrate was integrated into a MDM cavity to further amplify the local electromagnetic environment. The multilayer $Au/Al_2O_3/Au$ structure was produced by sequential electron-beam evaporation and lithography, enabling reliable formation of a photonic cavity supporting magnetic-dipole resonances. The resulting hybrid plasmonic–photonic cavity generated intense asymmetric near fields and circulating displacement currents that are absent in single-layer geometries. Consequently, the chirality enhancement factor increased by an additional order of magnitude, and a 50-fold improvement in the CD signal of L-phenylalanine was experimentally demonstrated. These results confirm that cavity-assisted field confinement, particularly the co-localization of

electric and magnetic components, is an effective route for boosting molecular chiroptical signatures using fully achiral architectures.

Following the cavity-induced enhancement demonstrated in the MDM nanohole system, we extended our investigation toward an intrinsically chiral cavity design capable of producing comparably intense, chiral near fields. This motivation led to the development of the NPoM cavity, in which plasmonic nanoparticle dimer gratings are integrated above a thin-film Au/Al_2O_3 photonic cavity. The fabrication of this platform relied on LIL combined with Template-Assisted Self-Assembly, as detailed in the fabrication chapter. The NPoM architecture was conceived to exploit the hybrid interaction between localized surface plasmons, lattice diffraction modes, and cavity-supported resonances with RA, which arises from the diffraction orders of the grating, thereby establishing strongly confined electromagnetic hotspots within nanoscale gaps.

To disentangle the role of each constitutive layer, the study began with single-layer nanoparticle dimer gratings deposited sequentially on glass, glass/Au, glass/Au/Al_2O_3, and glass/Au/Al_2O_3 coated with an L-phenylalanine film. This incremental approach provided a clear means of isolating the influence of the metallic mirror, the dielectric spacer, and the chiral analyte on the optical response. Transmission measurements and angle-resolved dispersion maps revealed the progressive emergence and evolution of guided-mode resonances, and photonic modes, Rayleigh anomalies and their hybrid modes as additional layers were introduced. These resonances manifested as distinct features in the wavelength–angle domain, confirming that the interplay between the nanoparticle array and the cavity modifies the landscape substantially. At the spectral positions where these hybrid modes were strongest, we observed a corresponding enhancement in circular dichroism, highlighting the direct connection between resonance-driven field confinement and chiroptical amplification.

Building on the single-layer studies, a second nanoparticle grating was then cross-stacked at a controlled angle to introduce genuine three-dimensional intrinsic chirality and to form confined vertical nanogaps. This stacked-layer configuration was specifically designed to harness the cavity-assisted hotspot localization and the geometric chirality arising from the rotating. Circular dichroism measurements confirmed a marked enhancement in the stacked NPoM structure, particularly at wavelengths associated with hybridized RA and GMR modes. Compared to the response from a grating deposited on bare glass, the cavity-supported stacked system exhibited substantially stronger CD signals, including for the L-phenylalanine layer, thereby validating the effectiveness of combining intrinsic chiral geometry with cavity-enhanced field localization.

The results obtained here provide a clear pathway for further advancement. The pronounced influence of hybrid resonances and nanogap-confined fields suggests that refining the NPoM cavity geometry through optimization of particle periodicity, stacking angle, and cavity thickness could further elevate the chiroptical response. Numerical modelling will play a central role in guiding these refinements by resolving the electric-field distributions associated with the most effective hybrid modes. Additionally, extending angle-resolved dispersion measurements to the stacked structure will allow a more complete reconstruction of the complex modal interactions within the intrinsically chiral cavity. Together, these steps will deepen the understanding of intrinsic cavity-enhanced CD and support the development of highly sensitive, tunable chiroptical platforms for molecular detection.

References

[1] Matthias Wollenhaupt. “Photoelectron circular dichroism in different ionization regimes”. In: *New Journal of Physics* 18.12 (Dec. 2016), p. 121001. ISSN: 1367-2630. DOI: 10.1088/1367-2630/18/12/121001.

[2] Agata Chotera-Ouda, Katarzyna Trzeciak, and Marek J. Potrzebowski. “Importance of chirality in the self-organizing peptides – from single molecules to functional supramolecular structures”. In: *Physical Chemistry Chemical Physics* 27.35 (2025), pp. 18062–18092. ISSN: 1463-9076, 1463-9084. DOI: 10.1039/D5CP01562F.

[3] Kyu-Tae Lee et al. “Enantiomer-Selective Molecular Sensing in the Nonlinear Optical Regime via Upconverting Chiral Metamaterials”. In: *Advanced Functional Materials* 32.43 (Oct. 2022), p. 2208641. ISSN: 1616-301X, 1616-3028. DOI: 10.1002/adfm.202208641.

[4] Jessica Ceramella et al. “A Look at the Importance of Chirality in Drug Activity: Some Significative Examples”. In: *Applied Sciences* 12.21 (Oct. 2022), p. 10909. ISSN: 2076-3417. DOI: 10.3390/app122110909.

[5] Simimole Haleema et al. “Enantiomerically pure compounds related to chiral hydroxy acids derived from renewable resources”. In: *RSC Advances* 2.25 (2012), p. 9257. ISSN: 2046-2069. DOI: 10.1039/c2ra21205f.

[6] Hafiz Saad Khaliq et al. “Manifesting Simultaneous Optical Spin Conservation and Spin Isolation in Diatomic Metasurfaces”. In: *Advanced Optical Materials* 9.8 (Apr. 2021), p. 2002002. ISSN: 2195-1071, 2195-1071. DOI: 10.1002/adom.202002002.

[7] Mengxin Ren et al. “Giant nonlinear optical activity in a plasmonic metamaterial”. In: *Nature Communications* 3.1 (May 2012), p. 833. ISSN: 2041-1723. DOI: 10.1038/ncomms1805.

[8] Yuwen Wang et al. “Chiral Engineered Biomaterials: New Frontiers in Cellular Fate Regulation for Regenerative Medicine”. In: *Advanced Functional Materials* 35.20 (May 2025), p. 2419610. ISSN: 1616-301X, 1616-3028. DOI: 10.1002/adfm.202419610.

[9] Andrew Lininger et al. “Chirality in Light–Matter Interaction”. In: *Advanced Materials* 35.34 (Aug. 2023), p. 2107325. ISSN: 0935-9648, 1521-4095. DOI: 10.1002/adma.202107325.

[10] Chun-Fang Li and Zhi-Juan Hu. *On a heuristic point of view concerning the optical activity*. Sept. 2022. DOI: 10.48550/arXiv.2209.07982.

[11] H. D. Flack. “Louis Pasteur’s discovery of molecular chirality and spontaneous resolution in 1848, together with a complete review of his crystallographic and chemical work”. In: *Acta Crystallographica Section A Foundations of Crystallography* 65.5 (Sept. 2009), pp. 371–389. ISSN: 0108-7673. DOI: 10.1107/S0108767309024088.

[12] Rong-Ming Ho et al. “Transfer of Chirality from Molecule to Phase in Self-Assembled Chiral Block Copolymers”. In: *Journal of the American Chemical Society* 134.26 (July 2012), pp. 10974–10986. ISSN: 0002-7863, 1520-5126. DOI: 10.1021/ja303513f.

[13] Semere Araya Asefa et al. “Chiral Metasurfaces: A Review of the Fundamentals and Research Advances”. In: *Applied Sciences* 13.19 (Sept. 2023), p. 10590. ISSN: 2076-3417. DOI: 10.3390/app131910590.

[14] Gábor Szilvágyi et al. “Conformational studies on chiral rhodium complexes by ECD and VCD spectroscopy”. In: *Chirality* 23.4 (Apr. 2011), pp. 294–299. ISSN: 0899-0042, 1520-636X. DOI: 10.1002/chir.20916.

[15] Fujiang Zhu et al. “Raman Optical Activity: A Tool for Protein Structure Analysis”. In: *Structure* 13.10 (Oct. 2005), pp. 1409–1419. ISSN: 09692126. DOI: 10.1016/j.str.2005.07.009.

[16] Xiaoli Wang and Zhiyong Tang. “Circular Dichroism Studies on Plasmonic Nanostructures”. In: *Small* 13.1 (Jan. 2017), p. 1601115. ISSN: 16136810. DOI: 10.1002/smll.201601115.

[17] Jun Lu et al. “Chiral Plasmonic Nanochains *via* the Self-Assembly of Gold Nanorods and Helical Glutathione Oligomers Facilitated by Cetyltrimethylammonium Bromide Micelles”. In: *ACS Nano* 11.4 (Apr. 2017), pp. 3463–3475. ISSN: 1936-0851, 1936-086X. DOI: 10.1021/acsnano.6b07697.

[18] Cuiping Ma et al. “Chiral Optofluidics with a Plasmonic Metasurface Using the Photothermal Effect”. In: *ACS Nano* 15.10 (Oct. 2021), pp. 16357–16367. ISSN: 1936-0851, 1936-086X. DOI: 10.1021/acsnano.1c05658.

[19] Lei Wang and Luogen Deng. “Plasmonic Circular Dichroism of the Helical Nanosphere Assemblies and the Helical Nanoellipsoid Assemblies”. In: *Plasmonics* 10.2 (Nov. 2014), pp. 399–409. ISSN: 1557-1963. DOI: 10.1007/s11468-014-9821-1.

[20] Y. Zhao, M.A. Belkin, and A. Alù. “Twisted optical metamaterials for planarized ultrathin broadband circular polarizers”. In: *Nat. Commun.* 3.1 (May 2012). ISSN: 2041-1723. DOI: 10.1038/ncomms1877.

[21] Eric Sidney Aaron Goerlitzer et al. “Molecular-Induced Chirality Transfer to Plasmonic Lattice Modes”. In: *ACS Photonics* 10.6 (May 2023), pp. 1821–1831. ISSN: 2330-4022. DOI: 10.1021/acsphotonics.3c00174.

[22] Ben M. Maoz et al. “Chiroptical Effects in Planar Achiral Plasmonic Oriented Nanohole Arrays”. In: *Nano Lett.* 12.5 (Apr. 2012), pp. 2357–2361. ISSN: 1530-6992. DOI: 10.1021/nl300316f.

[23] Matteo Venturi et al. “Plasmon-enhanced circular dichroism spectroscopy of chiral drug solutions”. In: *The Journal of Chemical Physics* 159.15 (Oct. 2023), p. 154703. ISSN: 0021-9606, 1089-7690. DOI: 10.1063/5.0169826.

[24] Zhiyuan Fan and Alexander O. Govorov. “Plasmonic Circular Dichroism of Chiral Metal Nanoparticle Assemblies”. In: *Nano Lett.* 10.7 (June 2010), pp. 2580–2587. ISSN: 1530-6992. DOI: 10.1021/nl101231b.

[25] D. Vestler et al. “Circular dichroism enhancement in plasmonic nanorod metamaterials”. In: *Opt. Express* 26.14 (June 2018), p. 17841. ISSN: 1094-4087. DOI: 10.1364/oe.26.017841.

[26] Thomas J. Ugras et al. “Transforming achiral semiconductors into chiral domains with exceptional circular dichroism”. In: *Science* 387.6733 (Jan. 2025), eado7201. ISSN: 0036-8075, 1095-9203. DOI: 10.1126/science.ado7201.

[27] Manuel Nunez-Martínez et al. “Chiroptical hybrid nanomaterials based on metal nanoparticles and biomolecules”. In: *Adv. Colloid Interface Sci.* 341 (July 2025), p. 103501. ISSN: 0001-8686. DOI: 10.1016/j.cis.2025.103501.

[28] Kyle Van Gordon et al. “Single Crystal and Pentatwinned Gold Nanorods Result in Chiral Nanocrystals with Reverse Handedness”. In: *Angew. Chem. Int. Ed.* 63.26 (May 2024). ISSN: 1521-3773. DOI: 10.1002/anie.202403116.

[29] Vikas Yadav and Soumik Siddhanta. “Engineering chiral plasmonic nanostructures for gain-assisted plasmon amplification and tunable enhancement of circular dichroism”. In: *Mater. Adv.* 3.3 (2022), pp. 1825–1833. ISSN: 2633-5409. DOI: 10.1039/d1ma01067k.

[30] Daniel Vestler, Assaf Ben-Moshe, and Gil Markovich. “Enhancement of Circular Dichroism of a Chiral Material by Dielectric Nanospheres”. In: *J. Phys. Chem. C* 123.8 (Feb. 2019), pp. 5017–5022. ISSN: 1932-7455. DOI: 10.1021/acs.jpcc.8b10975.

[31] Maxim L. Nesterov et al. “The Role of Plasmon-Generated Near Fields for Enhanced Circular Dichroism Spectroscopy”. In: *ACS Photonics* 3.4 (Apr. 2016), pp. 578–583. ISSN: 2330-4022. DOI: 10.1021/acsphotonics.5b00637.

[32] Maryam Mirahmadi et al. “Ultrasensitive and Tunable Achiral Metamaterial Substrates as Nanobiosensors for Enantiomer Detection”. In: *ACS Applied Materials & Interfaces* 17.47 (Nov. 2025), pp. 65270–65280. ISSN: 1944-8244, 1944-8252. DOI: 10.1021/acsami.5c14316.

[33] Tiago Ramos Leite et al. “Resonant Plasmonic–Biomolecular Chiral Interactions in the Far-Ultraviolet: Enantiomeric Discrimination of sub-10 nm Amino Acid Films”. In: *Nano Lett.* 22.18 (Sept. 2022), pp. 7343–7350. ISSN: 1530-6992. DOI: 10.1021/acs.nanolett.2c01724.

[34] Jose García-Guirado et al. “Enantiomer-Selective Molecular Sensing Using Racemic Nanoplasmonic Arrays”. In: *Nano Lett.* 18.10 (Sept. 2018), pp. 6279–6285. ISSN: 1530-6992. DOI: 10.1021/acs.nanolett.8b02433.

[35] Abraham Vázquez-Guardado and Debashis Chanda. “Superchiral Light Generation on Degenerate Achiral Surfaces”. In: *Physical Review Letters* 120.13 (Mar. 2018). ISSN: 1079-7114. DOI: 10.1103/physrevlett.120.137601.

[36] Siyi Wang et al. “Extrinsic chiral plasmonic sensors based on a nanohole array”. In: *Optics Letters* 50.5 (Mar. 2025), p. 1645. ISSN: 0146-9592, 1539-4794. DOI: 10.1364/OL.547913.

[37] Changlong Hao et al. “Assembled Plasmonic Asymmetric Heterodimers with Tailorable Chiroptical Response”. In: *Small* 10.9 (May 2014), pp. 1805–1812. ISSN: 1613-6810, 1613-6829. DOI: 10.1002/smll.201303755.

[38] Xiang-Tian Kong et al. “Plasmonic Chirality and Circular Dichroism in Bioassembled and Nonbiological Systems: Theoretical Background and Recent Progress”. In: *Advanced Materials* 32.41 (Oct. 2020), p. 1801790. ISSN: 0935-9648, 1521-4095. DOI: 10.1002/adma.201801790.

[39] Emilija Petronijevic et al. “Extrinsic Chirality and Circular Dichroism at Visible Frequencies Enabled by Birefringent α-MoO_3 Nanoscale-Thick Films: Implications for Chiro-Optical Control”. In: *ACS Applied Nano Materials* 5.4 (Apr. 2022), pp. 5609–5616. ISSN: 2574-0970, 2574-0970. DOI: 10.1021/acsanm.2c00565.

[40] Ismael Barba García et al. “A complementary chiral metamaterial with giant electromagnetic activity and low losses”. In: *The 7th META Conference Proceedings*. 2016.

[41] X. Guo, C. Liu, and H.C. Ong. “Generalization of the Circular Dichroism from Metallic Arrays That Support Bloch-Like Surface Plasmon Polaritons”. In: *Phys. Rev. Appl.* 15.2 (Feb. 2021), p. 024048. DOI: 10.1103/PhysRevApplied.15.024048.

[42] P. Moroshkin, M.-J. Yu, and J. Xu. “Spin-momentum-locking–induced dynamic circular dichroism in extraordinary optical transmission”. In: *Phys. Rev. A* 107.3 (Mar. 2023), p. 033504. DOI: 10.1103/PhysRevA.107.033504.

[43] Wenjing Yan et al. “Self-Assembly of Chiral Nanoparticle Pyramids with Strong *R* / *S* Optical Activity”. In: *Journal of the American Chemical Society* 134.36 (Sept. 2012), pp. 15114–15121. ISSN: 0002-7863, 1520-5126. DOI: 10.1021/ja3066336.

[44] Murali Golla et al. “DNA-Decorated, Helically Twisted Nanoribbons: A Scaffold for the Fabrication of One-Dimensional, Chiral, Plasmonic Nanostructures”. In: *Angewandte Chemie International Edition* 58.12 (Mar. 2019), pp. 3865–3869. ISSN: 1433-7851, 1521-3773. DOI: 10.1002/anie.201813900.

[45] Patrick T. Probst et al. “Mechano-tunable chiral metasurfaces via colloidal assembly”. In: *Nature Materials* 20.7 (July 2021), pp. 1024–1028. ISSN: 1476-1122, 1476-4660. DOI: 10.1038/s41563-021-00991-8.

[46] Mohammad Adnan et al. “Selective Directional Enhancement in Gold/Perovskite Quantum Dot Metasurfaces”. In: *Advanced Optical Materials* 13.13 (May 2025), p. 2403397. ISSN: 2195-1071, 2195-1071. DOI: 10.1002/adom.202403397.

[47] Swagato Sarkar et al. “Hybridized Guided-Mode Resonances via Colloidal Plasmonic Self-Assembled Grating”. In: *ACS Applied Materials & Interfaces* 11.14 (Apr. 2019), pp. 13752–13760. ISSN: 1944-8244, 1944-8252. DOI: 10.1021/acsami.8b20535.

[48] James Clerk Maxwell. “VIII. A dynamical theory of the electromagnetic field”. In: *Philosophical Transactions of the Royal Society of London* 155 (Dec. 1865), pp. 459–512. DOI: 10.1098/rstl.1865.0008.

[49] Huajin Chen et al. “Tailoring azimuthal optical force on lossy chiral particles in Bessel beams”. In: *Physical Review A* 90.4 (Oct. 2014), p. 043850. ISSN: 1050-2947, 1094-1622. DOI: 10.1103/PhysRevA.90.043850.

[50] Hyun Sung Park et al. “A General Recipe for Nondispersive Optical Activity in Bilayer Chiral Metamaterials”. In: *Advanced Optical Materials* 7.19 (Oct. 2019), p. 1801729. ISSN: 2195-1071, 2195-1071. DOI: 10.1002/adom.201801729.

[51] Alessandro Belardini et al. “Chiral light intrinsically couples to extrinsic/pseudo-chiral metasurfaces made of tilted gold nanowires”. In: *Scientific Reports* 6.1 (Aug. 2016), p. 31796. ISSN: 2045-2322. DOI: 10.1038/srep31796.

[52] Hanan Ali et al. “Maximum Chirality Empowered by a Bound State in a Continuum in a Plasmonic Metasurface”. In: *ACS Applied Optical Materials* 2.5 (May 2024), pp. 825–833. ISSN: 2771-9855, 2771-9855. DOI: 10.1021/acsaom.4c00097.

[53] Éadaoin McClean-Ilten and Dominic Zerulla. “Nanoscale Tailored Plasmonic Material for Optimum Broadband Solar Harvesting”. In: *Advanced Optical Materials* 4.3 (Mar. 2016), pp. 413–418. ISSN: 2195-1071, 2195-1071. DOI: 10.1002/adom.201500513.

[54] Steven J. Byrnes. *Multilayer optical calculations*. Dec. 2020. DOI: 10.48550/arXiv.1603.02720.

[55] Sergey Kruk et al. “Enhanced Magnetic Second-Harmonic Generation from Resonant Metasurfaces”. In: *ACS Photonics* 2.8 (Aug. 2015), pp. 1007–1012. ISSN: 2330-4022, 2330-4022. DOI: 10.1021/acsphotonics.5b00215.

[56] M. G. Moharam et al. “Formulation for stable and efficient implementation of the rigorous coupled-wave analysis of binary gratings”. In: *Journal of the Optical Society of America A* 12.5 (May 1995), p. 1068. ISSN: 1084-7529, 1520-8532. DOI: 10.1364/JOSAA.12.001068.

[57] Bo Zhao, Atsushi Sakurai, and Zhuomin M. Zhang. “Polarization Dependence of the Reflectance and Transmittance of Anisotropic Metamaterials”. In: *Journal of Thermophysics and Heat Transfer* 30.1 (Jan. 2016), pp. 240–246. ISSN: 0887-8722, 1533-6808. DOI: 10.2514/1.T4587.

[58] Jun Qin et al. “Switching the optical chirality in magnetoplasmonic metasurfaces using applied magnetic fields”. In: *ACS Nano* 14.3 (Mar. 2020), pp. 2808–2816.

[59] Kyle W. Smith et al. “Exploiting Evanescent Field Polarization for Giant Chiroptical Modulation from Achiral Gold Half-Rings”. In: *ACS Nano* 12.11 (Nov. 2018), pp. 11657–11663. ISSN: 1936-0851, 1936-086X. DOI: 10.1021/acsnano.8b07060.

[60] Ershad Mohammadi et al. “Accessible Superchiral Near-Fields Driven by Tailored Electric and Magnetic Resonances in All-Dielectric Nanostructures”. In: *ACS Photonics* 6.8 (July 2019), pp. 1939–1946. ISSN: 2330-4022. DOI: 10.1021/acsphotonics.8b01767.

[61] E. Mohammadi et al. “Nanophotonic Platforms for Enhanced Chiral Sensing”. In: *ACS Photonics* 5.7 (July 2018), pp. 2669–2675. ISSN: 2330-4022, 2330-4022. DOI: 10.1021/acsphotonics.8b00270.

[62] P. Mandal. “Large Circular Dichroism in MDM Plasmonic Metasurface with Subwavelength Crescent Aperture”. In: *Plasmonics* 13.6 (Mar. 2018), pp. 2229–2237. ISSN: 1557-1963. DOI: 10.1007/s11468-018-0742-2.

[63] Yongkai Wang et al. “Circular Dichroism Enhancement and Biosensing Application of Composite Dielectric Chiral Nanostructures”. In: *J. Phys. Chem. C* 125.45 (2021), pp. 25243–25252. DOI: 10.1021/acs.jpcc.1c07138.

[64] Tun Cao and Martin J. Cryan. “Study of incident angle dependence for dual-band double negative-index material using elliptical nanohole arrays”. In: *J. Opt. Soc. Am. A* 29.3 (Mar. 2012), pp. 209–215. DOI: 10.1364/JOSAA.29.000209.

[65] Stanislaw Olszewski. “Electrodynamics of the Electron Orbital Motion in the Hydrogen Atom Considered in Reference to the Microstructure of the Electron Particle and Its Spin”. In: *Journal of Modern Physics* 06.15 (2015), pp. 2202–2210. ISSN: 2153-1196, 2153-120X. DOI: 10.4236/jmp.2015.615224.

[66] Angela I. Barreda et al. “Hybrid photonic-plasmonic cavities based on the nanoparticle-on-a-mirror configuration”. In: *Photonics Research* 9.12 (Dec. 2021), p. 2398. ISSN: 2327-9125. DOI: 10.1364/PRJ.433761.

[67] Wei Peng et al. “Construction of nanoparticle-on-mirror nanocavities and their applications in plasmon-enhanced spectroscopy”. In: *Chemical Science* 15.8 (2024), pp. 2697–2711. ISSN: 2041-6520, 2041-6539. DOI: 10.1039/D3SC05722D.

[68] Olha Aftenieva et al. “Directional Amplified Photoluminescence through Large-Area Perovskite-Based Metasurfaces”. In: *ACS Nano* 17.3 (Feb. 2023), pp. 2399–2410. ISSN: 1936-0851, 1936-086X. DOI: 10.1021/acsnano.2c09482.

[69] Junxi Zhang, Lide Zhang, and Wei Xu. “Surface plasmon polaritons: physics and applications”. In: *Journal of Physics D: Applied Physics* 45.11 (Mar. 2012), p. 113001. ISSN: 0022-3727, 1361-6463. DOI: 10.1088/0022-3727/45/11/113001.

[70] Fangqiang Li et al. “MEMS-based plasmon infrared emitter with hexagonal hole arrays perforated in the Al-SiO_2 -Si structure”. In: *Journal of Micromechanics and Microengineering* 21.10 (Oct. 2011), p. 105023. ISSN: 0960-1317, 1361-6439. DOI: 10.1088/0960-1317/21/10/105023.

[71] Ren-Jie Chen et al. “Raman generation with resonant periodic nanopatterns”. en. In: *Opt. Express* 33.11 (June 2025), pp. 22244–22254.

[72] Mohammad Shyiq Amin, Jae Woong Yoon, and Robert Magnusson. “Optical transmission filters with coexisting guided-mode resonance and Rayleigh anomaly”. In: *Applied Physics Letters* 103.13 (Sept. 2013), p. 131106. ISSN: 0003-6951, 1077-3118. DOI: 10.1063/1.4823532.

[73] Nir Levanon et al. “Angular Transmission Response of In-Plane Symmetry-Breaking Quasi-BIC All-Dielectric Metasurfaces”. In: *ACS Photonics* 9.11 (Nov. 2022), pp. 3642–3648. ISSN: 2330-4022, 2330-4022. DOI: 10.1021/acsphotonics.2c01069.

[74] H. Gao et al. “Rayleigh anomaly-surface plasmon polariton resonances in palladium and gold subwavelength hole arrays”. In: *Optics Express* 17.4 (Feb. 2009), p. 2334. ISSN: 1094-4087. DOI: 10.1364/OE.17.002334.

[75] Fanghui Ren et al. “Effect of finite metallic grating size on Rayleigh anomaly-surface plasmon polariton resonances”. In: *Optics Express* 23.22 (Nov. 2015), p. 28868. ISSN: 1094-4087. DOI: 10.1364/OE.23.028868.

[76] Lei Zhou et al. “Light Extraction of Trapped Optical Modes in Polymer Light-Emitting Diodes with Nanoimprinted Double-Pattern Gratings”. In: *ACS Applied Materials & Interfaces* 6.20 (Oct. 2014), pp. 18139–18146. ISSN: 1944-8244, 1944-8252. DOI: 10.1021/am5050357.

[77] Xiaorui Tian, Yurui Fang, and Mengtao Sun. “Formation of Enhanced Uniform Chiral Fields in Symmetric Dimer Nanostructures”. In: *Scientific Reports* 5.1 (Dec. 2015), p. 17534. ISSN: 2045-2322. DOI: 10.1038/srep17534.

[78] Lixing Kang et al. “Label-free plasmonic-based biosensing using a gold nanohole array chip coated with a wafer-scale deposited WS_2 monolayer”. In: *RSC Advances* 12.51 (2022), pp. 33284–33292. ISSN: 2046-2069. DOI: 10.1039/D2RA03479D.

[79] Yin-Kuang Yang et al. “Energy and cost efficient manufacturing of uniform periodic nanostructures enabled by an adaptable beam flattening device”. In: *Journal of Micromechanics and Microengineering* 35.1 (Jan. 2025), p. 015008. ISSN: 0960-1317, 1361-6439. DOI: 10.1088/1361-6439/ad9df5.

[80] David Vila-Liarte, Nicholas A. Kotov, and Luis M. Liz-Marzán. “Template-assisted self-assembly of achiral plasmonic nanoparticles into chiral structures”. In: *Chemical Science* 13.3 (2022), pp. 595–610. ISSN: 2041-6520, 2041-6539. DOI: 10.1039/D1SC03327A.

[81] Ingrid M. Weiss et al. “Thermal decomposition of the amino acids glycine, cysteine, aspartic acid, asparagine, glutamic acid, glutamine, arginine and histidine”. In: *BMC Biophysics* 11.1 (Feb. 2018). ISSN: 2046-1682. DOI: 10.1186/s13628-018-0042-4.

[82] Lili Liu et al. “Role of the Solvent–Surfactant Duality of Ionic Liquids in Directing Two-Dimensional Particle Assembly”. In: *The Journal of Physical Chemistry C* 124.44 (Nov. 2020), pp. 24215–24222. ISSN: 1932-7447, 1932-7455. DOI: 10.1021/acs.jpcc.0c07221.

[83] Swagato Sarkar et al. “Enhanced Figure of Merit via Hybridized Guided-Mode Resonances in 2D-Metallic Photonic Crystal Slabs”. In: *Advanced Optical Materials* 10.21 (Nov. 2022), p. 2200954. ISSN: 2195-1071, 2195-1071. DOI: 10.1002/adom.202200954.

[84] P. B. Johnson and R. W. Christy. “Optical Constants of the Noble Metals”. In: *Physical Review B* 6.12 (Dec. 1972), pp. 4370–4379. ISSN: 0556-2805. DOI: 10.1103/PhysRevB.6.4370.

[85] Edward D Palik. *Handbook of optical constants of solids*. Vol. 3. Academic press, 1998.

[86] Maryam Mirahmadi and Roman Krahne. “Advanced Chiral Sensing Using Tilted Plasmonic Nanostructure: A Theoretical and Numerical Study”. In: *2024 IEEE Photonics Conference (IPC)*. 2024, pp. 1–2. DOI: 10.1109/IPC60965.2024.10799518.

[87] Vincenzo Caligiuri et al. “A Semi-Classical View on Epsilon-Near-Zero Resonant Tunneling Modes in Metal/Insulator/Metal Nanocavities”. In: *Nano Lett.* 19.5 (Mar. 2019), pp. 3151–3160. ISSN: 1530-6992. DOI: 10.1021/acs.nanolett.9b00564.

[88] Aniket Patra et al. “Design and Polarization Control of the Modal Splitting in Hybrid Anisotropic Nanocavities”. In: *Adv. Opt. Mater.* 11.10 (Mar. 2023). ISSN: 2195-1071. DOI: 10.1002/adom.202202876.

[89] Baptiste Auguié and William L. Barnes. “Collective Resonances in Gold Nanoparticle Arrays”. In: *Phys. Rev. Lett.* 101.14 (Sept. 2008), p. 143902. DOI: 10.1103/PhysRevLett.101.143902.

[90] Boris Lukýanchuk et al. “The Fano resonance in plasmonic nanostructures and metamaterials”. In: *Nat. Mater.* 9.9 (Aug. 2010), pp. 707–715. ISSN: 1476-4660. DOI: 10.1038/nmat2810.

[91] Xianzhe Zhang et al. “Enhancing Superchiral Fields and Circular Dichroism Detection with Achiral Dielectric Metasurfaces”. In: *Nano Letters* 25.33 (Aug. 2025), pp. 12620–12626. ISSN: 1530-6992. DOI: 10.1021/acs.nanolett.5c02945.

[92] Mikhail F. Limonov et al. “Fano resonances in photonics”. In: *Nature Photonics* 11.9 (Sept. 2017), pp. 543–554. ISSN: 1749-4893. DOI: 10.1038/nphoton.2017.142.

[93] Andrey E. Miroshnichenko, Sergej Flach, and Yuri S. Kivshar. “Fano resonances in nanoscale structures”. In: *Reviews of Modern Physics* 82.3 (Aug. 2010), pp. 2257–2298. ISSN: 1539-0756. DOI: 10.1103/revmodphys.82.2257.

[94] Swagato Sarkar and Tobias A. F. König. “Engineering Plasmonic Hybridization toward Advanced Optical Sensors”. In: *Advanced Sensor Research* 3.1 (Jan. 2024), p. 2300054. ISSN: 2751-1219, 2751-1219. DOI: 10.1002/adsr.202300054.

[95] Sezer Seçkin et al. “Super-Radiant SERS Enhancement by Plasmonic Particle Gratings”. In: *ACS Applied Materials & Interfaces* 15.36 (Sept. 2023), pp. 43124–43134. ISSN: 1944-8244, 1944-8252. DOI: 10.1021/acsami.3c07532.

[96] Ina Alber et al. “Visualization of Multipolar Longitudinal and Transversal Surface Plasmon Modes in Nanowire Dimers”. In: *ACS Nano* 5.12 (Dec. 2011), pp. 9845–9853. ISSN: 1936-0851, 1936-086X. DOI: 10.1021/nn2035044.

[97] V. G. Kravets et al. “Plasmonic Surface Lattice Resonances: A Review of Properties and Applications”. In: *Chemical Reviews* 118.12 (June 2018), pp. 5912–5951. ISSN: 1520-6890. DOI: 10.1021/acs.chemrev.8b00243.

[98] Christoph Hanske et al. “Strongly Coupled Plasmonic Modes on Macroscopic Areas via Template-Assisted Colloidal Self-Assembly”. In: *Nano Letters* 14.12 (Dec. 2014), pp. 6863–6871. ISSN: 1530-6984, 1530-6992. DOI: 10.1021/nl502776s.

[99] Delphine Manchon et al. “Plasmonic coupling with most of the transition metals: a new family of broad band and near infrared nanoantennas”. In: *Nanoscale* 7.3 (2015), pp. 1181–1192. ISSN: 2040-3364, 2040-3372. DOI: 10.1039/C4NR05383D.

[100] Jing Zhao et al. “Resonance Localized Surface Plasmon Spectroscopy: Sensing Substrate and Inhibitor Binding to Cytochrome P450”. In: *The Journal of Physical Chemistry C* 112.34 (Aug. 2008), pp. 13084–13088. ISSN: 1932-7447, 1932-7455. DOI: 10.1021/jp801719c.

[101] X.Q. Li, S.Q. Liu, and X.Y. Tao. “Kinetic Modeling of Self-Generated Magnetic Fields by Transverse Plasmons in the Relativistic Regime”. In: *Contributions to Plasma Physics* 48.4 (May 2008), pp. 361–374. ISSN: 0863-1042, 1521-3986. DOI: 10.1002/ctpp.200810060.

[102] I. Yu. Chestnov et al. “One-dimensional Tamm plasmons: Spatial confinement, propagation, and polarization properties”. In: *Physical Review B* 96.24 (Dec. 2017), p. 245309. ISSN: 2469-9950, 2469-9969. DOI: 10.1103/PhysRevB.96.245309.

[103] Antonio Minopoli et al. “Double-Resonant Nanostructured Gold Surface for Multiplexed Detection”. In: *ACS Applied Materials & Interfaces* 14.5 (Feb. 2022), pp. 6417–6427. ISSN: 1944-8244, 1944-8252. DOI: 10.1021/acsami.1c23438.

[104] T. Maurer et al. “Enhancing LSPR Sensitivity of Au Gratings through Graphene Coupling to Au Film”. In: *Plasmonics* 9.3 (June 2014), pp. 507–512. ISSN: 1557-1955, 1557-1963. DOI: 10.1007/s11468-013-9649-0.

[105] Anders Pors et al. “Efficient unidirectional polarization-controlled excitation of surface plasmon polaritons”. In: *Light: Science & Applications* 3.8 (Aug. 2014), e197–e197. ISSN: 2047-7538. DOI: 10.1038/lsa.2014.78.

[106] Yi Zhou et al. “Guided Mode Resonance Sensors with Optimized Figure of Merit”. In: *Nanomaterials* 9.6 (June 2019), p. 837. ISSN: 2079-4991. DOI: 10.3390/nano9060837.

[107] Pankaj K. Sahoo, Swagato Sarkar, and Joby Joseph. “High sensitivity guided-mode-resonance optical sensor employing phase detection”. In: *Scientific Reports* 7.1 (Aug. 2017), p. 7607. ISSN: 2045-2322. DOI: 10.1038/s41598-017-07843-z.

[108] Daniel W. Hewak and John W. Y. Lit. “Generalized dispersion properties of thin-film waveguides”. In: *Applied Optics* 25.12 (June 1986), p. 1977. ISSN: 0003-6935, 1539-4522. DOI: 10.1364/AO.25.001977.

[109] Hyungsoon Im et al. “Atomic Layer Deposition of Dielectric Overlayers for Enhancing the Optical Properties and Chemical Stability of Plasmonic Nanoholes”. In: *ACS Nano* 4.2 (Feb. 2010), pp. 947–954. ISSN: 1936-0851, 1936-086X. DOI: 10.1021/nn901842r.

[110] S. Carretero-Palacios et al. “Effect of film thickness and dielectric environment on optical transmission through subwavelength holes”. In: *Physical Review B* 85.3 (Jan. 2012), p. 035417. ISSN: 1098-0121, 1550-235X. DOI: 10.1103/PhysRevB.85.035417.

[111] Martin G. Blaber et al. “LSPR Imaging of Silver Triangular Nanoprisms: Correlating Scattering with Structure Using Electrodynamics for Plasmon Lifetime Analysis”. In: *The Journal of Physical Chemistry C* 116.1 (Jan. 2012), pp. 393–403. ISSN: 1932-7447, 1932-7455. DOI: 10.1021/jp209466k.

[112] Thomas Siegfried et al. “Engineering Metal Adhesion Layers That Do Not Deteriorate Plasmon Resonances”. In: *ACS Nano* 7.3 (Mar. 2013), pp. 2751–2757. ISSN: 1936-0851, 1936-086X. DOI: 10.1021/nn4002006.

[113] Georg Haberfehlner et al. “3D Imaging of Gap Plasmons in Vertically Coupled Nanoparticles by EELS Tomography”. In: *Nano Letters* 17.11 (Nov. 2017), pp. 6773–6777. ISSN: 1530-6984, 1530-6992. DOI: 10.1021/acs.nanolett.7b02979.

[114] Masanobu Iwanaga and Bongseok Choi. “Heteroplasmon Hybridization in Stacked Complementary Plasmo-Photonic Crystals”. In: *Nano Letters* 15.3 (Mar. 2015), pp. 1904–1910. ISSN: 1530-6984, 1530-6992. DOI: 10.1021/nl504755d.

[115] Tigran V. Shahbazyan. “Local Density of States for Nanoplasmonics”. In: *Physical Review Letters* 117.20 (Nov. 2016), p. 207401. ISSN: 0031-9007, 1079-7114. DOI: 10.1103/PhysRevLett.117.207401.